Black and Brown Carbon Particles in the Atmosphere of a Northeast Indian City – Study of properties, sources, and impacts through field study and modelling

A Thesis

Submitted in Partial Fulfillment of the Requirements

for the award of the Degree of

Doctor of Philosophy

by

Sameer Singh

Department of Civil Engineering
Indian Institute of Technology Guwahati
Guwahati - 781039, Assam, India

January 2023

Dedicated

to

my mentor and supervisor

Prof. Sharad Gokhale

&

my dear

Parents

I owe it all to you.

Many thanks!

भारतीय प्रौद्योगिकी संस्थान गुवाहाटी
Indian Institute of Technology Guwahati
Department of Civil Engineering

Declaration

I hereby declare that the work embodied in this thesis entitled "**Black and Brown Carbon Particles in the Atmosphere of a Northeast Indian City – Study of properties, sources, and impacts through field study and modelling**" carried out by me in the Department of Civil Engineering, Indian Institute of Technology Guwahati, Assam, India, under the supervision of **Prof. Sharad Gokhale**. Wherever I have consulted, the research findings of others in creating this work, I have given due credit by citing them in the text of the thesis and providing their details in the references.

Sameer Singh
Roll No.166104024
Department of Civil Engineering
Indian Institute of Technology Guwahati
Guwahati - 781039, Assam, India

Date : January 2023
Place: Guwahati

भारतीय प्रौद्योगिकी संस्थान गुवाहाटी
Indian Institute of Technology Guwahati
Department of Civil Engineering

Certificate

This is to certify that the work described in this thesis entitled "**Black and Brown Carbon Particles in the Atmosphere of a Northeast Indian City – Study of properties, sources, and impacts through field study and modelling**" submitted by **Sameer Singh** (Roll No. 166104024) is an authentic record of the results obtained from the research work carried out under my supervision in the Department of Civil Engineering, Indian Institute of Technology Guwahati, Assam, India. I certify that he has fulfilled all the requirements according to the rules of this institute regarding the investigations embodied in his thesis, and this work has not been submitted elsewhere for a degree.

Dr. Sharad Gokhale
Professor
Department of Civil Engineering
Indian Institute of Technology Guwahati
Guwahati - 781039, Assam, India

Date : January 2023
Place: Guwahati

Acknowledgements

The Ph.D. journey is not only about engaging in research. It is a life itself that we live and learn a lot from several challenges, ups, and downs in this entire period. This work would not have been possible without the help and support I received from many people during this incredible journey.

First of all, I would like to express my sincere gratitude to my supervisor **Prof. Sharad Gokhale**, Department of Civil Engineering, Indian Institute of Technology (IIT) Guwahati. It would not have been possible for me to reach this far without his immense support, motivation, patience, and constant encouragement throughout my Ph.D. course. His guidance helped me in all the time of research and writing of this thesis. I could not have imagined having a better supervisor and mentor for my Ph.D. course.

Besides my supervisor, I would like to express my sincere gratitude to the Chairman of my doctoral committee: **Prof. Saswati Chakraborty**, Department of Civil Engineering, IIT Guwahati, and the members of the doctoral committee: **Prof. Subashisa Dutta**, Department of Civil Engineering, IIT Guwahati and **Prof. Uppaluri Ramgopal V. S.**, Department of Chemical Engineering, IIT Guwahati for sharing their valuable time and insightful suggestions provided at various stages to improve the quality of my research work from multiple perspectives.

I want to thank the technical officer and staff: **Ms. Jonali Saikia**, **Mr. Chitta R. Medhi**, and **Mr. Payodhar Pathak**, Department of Civil Engineering, IIT Guwahati, for helping me during fieldwork and providing technical details of the instruments. I extend my thanks to the office staff of the Department of Civil Engineering, **Mr. Susanta K. Sarma**, and **Ms. Juri J. Hazarika** for their kind co-operation, and smooth and rapid execution of office work. I would also thank my co-researchers **Dr. Jayashree Dutta**, **Dr. Sushant K. Padhi**, **Dr. N. Premananda Singh**, **Dr. Mitali Sahu**, **Ardhendu Shekhar Chaudhury**, and **Dr. Rajneesh Kumar** who were a great helping hand from time to time throughout my Ph.D. journey. I had a wonderful off-research time with my friends (Dr. Ashutosh Sharma, Umesh Chaudhary), colleagues (Argha Kamal Guha, Neeldip Barman, Rajarshi Sarma, and Himanshu Gupta),

and project staff (Alkesh Barman, Arindom Borah, Dr. Dudul Das, Hrishikesh Battacharya, Rahul Choudhary, and Rajib Das) of the Air and Noise Pollution Laboratory, Department of Civil Engineering at IIT Guwahati.

I would like to express my sincere thanks to the Doloi of Maa Kamakhya Devalaya: **Mr. Mohit Ch. Sarma** and **Mr. Kabindra Prasad Sarma** for providing the necessary facilities such as electricity and premises during the fieldwork at Ma Kamakhya Devalaya Health Care Centre on the Nilachal hills.

It goes without saying that this journey would not have been possible without the constant support, unconditional love, and profound encouragement of my parents **Dr. Gore Lal** and **Mrs. Ranno Devi**. They never questioned my intentions and supported me in all my endeavors. There are no words to express my gratitude to them. And finally, last but not least, I thank my wife, who has provided me with moral and emotional support in my life.

This list is obviously incomplete, and I once again record my gratitude to all those who have cooperated with me directly or indirectly in this endeavor.

Date: January 2023 **Sameer Singh**

Contents

Abstract

Black Carbon (BC) is a short-lived climate pollutant, which has been demonstrated to pose significant negative impacts on climate and human health. On-road traffic and open burning of biomass are two primary sources of BC emissions in India. It has been observed that hilly regions tend to show a higher concentration of BC due to the movement of wind being obstructed by the geographical entities and exhibit different meteorology than plains. Low-level clouds over the hilly region of northeast India and longer hill fogs might not only be affecting the mass concentrations of BC but might also be affecting its radiative properties. The northeast India being close to the Himalayas is vulnerable to climate change. It is essential to study radiation properties and determine the contributions of fossil fuel to the ambient BC and its dispersion over the hilly region of Guwahati. These objectives were achieved by measurements and modelling of BC at two locations in the hills of Guwahati and analyzing the data using radiation absorption equations with the site-specific properties of BC.

The equivalent BC measurements were conducted using a seven-wavelength Aethalometer (AE-33) during winter 2020 from Jan-March over a suburban atmosphere in Guwahati, Northeast India. The daily $PM_{2.5}$ and PM_{10} concentrations were also measured simultaneously to quantify the share of BC and study inter-relationship. The chemical species such as metals (Fe, Mn, Zn, Cu, Cr, Pb, Al) and ions (NO_3^-, SO_4^{2-}, F^-, and Cl^-) in $PM_{2.5}$ and PM_{10} were also quantified to study the correlation with BC. The contribution of two distinct sources obtained by AE-33 has been improved using site-specific Aerosol Angstrom exponent. The best wavelength pair to apportion BC from two sources such as fossil fuel and biomass burning has been worked out. The key findings of the research showed that the traffic-derived BC emissions (BC_{FF}) dominate over biomass burning. The BC levels substantially varies with local meteorological conditions and the traffic volume & its composition. The light absorption of BC dominated at all wavelengths from 370 to 950 nm. Primary and secondary Brown Carbon significantly contribute to aerosol light absorption at a shorter wavelengths (370 to 660 nm) during winter nighttime.

The AERMOD model was used to model BC from emissions originated from moving traffic as line source and parking lot as area source using observational and WRF-processed meteorology for the winter period. Hilly terrain obstructs winds and develops a negative pressure loading to a vacuum on the other side of the hills, which promotes accumulation of emissions causing high BC concentrations. The pockets of higher concentration were seen at the locations where steep slopes were associated with low winds and hill fogs. The AERMOD model after statistical evaluation against the observational BC concentrations in two topographical areas during winter has been applied to study the reduction in BC concentrations due to implementation of vehicular emission norms as mitigation measures i.e. Bharat Stage BS-IV (equivalent to Euro 4) and BS-VI (equivalent to Euro 6). It was found that the BC_{FF} concentrations for BS-IV and BS-VI reduced by 35% and 75%, respectively. The model was used to study the contribution of each vehicular category in BC concentration. Based on all these findings, mitigation measures were suggested for reduction of BC concentration from traffic. The observational data incidentally falling in period of COVID-19 lockdown has also been analyzed for radiative properties and comparison has been done. The probable source of origin of high aerosol loading was investigated using HYSPLIT model.

The health risk of BC and $PM_{2.5}$ were estimated in terms of daily passive smoking method. The conclusions drawn in this research will be useful in making new strategies to reduce BC emissions and issue public health advisories during haze occasions. Thus, it will promote the implementation of strict regulations aiming to improve deteriorating air quality and safeguard the exposed individuals in the hilly regions of the Brahmaputra River Basin.

Keywords: Aethalometer; Black Carbon; Brown Carbon; Source apportionment; Optical properties; AERMOD; Health risks; COVID-19; Brahmaputra river valley; Northeast India.

List of Figures

List of Tables

List of Symbols

Symbols	Description
b_{abs}	Aerosol Absorption Coefficient
b_{abs_BC}	Absorption Coefficient of Black Carbon
$b_{abs\_B_rC}$	Aerosol Absorption Coefficient of Brown Carbon
$b_{abs\_B_rC\_sec}$	Aerosol Absorption Coefficient of secondary Brown Carbon
b_{abs_λ}	Aerosol Absorption Coefficient at particular wavelength
BS-IV	Bharat Stage emission norm-IV
BS-VI	Bharat Stage emission norm-VI
C_o	Observed concentration
C_p	Predicted concentration
CO	Carbon Monoxide
CO_2	Carbon Dioxide
d	Index of the agreement
h	Hour
h_s	Height of stack
H_2S	Hydrogen sulfide
I_o	Intensity of incoming light
I	Intensity of remaining light after passing through a filter
Δh	Updraft velocity
λ	Wavelength
σ_y & σ_z	Dispersion coefficients in horizontal (y) & vertical (z) direction
μm	Micrometer
km	Kilometer
m	meter
NH_3	Ammonia
NO_2	Nitrogen dioxide
nm	Nanometer
O_3	Ozone

$PM_{2.5}$	Particles having aerodynamic diameter less than 2.5 μ
PM_{10}	Particles having aerodynamic diameter less than 10 μ
r	Pearson's product moment correlation
R^2	Coefficients of determination
SO_2	Sulfur dioxide
u	Wind velocity
μ	Micro
μg	Microgram
x	downwind distance
z	thickness of a filter paper
Z	Height of receptor
Z_i	Height of convective boundary layer

List of Abbreviations

Terms	Description
2W	Two Wheeler
3W	Three Wheeler
4W	Four Wheeler
AAE	Aerosol Angstrom Exponent
AAE_{FF}	Angstrom Absorption Exponent values associated with Fossil Fuel
AAE_{BB}	Angstrom Absorption Exponent values associated with Biomass Burning
AERMOD	American Meteorological Society/Environmental Protection Agency Regulatory Model
AGL	Above Ground Level
AMS	American Meteorological Society
AMSL	Above Mean Sea Level
ARAI	Automotive Research Association of India
AT	Atmospheric Temperature
BB	Biomass Burning
BC	Black Carbon
BC_{BB}	Black Carbon associated with Biomass Burning
BC_{FF}	Black Carbon associated with Fossil Fuel
B_rC	Brown carbon
B_rC_{pri}	Primary Brown Carbon
B_rC_{sec}	Secondary Brown Carbon
BP	Barometric Pressure
BRB	Brahmaputra River Basin
BRV	Brahmaputra River Valley
BS	Bharat Stage
CBL	Convective Boundary Layer
CC	Controlled Combustion
CLAP	Continuous Light Absorption Photometer

CM	Cardiovascular Mortality
CPCB	Central Pollution Control Board
CPF	Conditional Probability Function
eBC	equivalent Black Carbon
EC	Elemental Carbon
EF	Emission Factor
EF_{BC}	Emission Factor of Black Carbon
EPA	Environmental Protection Agency
ETS	Environmental Tobacco Smoke
EU	European Union
FAC2	Fraction of extrapolations within a Factor of two observations
FB	Fractional Bias
FF	Fossil Fuel
GDP	Gross Domestic Product
Gg	Giga-gram
GMB	Geometric Mean Bias
GV	Geometric Variance
HDDV	Heavy Duty Diesel Vehicle
HYSPLIT	Hybrid Single-Particle Lagrangian Integrated Trajectory
IGP	Indo-Gangetic Plains
IPCC	Intergovernmental Panel on Climate Change
IHR	Indian Himalayan Region
IR	Infrared
ISCST	Industrial Source Complex Short Term
IC	Ion Chromatography
IHD	Ischemic Heart Disease
LBWI	Low Birth Weight of Infants
LC	Lung Cancer
LDDV	Light Duty Diesel Vehicle
LD	Lockdown

LMV	Light Motor Vehicles
LPM	Litre Per Minute
LST	Local Standard Time
MAC	Mass Absorption Cross-Section
MSE	Mean Squared Error
NAAQS	National Ambient Air Quality standards
NE	North East
NH	National Highway
NMSE	Normalized Mean Square Error
OC	Organic Carbon
PC	Passenger Car
PM	Particulate Matter
PSAP	Particle Soot/Absorption Photometers
PSC	Passively Smoked Cigarettes
PLFD	Lung Function Decrement in children in Percent
rBC	refractory Black Carbon
RH	Relative Humidity
RMSE	Root Mean Square Error
SR	Solar Radiation
SRTM1	Shuttle Radar Topography Mission of one arc second
SAR-CoV-2	COVID-19 pandemic
USEPA	United States Environmental Protection Agency
UTM	Universal Transverse Mercator
UV	Ultraviolet
VOC	Volatile Organic Compound
WD	Wind Direction
WHO	World Health Organization
WRF	Weather Research Forecasting
WS	Wind Speed
WD	Wind Direction

1

Introduction

1.1 General

Black Carbon (BC) is an unwanted fraction of fine particulate matter ($PM_{2.5}$)[†] produced through incomplete combustion of biomass and fossil fuel associated with anthropogenic and natural activities (Bond et al., 2011; Deng et al., 2020; Chaudhury et al., 2022). BC, also known as soot, is the particulate form of short-lived climate forcing pollutant with warming potential next to Carbon Dioxide (CO_2) (Bond and Sun, 2005). Table 1.1 shows a comparison of BC and CO_2 in detail. It is directly linked to the atmospheric environment through different physicochemical and biological processes, which affect the local air quality (Jacobson, 2004; Chen et al., 2022). Once released, it can travel a long distance into ambient air in a shorter duration (Ramanathan and Carmichael, 2008) and influence air quality in local to regional and intercontinental areas. It is also a primary pollutant, so its concentration in the atmosphere is directly linked to anthropogenic activities (USEPA, 2012). Although various sources of BC have been identified, it is emitted from the transportation sector, observed to have high light absorption and adverse effects on the atmosphere and human health (Bond et al., 2013; Van der Zee et al., 2016; Wang et al., 2022). Rapid urbanization, unprecedented growth in vehicles, and improper planning in the road networks result in traffic congestion, which has increased BC emissions in several developing countries like India. In India, open burning of agricultural waste and forest fires accounts for 24% of all BC emissions, while transportation sector and industries contribute 21% and 15%, respectively (USEPA, 2012).

[†]particles with the aerodynamic diameter less than or equal to 2.5 micron.

Table 1.1 Comparison of Black Carbon to CO_2 based on the properties that influences the climate (USEPA, 2012).

Property	Black Carbon	CO_2
Atmospheric life time	Days to weeks	Up to millennia
Distribution of atmospheric concentrations	Highly variable both geographically and temporally correlating with emission sources	Generally uniform across the globe
Direct radiative properties	Absorbs all wavelengths of solar radiation	Absorbs only thermal radiation
Global mean radiative forcing	+0.34 to 1.0 W m^{-2} direct forcing +0.05 W m^{-2} (snow/ice albedo forcing) Net effect: uncertain, but likely warming	+1.66 (± 0.17 W m^{-2})
Cloud interactions	Multiple cloud interactions that can lead to warming or cooling as well as effects on precipitation	Increases cloud droplet acidity
Surface albedo effects	Contributes to accelerated melting of snow/ice and reduces reflectivity by darkening snow and ice, enhancing climate warming	No direct surface albedo effects
Contribution to current global warming	Likely third largest contributor (after CO_2 and CH_4), but large uncertainty	Largest contributor
Dimming	Contributes to surface dimming	No direct effects on surface dimming

Traffic is responsible for ~33-90% of BC emission in areas rich with vehicular activities and traffic congestion (USEPA, 2002), while around 8% of BC is produced from open burning of biomass (Reid et al., 2005). It is also reported that the traffic-originated BC particles are darker than the particles from biomass combustion, hence, having higher warming effects (Han et al., 2017; Ramanathan and Carmichael, 2008). Moreover, different types of fuels combustions produce different amounts of BC. For example, natural gas combustion produces too little BC, while diesel combustion produces quite a high BC (Evans et al., 2017). Therefore, BC emissions are required to be reduced from biofuel combustion and from direct vehicular emissions to prevent acute impact on regional climate. This problem can be solved by developing mitigation measures and implementing proper technology. Fig. 1.1 shows the different species derived from two sources.

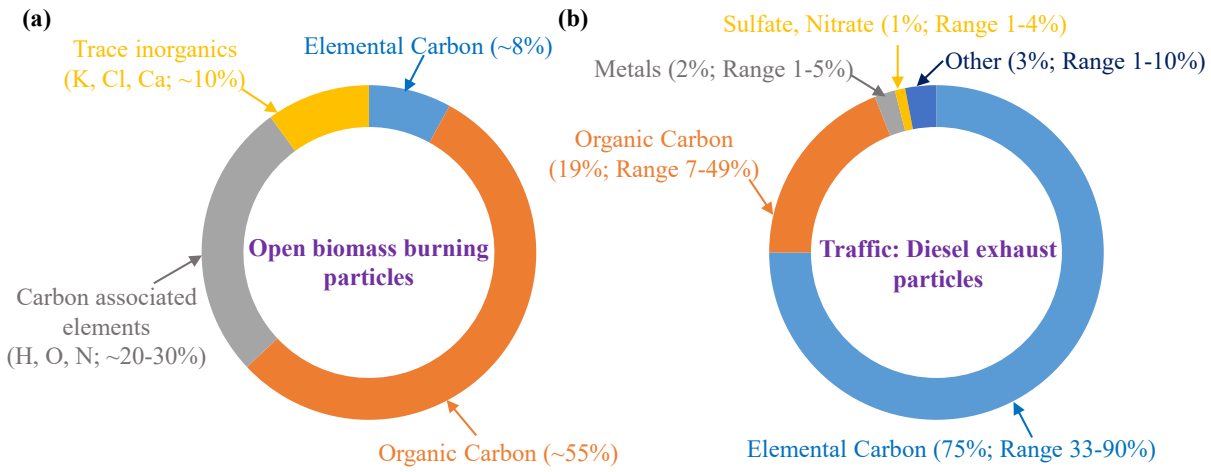

Fig. 1.1 Distribution of particles originated from (a) biomass burning (Reid et al., 2005) and (b) heavy-duty diesel $PM_{2.5}$ emissions (USEPA, 2002).

The BC concentrations found in various cities of India mainly from traffic and biomass burning are shown in Fig. 1.2. The measurements were conducted using different models of the Aethalometer, and the apportionment was done at default settings except for a few studies. It can be seen that the BC concentration associated with fossil fuel was higher than the winter mean of cities under consideration. While, biomass burning contributed more to the total BC concentrations in India's eastern and northeastern parts of the Himalayas.

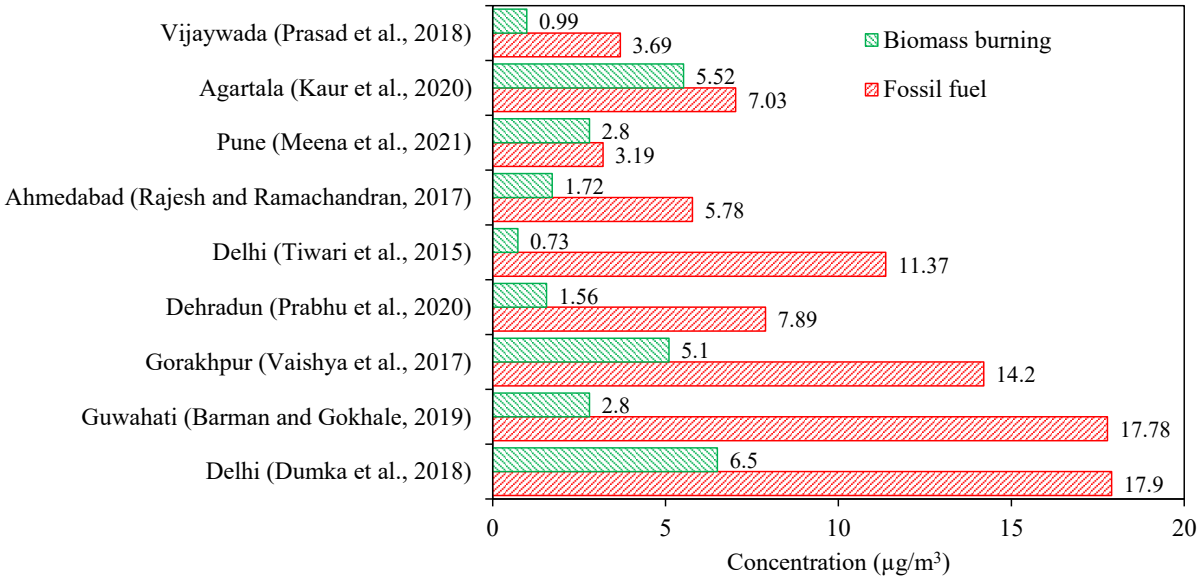

Fig. 1.2 Black Carbon concentrations from two sources in Indian cities during winter.

BC has its importance in the current situation of global warming as it is the third largest contributor that absorbs solar radiation at all wavelengths ranging from 370 to 950 nm (USEPA, 2012). It has high radiation absorption properties, resulting in global warming, snow albedo effects, and a deteriorating impact on cloud formation and precipitation (Jacobson, 2004). After CO_2, BC is the second-largest contributor to global warming with a net positive radiative forcing of 1-1.2 Wm^{-2} (Jacobson, 2001; Bond et al., 2013). BC in the atmosphere absorbs sunlight; and thus has positive radiative forcing (Chakrabarty et al., 2012; Liu et al., 2018). Chakrabarty et al. (2012) showed that the total reduction of shortwave radiation reaching the surface is ~63 Wm^{-2} and radiating back to the atmosphere is ~11 Wm^{-2} under cloud-free conditions. Tiwari et al. (2016) showed that BC contributes to the cooling effect at the surface level in the Brahmaputra river valley (BRV) region. Another study of the Central Indo Gangetic Plain site (Gorakhpur, India) showed that BC emissions from local sources are dominant over these long-distance transported due to calm wind conditions and shallow boundary layer height (Vaishya et al., 2017). Chaudhury et al. (2022) concluded that the meteorology's effect on BC's spatiotemporal variability was negligible at the surface locations (at 1.5 m height) in the BRV region. Sarkar et al. (2015) reported a higher contribution from local sources (huge tourist activities) followed by long-range and mountain wind transport during the pre-monsoon season at the high-altitude location in the eastern part of the Himalayas in India. It is also reported that BC particles from Indo-Gangetic Plain are

being deposited into the northeastern part of the Himalayan regions in India during winter and pre-monsoon seasons (Barman and Gokhale, 2019).

Fig. 1.3 shows the number of papers published and the mean observed concentrations of BC in various parts of India from 2002 to 2018 (Rana et al., 2019). The highlighted map area represents the district from which BC measurements have been reported. Fig. 1.3a shows that the very few studies have been conducted in the northeastern region than the rest of India. Also, the levels of BC are comparable with the Indian cities. These levels of BC are alarming compared to the rest of India and worldwide. Fig. 1.3b signifies the spatial variation of at least year-long BC concentrations in India, where circle sizes are proportional to the BC concentrations. It provides the best estimate of the average BC in India during 2002-2018.

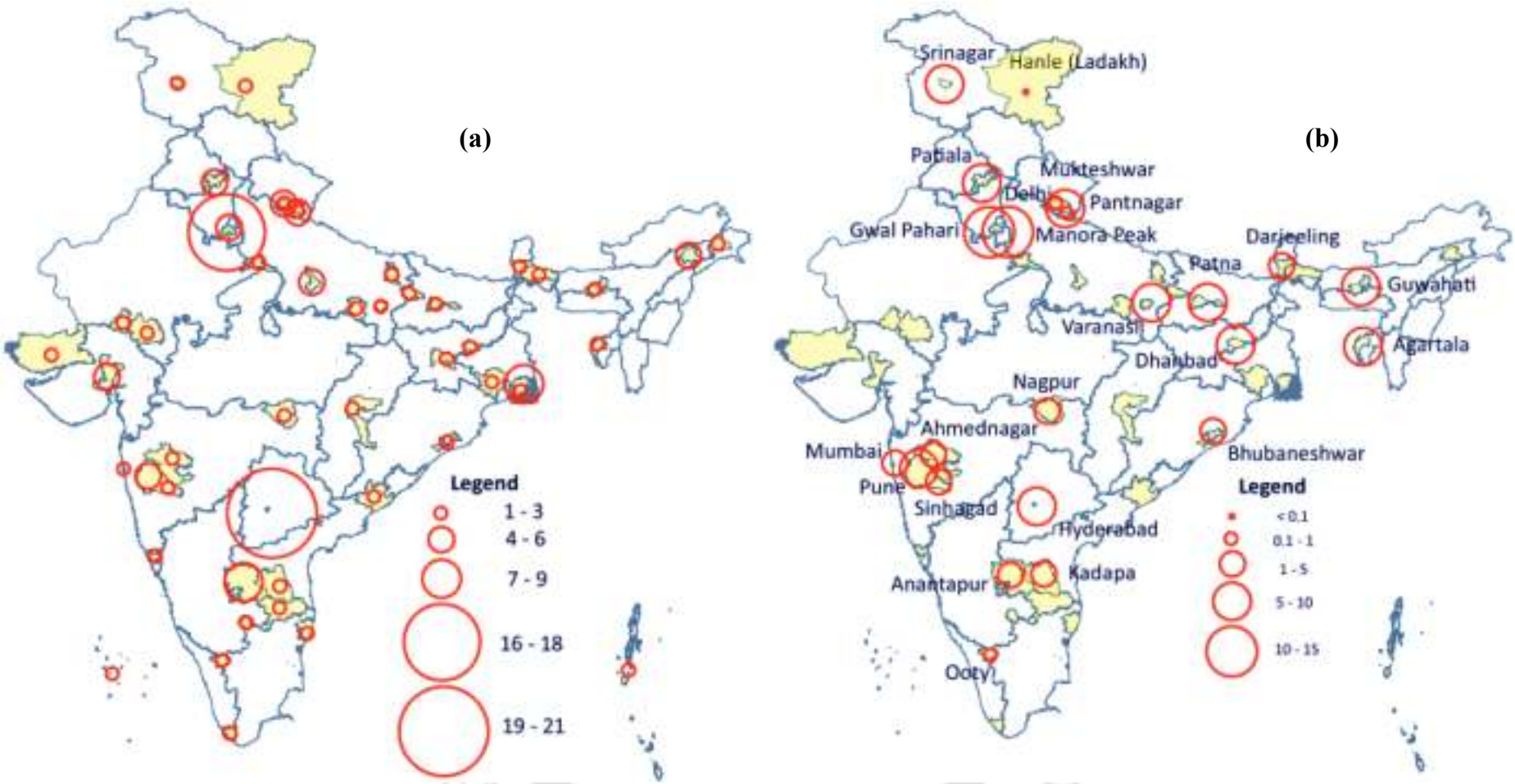

Fig. 1.3 (a) Number of research papers published on atmospheric Black Carbon in India, (b) Variation of average Black Carbon concentrations (μg m^{-3}) in India based on published literature during 2002-2018 (Rana et al. 2019). The presented data show those studies that report at least year-long Black Carbon measurements. The highlighted area on the map represents the district from which Black Carbon measurements have been reported.

In a particular region, the impacts of BC can be attributed to local emissions, meteorological conditions and local geography. There is rising concern that the natural reserves on the Himalayas are in retreat due to aerosol BC (Barman and Gokhale, 2019). The rate of warming is different with location and elevation because high mountainous, hilly topographical environments experience more rapid changes in temperature than environments at lower elevations (Goldreich et al., 1986). Hilly regions have complex wind flow patterns due to high and low ridges obstructing the direct wind flow. Almost 70% of the region in northeast India has hilly ecosystem, where alpine vegetation, snow-capped high mountains (1-5 km, above mean sea level [a.s.l.]), and rocky surface dominate the physical landscape (Pathak et al., 2021). For better health assessment and air quality management the emission of Black Carbon in such areas might exhibit optical properties different from those in simple terrain areas. It may affect the accuracy of the apportionment of BC to the fossil fuel and biomass burning. As per the Economic Survey of India (2015), the state of Assam showed a growth rate in emission density of BC by 15.9% and the growth rate of per capita by 14.5% in national summary data pages. The number of on-road automobiles in Assam has increased from 0.53 million in 2001 to 2.84 million in 2018 (Economic survey of Assam, 2017). The vehicles plying on the roads of Guwahati city are all mixed in the various proportion of BS-II, BS-III, and BS-IV compliant. Besides, a railway network (972 km) across the northeastern states is mostly diesel power-driven, which might also be contributing to the atmospheric BC.

Guwahati is the largest and fast developing urbanized city in northeast India. It is situated in a small to steep-sloped hilly region of the lower Brahmaputra river basin. Besides hill fogs in winter are severe, stays for long time at low levels, which may trap pollutants and create pockets of high pollution. Thus, measurements and observations of BC in the hilly areas with considerable human settlements are essential to improve understanding of the impact of BC, its contribution to light absorption, and dispersion in hilly terrain. This information is needed to improve emission inventories and formulate mitigation strategies. Barman and Gokhale (2019) showed that in Guwahati, traffic and biomass contribute 85-92% and 9-15%, respectively, to the total BC. Another study by Chaudhury et al. (2022) reported higher values of BC measured at surface locations (at 1.5 m height) when compared with

upper location (at 15 m height) measurements between August 2016 to July 2017. Only these studies on BC are available each with a limited data for about a week mostly restricted to ∼20 m above the ground level (Chakrabarty et al., 2012; Tiwari et al., 2016; Barman and Gokhale, 2019; Chaudhury et al., 2022). The source apportionment of BC is not done using aerosol absorption coefficient. The characterization of Brown Carbon, both primary and secondary at shorter wavelengths (370-660 nm) is not done. The compared studies and their results showed that the source apportionment techniques are based on the default Aethalometer settings, which have been improved in the present study by using site-specific properties. In the Indian context, fossil fuel is the most dominant factor contributing more to BC than biomass burning. The reason could be that the technology used in the vehicles is old (BS-II, BS-III, and BS-IV compliant). Given the share of old vehicles (7-15 years petrol and 7-10 years diesel vehicles) in the fleet, BC emission is high compared to metro cities where the old vehicles are phased out. The Indian government implemented new emission norms (BS-VI) in 2020 to tackle air pollution from vehicular categories. This study may be useful as a base study for future projections of BC when these vehicles will be phased out from Guwahati. The present study, therefore, focuses on the longer (winter and pre-monsoon season) measurements of BC, its optical properties, its dominant source identification, and its dispersion over the complex terrain with the measurement location situated on the peak of the hills to study effect of hill fog and complex topography. The research objectives were framed based on research gaps and have been presented in the subsequent Chapter 2.

1.2 Scope and objective

The primary objective is the source apportionment of Black and Brown Carbon aerosols from light absorption observation and to investigate the spatio-temporal variability using source-oriented modelling in the study region of Guwahati, Northeast Indian city. The expected results of this research may contribute to the state-of-art study, literature on BC from this region, which is close to Himalayas and, therefore, in the context of climate change has significance. Key tasks to achieve the main objective are as follows:

i. Fieldwork involving the selection of study domain & monitoring locations, measurements of $PM_{2.5}$, PM_{10} and Black Carbon concentrations simultaneously, collection of

local meteorological parameters, traffic volume survey within the study region for winter period from Jan - March 2020.

ii. Data analysis and interpretation in respect of winter season and COVID-19 lockdown on Black Carbon air quality.

iii. Optical properties of Black and Brown Carbon aerosols (primary and secondary) and their contribution to the total aerosol light absorption at different wavelengths.

iv. Source apportionment of Black Carbon (at 880 nm) and contribution of dominating sources using light absorption-based default and improved method.

v. Health risks of Black Carbon and $PM_{2.5}$ on human health in terms of an equivalent passively smoked cigarette.

vi. Modelling the dispersion of traffic-derived Black Carbon emission in a hilly terrain using observational and WRF-modelled weather data using AERMOD model.

vii. Application of the model to study the impacts.

1.3 Novelty statement

The apportion of the sources of Black Carbon aerosols has been conducted on the Himalayas and other places using default Aethalometer settings, which are mentioned in the literature section. This study used an improved light absorption-based method, which is missing in the studies conducted in the country.

i. Source apportionment of Black Carbon from vehicles and biomass burning in the hilly region of Guwahati using an improved light absorption based-method.

ii. Contribution of primary and secondary Brown Carbon to the total aerosol light absorption using optical properties.

iii. Health risk for the dwellers of the hilly region due to Black Carbon and $PM_{2.5}$ in terms of daily passive smoking method.

iv. Comparative study of dispersion of traffic-derived Black Carbon emission in the hilly region using onsite and WRF simulated meteorology.

1.4 Thesis outline

The thesis is organized into seven chapters.

Chapter 1: Introduction - introduces the significance of the topic and highlights the problems and the limitations of the existing techniques used in the source apportionment studies. It gives an overview about Black Carbon and why the study has its significance in the Brahmaputra river valley region. It describes the main aim of this research to improve the Black Carbon apportion method based on the light absorption properties, the detailed scope and objectives of this research, novelty statements, and organization of the thesis.

Chapter 2: Literature review - reviews the studies on the Black Carbon emissions in different environments. It begins with the background of emission sources, impacts of traffic, and role of meteorological parameters, emission rates of Black Carbon, and source apportionment techniques based on default Aethalometer model. Subsequently, it covers aerosols' light absorption properties, including Black Carbon, primary and secondary Brown Carbon at different wavelengths. It further reviews the advantages and shortcomings of each method of source apportionment, air quality models used in the dispersion of air pollutants, followed by the summary with research gaps.

Chapter 3: Field Work and Research Methodology - the detailed methods for estimating the dominant sources of Black Carbon, human health risks of air pollutants (Black Carbon and $PM_{2.5}$), and dispersion of traffic-derived Black Carbon have been described. The chapter includes the site selection, traffic monitoring locations, data collection procedures later utilized in dispersion modelling. The proposed improved methodology for estimating the contribution of Black Carbon sources has been presented. A similar analysis has been conducted to check the effect of COVID-19 lockdown. The method built on the winter data was validated during the COVID-19 lockdown period.

Chapter 4: Data analysis and Interpretation - describes preliminary the data analysis and interpretation conducted on collected field data during the fieldwork. It have been organized for meaningful interpretation and discussed in detail. It consists of the pollutant concentrations, chemical species and meteorological characteristics. Further, the statistical relationship of pollutant concentration with traffic and meteorological characteristics has

been presented. It discussed the extent of relationship of meteorology and traffic with pollutant concentrations using statistical methods like Pearson correlation analysis and bi-variate polar plots. Moreover, the human health risks of air pollutants in terms of daily passively smoked cigarettes have been discussed.

Chapter 5: Results and discussion - aerosol light absorption, their contribution, different wavelengths, traffic, and meteorological characteristics. Further, the statistical relationship with meteorological parameters using statistical methods has been presented. It discussed the effect of local emissions using bi-variate polar plots, and probable sources of air masses originating from transboundary and coming to monitoring location using backward trajectory analysis utilizing the HYSPLIT model. Dispersion modelling covers the dispersion of traffic-derived BC emissions in hilly terrain. The spatio-temporal distribution of BC has been combined with the observed and WRF modelled meteorological data.

Chapter 6: Impacts and Mitigations - discuss the impacts of COVID-19 pandemic lockdown and hilly terrain on Black Carbon concentration and radiation properties of aerosols. It provides an understanding of the reduction of anthropogenic emissions during the different lockdown periods. The chapter also presents the calculation on reducing traffic-derived Black Carbon emissions to meet the Bharat Stage emission norms (BS-IV and BS-VI) proposed by the Indian government to reduce the air pollution caused by vehicular activities.

Chapter 7: Findings and Conclusions - summarizes the findings and conclusions from the research work, limitations, and scope of future work. The key points from the study are presented.

2

Literature Review

The literature review has been carried out on the topics relevant to the research objectives, including characteristics, sources, and various methodologies. It includes selecting the best pair of wavelength and Aerosol Angstrom Exponent to apportion the Black Carbon aerosol from two different sources, dispersion models, health effects in terms of passive smoking, and optical properties of primary and secondary Brown Carbon aerosols.

2.1 Carbonaceous aerosols and their characteristics

Black and Brown Carbon are two carbonaceous aerosols emitted from different sources with different characteristics. The question of what "Black Carbon" is cannot be answered quickly, and there is no exact definition of this term in the research community. Although, Black Carbon (BC) plays a significant role in the atmospheric environment once released from anthropogenic and natural activities. Additionally, the distinction against the term "soot" is not clarified. As per Intergovernmental Panel on Climate Change (IPCC, 2007a, p.810), soot is determined as a part of BC; in other, it is used interchangeably (IPCC, 2007b; Ramanathan and Carmichael, 2008; USEPA, 2012). Further, the definitions of BC were proposed in terms of particle morphology (Buseck et al., 2012), its characteristics (Bond et al., 2013), and measuring techniques (Petzold et al., 2005). Petzold et al. (2005) defined BC as "a useful qualitative description when referring to light-absorbing carbonaceous substances in atmospheric aerosol" and recommend using more specific terms for quantitative utilization. These terms are Equivalent Black Carbon (eBC), Refractory Black Carbon (rBC), and Soot. This study also recommended using the term "soot" to describe the formation of carbonaceous particles and not atmospheric aerosols. Some studies have also used Elemental Carbon (EC), light-absorbing carbon (Lack et al., 2014). In the present study, data derived from the optical

absorption methods are referred to as BC_{880}, since the procedures require a conversion of light absorption coefficient into mass concentration. The subscript 880 denotes the BC mass concentration at 880 nm wavelength since BC is the only substance to absorb the light (Bond and Bergstrom, 2006).

BC is an unwanted fraction of particulate matter formed during incomplete combustion of biofuel, fossil fuel, and biomass. Incomplete combustion means no complete conversion of the fuels or biomass into CO_2 and water due to lack of oxygen and too low temperature. Inadequate combustion occurs in several kinds of the burning process. During the burning processes, small carbon particles size ranging from 10 to 50 nm are formed and accumulated in aggregates (Buseck et al., 2012; Bond et al., 2013). The size of these particles entirely depends on the fuel burned. For example, Takahama et al. (2014) reported three modes of BC containing particle size below 100 nm, near 100 nm, and between 200 and 300 nm due to vehicular activities in an urban environment. The light-absorbing carbonaceous substances included in these aerosols are in this study called “Black Carbon” or “BC” or “BC_{880}”. These emitted particles are insoluble in water, while the irregular morphology facilitates the sorption of other species (Petzold et al., 2005). The formation of aggregates starts immediately after emission, and the aggregates get internally or externally mixed. Therefore, hardly any pure BC particles exist in the atmosphere, particularly in a highly polluted atmosphere. The particles grow via coagulation during transport. Their size distribution is directly related to the formation mechanism and atmospheric processes during transport. The more efficient the fuel burn, the smaller the particles. Usually, the BC particles are assigned to the Aitken mode, but they grow in the atmosphere due to subsequent coagulation and are found in the accumulation mode (Väkevä et al., 2002).

BC is removed from the atmosphere via wet and dry deposition (USEPA, 2012). Dry deposition acts as a sink for the atmospheric BC. In regions with high precipitation, wet deposition is necessary, like Northeast India. The lifetime of BC strongly depends on the deposition rate of the areas the particles are transported through. For example, Northeast India is a passage over which the pollutants are transported from Indo Gangetic plains and deposited to Himalayan margins (Barman and Gokhale, 2019). It usually has a short atmospheric lifetime between days to weeks (Cape et al., 2012; Bond et al., 2013).

Hilly regions are generally experiencing low wind circulation, which might lead to the accumulation of aerosols. The low-level fog occurrence in the winter season can lead to a higher concentration of aerosols. The deposition rate decreases with particle size for smaller particles, while it increases for larger particles (Nilsson and Rannik, 2001). Thus, the deposition might be higher in the hilly areas than in other regions, which might lead to a longer atmospheric lifetime of BC in the hilly region.

One of the essential properties of BC is the strong ability to absorb light in a spectral range of visible light. The mass-specific absorption coefficient, also known as mass absorption cross-section (MAC), at 550 nm of at least 5 $m^2\ g^{-1}$ (Petzold et al., 2013). In this study, the MAC values at seven discrete wavelengths provided by the manufacturer of the Aethalometer (AE-33) were used (Drinovec et al., 2015). The MAC is only slightly wavelength-dependent and holds for freshly formed particles. As mentioned above, BC particles can consist of a primary BC and a coating of different possible components. This coating may alter the optical properties of BC. Light absorption is enhanced if the primary BC is coated with scattering material (Fuller and Kreidenweis, 1999).

Two other specific particles absorbing visible light are Brown Carbon (B_rC) and dust particles (Bond et al., 2013). B_rC is a subset of organic aerosols and consists of a complex mixture of organic compounds. Its color results from non-uniform absorption over the visible wavelength range (Lack et al., 2014). It absorbs sunlight at shorter wavelengths (Andreae and Gelencsér, 2006). B_rC is originated from primary emissions or is formed through multiphase reactions in the ambient air (Laskin et al., 2015). Secondary organic aerosols from biomass burning are more absorptive at shorter wavelengths than the primary organic aerosols (Saleh et al., 2013). B_rC and BC are similar in size, but B_rC absorbs light weaker than BC at longer wavelengths. The MAC value of B_rC is smaller than 1 $m^2\ g^{-1}$, while dust in comparison to BC and B_rC has the lowest light absorption, around 0.009 $m^2\ g^{-1}$ at 550 nm (Petzold et al., 2013). Moreover, dust particles can be distinguished from BC since these have typical diameters larger than 2 μm, a crystalline structure, and crustal elements (Bond et al., 2013).

2.2 Sources of Black Carbon and Brown Carbon

Forest fires, volcanic eruptions, incomplete combustion of fossil fuel, and open biomass burning release the BC emissions in the atmospheric environment (Penner et al., 1993; Bond et al., 2013). Two-thirds of BC emission occurs in modern times due to anthropogenic activities involving fossil/biofuel combustion and domestic wood burning (Bond et al., 2013). Natural sources such as forest fires and savannah fires also contribute to BC emission into the atmospheric environment (Andreae and Metlet, 2001). The primary sources of BC can be classified based on the past emission inventory based on the following BC emitting sources (Andreae and Metlet, 2001; Bond et al., 2004; Lu et al., 2011):

i. Combustion of carbon-based fuels by industrial sector, power plants, transportation, and residential sector.

ii. Coke production, including the gas heating, refining, and leakage processes.

iii. Brick production, including material conveying, product drying, and fuel firing processes.

iv. Waste incineration, including combustion of municipal and industrial waste.

v. Outdoor biomass burning, including natural fires.

Bond et al. (2004) found that BC emissions from India were estimated as 483 Gg/y (ranging from 307 to 1035 Gg/y) based on fossil fuel and biomass combustion. Total BC emissions from India constituted 10% of the global total, making it the second-largest contributor to global BC after China with 1365 Gg/y (~35% of emissions). However, in another study, Bond et al. (2007) found that the BC emissions from coal use increased from 28 Gg (in 1950) to 55 Gg (in 2000), a ~95% increase. However, this increase was due to an actual 1100% rise in coal usage during this period. It indicates the increased efficiency of coal use and thus lowering emission factor. Moreover, Lu et al. (2011) found increased energy consumption from 1996 to 2010, increasing BC emissions. The growth in BC emissions in India, unaffected by control technologies, was primarily governed by energy consumption. The resulting emissions of BC are summarized as shown in Table 2.1.

Table 2.1 Black Carbon emissions in India from 1996-2010 in Gg/y (Lu et al., 2011).

Emission sources	Year				
	1996	2000	2004	2008	2010
Agricultural and waste burning	60	56	59	71	74
Biofuel	338	373	426	449	454
Coal	117	172	209	276	295
Forest and Savannah burning	19	17	19	16	19
Industry	155	168	198	217	227
Oil	117	126	124	153	159
Power plants	3	4	4	5	5
Residential	402	421	481	563	579
Transport	80	88	88	107	111
Other	8	10	12	14	15

Gustafsson et al. (2009) employed radiocarbon (14C) techniques to determine the contribution of different sources in Maldivas and Singhagad, west India. This study found that more (68%) soot carbon represents an unmanageable portion of BC spectrum from biomass than fossil fuel combustion. However, more (54%) elemental carbon (EC) arises from fossil fuel combustion.

Lyamani et al. (2011) investigated BC concentrations in an urban area, which varied daily. They attributed the large variability in BC concentrations to variations in emission sources and meteorological conditions. Further, a reduction in the concentration of BC was also observed, attributed to a decrease in traffic-related emissions. The winter concentrations were double the summer concentrations, more likely due to emissions caused by domestic heating, less vertical mixing, and lower wind speeds. The articulated diurnal variation observed during the study period was consistent and was mainly ascribed to the atmospheric boundary layer's daily evolution and local anthropogenic activities.

Trompetter et al. (2013) suggested BC as a good proxy for combustion-related PM concentrations. BC's vertical extent and profile show that it is mainly bounded by a surface layer less than 50 m in height from the surface. Surface-based thermal inversion strengthens during the night resulting in the decrease of mixing height and volume of atmosphere available to BC for dispersion, which aggregates the observed pollution episodes at ground level. Inversion events in the confined valley are the significant reasons for enhanced

concentrations of BC during the late evening.

Zha et al. (2014) studied and found that $PM_{2.5}$ has about 5.29% of BC. However, this observation was based on short-term data. Local pollution sources mainly contribute to BC. Fossil fuel usage is considered a significant source of BC apart from BB burning.

2.3 Impact of atmospheric Black Carbon

2.3.1 Vehicular emissions

The primary source of particulate pollution is traffic emissions (Gokhale and Raokhande, 2008). Using a mobile laboratory, Schneider et al. (2008) performed an in-situ study of various traffic-related emissions under real-atmosphere cruise conditions. The results show that traffic emitted particles are dominated by Black and Organic Carbon in the aerodynamic vacuum diameter below 200 nm. The different size modes were distinguished with the Aerodyne aerosol mass spectrometer. The highest BC and OC mass concentrations were found in the inner city traffic, while the highest particle number concentrations were observed during truck chasing on motorways.

Invernizzi et al. (2011) conducted a BC monitoring in Milan, Italy, in three main radial roads connecting the outskirts to the city center, each with three segments: including an outer one with no traffic restrictions, an intermediate one subjected to the traffic congestion charge (denoted as Eco pass) where a ticket is required to enter for cars equipped with engines before Euro 4 standards, and the pedestrian zone in the city center, where each of the three main roads ends. A sharply declining gradient in BC concentrations from the outer zone, without traffic restrictions, was observed to the more central areas for all three radial main roads. These results suggest that BC is a more relevant metric of traffic pollution and should be considered in demonstrating the effectiveness of air quality mitigation measures.

A field study conducted by Liang et al. (2013) at the highway segment has described the role of the local wind field and microclimate conditions in the near road BC transport, concentration, and composition. Microclimatic factors and traffic flow strongly correlate when their diurnal patterns are investigated. The initial vertical dispersion at the road caused due to plume rise in response to the wind-traffic interactions is significant and needs further

attention.

For comparative analysis, Song et al. (2013) carried out a study simultaneously at three different sites near a road, urban and rural. A higher concentration was observed at the roadside site than at urban and rural areas, indicating that vehicle emissions may be a significant source. In summer, a strong correlation was observed between the diurnal variations of BC at the roadside and the patterns of heavy-duty diesel vehicles. The BC/CO ratio played the role of a marker that helped indicate the contribution from $HDDV_s$, especially at night time of summer season. The main focus of the study was to highlight the contribution of $HDDV_s$ towards BC and PM.

Takahama et al. (2014) observed that BC mass and number size distribution has the presence of three modes BC containing particles: below 100 nm, near 100 nm, and between 200 and 300 nm BC diameter. The urban activities generated the most significant mode during the evening hours. The study also focused on adjacent areas traffic patterns and composition, impacting the BC concentrations depending on the prevailing wind direction. It was observed in the case of diesel-driven vehicles; the significant contribution is coming from the ten years and above category.

Barman and Gokhale (2019) studied the impact of traffic on BC concentration at two locations with varying traffic volumes in Guwahati. Light commercial, heavy-duty diesel vehicles, and two-wheelers were the most significant contributor to BC. This study observed comparatively higher BC concentrations at high traffic than low traffic locations. This study also found that the BC emissions from vehicles were increased to 0.44-0.55 Gg (2018) from 0.29-0.33 Gg (2011).

Emission factors are highly flexible and depend on the combustion engine's technology and particulate reduction equipment fitted out in automobiles (Bond et al., 2004; Yan et al., 2011; Myung and Park, 2012). Depending on the technology of combustion engines and dust reduction equipment employed on automobiles, BC emission factors (EF_{BC}) are expected to be highly variable. Novakov et al. (2003) assumed a linearly decreasing diesel EF_{BC} for developed countries from 1965 to 1985. The assumption made was that the diesel EF_{BC} in developing countries remained 10 g kg^{-1} throughout the period for the countries such

as India and China. Bond et al. (2004) considered the decrease of EF_{BC} for gasoline and diesel vehicles based on the measured emission factors of particulate matters measured for heavy-duty vehicles in the United States of America. They estimated the trends in BC emissions from motor vehicles. Wang et al. (2009) calculated the fleet average emission factors based on the data collected during the on-road measurements during the 2008 Beijing Olympic Games. By performing a carbon balance over the fuel combustion process, one can relate carbon-containing species' emissions from vehicle exhaust to fuel consumption. The derived emission factors for different types of individual vehicles and the fleet average emission factors are shown in Table 2.2.

Wang et al. (2012) tested several factors other than vehicle type for their effects on log EF_{BC} using analysis of variance. Among these factors, vehicle model, year, and country were significant ($p<0.05$) for log EF_{BC} of gasoline vehicles. They recognized that EF_{BC} decreased over time due to advances in control technology and tightening of emission regulations. They established that GDP is a good indicator reflecting variation among countries in terms of BC emission, citing the relationship between economic growth and technology evolution.

Takahama et al. (2014) reported the effect of vehicle mileage and vehicle type based on the fuel usage, such as diesel or gasoline. In the case of diesel-driven vehicles, the significant contribution comes from the ten years and above category.

Paliwal et al. (2016) developed an inventory of BC emissions in India at the district level. It was spatially distributed onto grids at a resolution of 40×40 km^2. The uncertainty in emissions has been estimated using a Monte Carlo simulation by considering the variability in activity data and emission factors (Table 2.3). In total BC emission, domestic fuel contributed most significantly (47%), followed by industry (22%), transport (17%), open burning (12%), and others (2%).

Table 2.2 On-road emission factors for different types of vehicles (Wang et al., 2009).

Vehicle type	Number of vehicles	BC (g kg-fuel^{-1})
Diesel trucks	19	1.0 (0.6-4.3)
Diesel buses	30	0.5 (0.3-0.9)
Euro III Natural gas bus	1	0.2
Gasoline trucks	6	0.9 (0.6-1.1)
High-speed diesel van	1	6.8
New diesel trucks	1	0.3

Table 2.3 Emission factors of Black Carbon for the transport sector in India (Paliwal et al., 2016).

Vehicle type	Emission factors (g km^{-1})
Two-wheeler	0.02 ± 0.01
Car	0.09 ± 0.06
LMV	0.15 ± 0.01
LCV	0.19 ± 0.07
Bus	0.49 ± 0.24
Truck	0.34 ± 0.17

2.3.2 Biomass burning

It can be seen from Table 2.4 that transportation sources show the lowest OC/BC ratios. In contrast, biomass burning categories are dominated by organic carbon emissions, and industrial sources are somewhere in the middle. All these sources also emit CO_2 and greenhouse gases, and sulfur emissions. The sulfur emissions transform into SO_2, NO_x emissions into nitrates, and contribute to ozone and other particles.

Table 2.4 Global Black and Organic carbon emissions from six source categories (Lamarque et al., 2010).

Source category	BC (Gg)	OC (Gg)	OC/BC
Energy/Power	54	368	7
Industry	1497	2249	2
Transportation	1340	1447	1
Domestic	1947	7746	4
Open biomass burning	2755	23868	9
Solid waste	35	47	1
Total	7628	35725	4.7

Fig. 2.1 shows that 35% of the total global emissions of Black Carbon are from biomass burning, while the domestic or residential sector contributes 25% of the worldwide total. In developing countries, most residential emissions come from cook-stoves than burning biomass, dung, or coal resulting in significant emissions of BC. India, China, and Africa contribute nearly two-thirds of the total BC emissions from biomass.

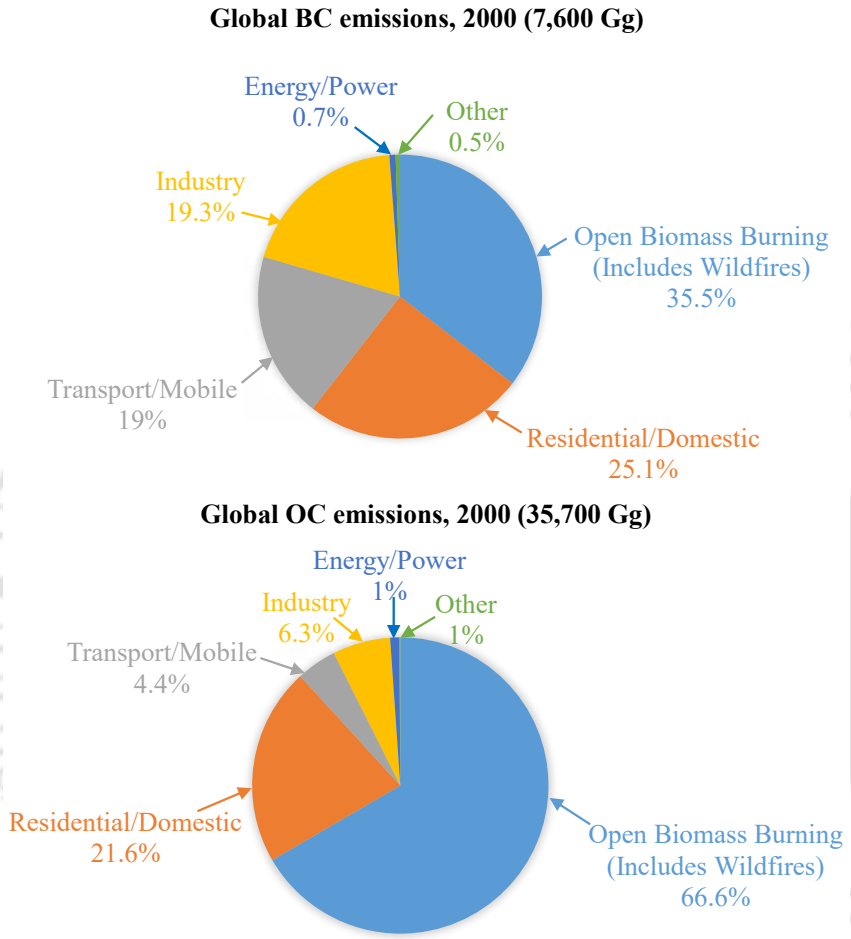

Fig. 2.1 Global distribution of Black and Organic Carbons emissions by major sources categories (USEPA, 2012).

Fig. 2.2 shows the BC emissions around 37 world regions. It can be seen that countries like India, China, and United States are dominated by anthropogenic sources, whereas Africa, Brazil, and Australia are dominated by open biomass burning.

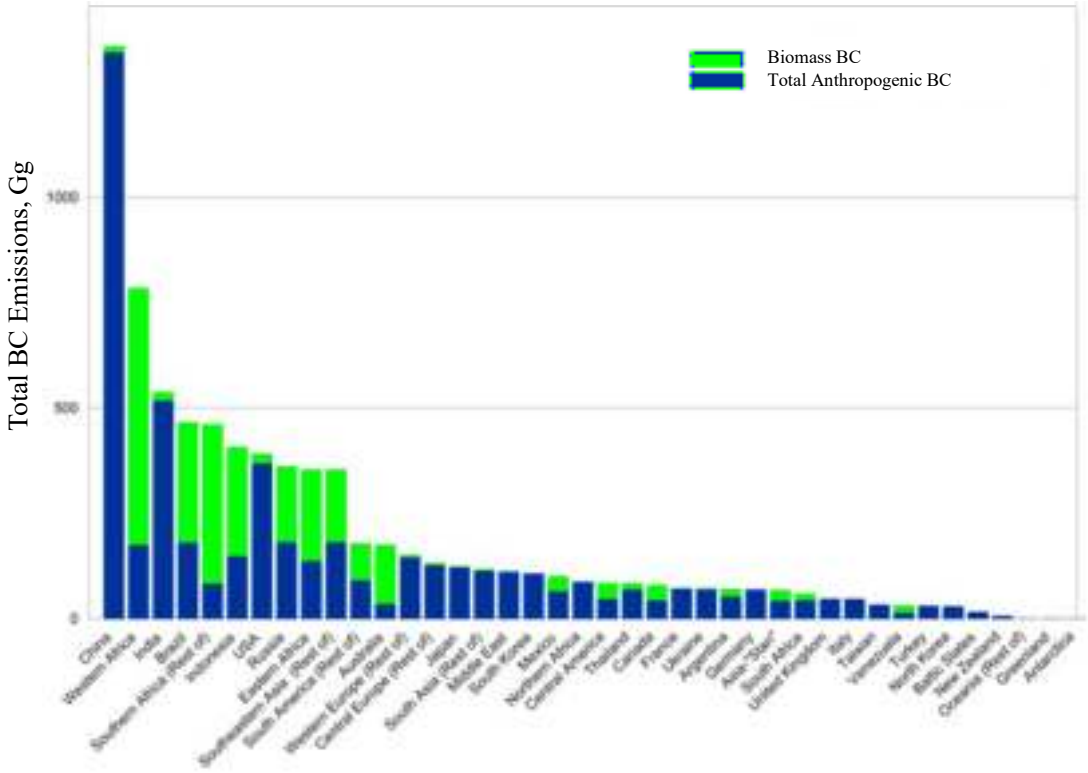

Fig. 2.2 Black Carbon emissions (in Gg) from two sources worldwide (Lamarque et al., 2010).

The residential in India do not have fireplaces, unlike other European and American countries. The uncontrolled open burning of softwood, hardwood, papers, agricultural waste, etc., for cooking and heating purposes, especially in winter, is common in rural and suburban areas. Several measures have been taken in urban and rural areas in the past years to reduce air pollution, focusing on household emissions. The Government of India, in March 2011, launched a National Carbonaceous Aerosol Programme to study regional carbonaceous aerosols, including atmospheric transformation processes, sources, and impacts on climate, clean air, and the ecologically sensitive Himalayas (INCCA, 2011). In January 2019, the Government of India launched another National Clean Air Programme to reduce PM_{10} and $PM_{2.5}$ by about 20 to 30% by 2024, which targets 122 non-attainment cities (NCAP, 2020). The Government of India rolled out several schemes to reduce carbon particles, including improved cook-stoves and LPG for cooking in suburban and rural areas. These schemes have reduced the consumption of kerosene.

2.4 Impact on climate

Black Carbon (BC) influences the climate in three ways: direct, semi-direct, and snow albedo. It has a dominant influence on global warming due to its strong radiation absorbance characteristics. It absorbs radiation at different wavelengths (370-880 nm) and thereby contributes to global warming as a direct effect. It has a semi-direct impact on cloud formation and precipitation by acting as base nuclei for cloud condensation. BC will hinder the droplet formation, size, and number distributions that cause clouds' reflectivity (Jacobson, 2004). BC also reduces the albedo of snow and ice, which results in accelerated melting (Warren and Clarke, 1990) in the sensitive region such as the Arctic and the Himalayas. It also affects nutrient retention time and plays a significant role in soil biogeochemical processes. BC can absorb a million times more energy than CO_2 and is the third-largest contributor to global warming (Bond and Sun, 2005). In addition to climate change, BC emission reduction can avoid over 1.6 million premature deaths from inhalation of smoke from indoor cooking (Rehman et al., 2011). Fig. 2.3 shows the possible effects of BC on climate compared to greenhouse gases (For example, CO_2).

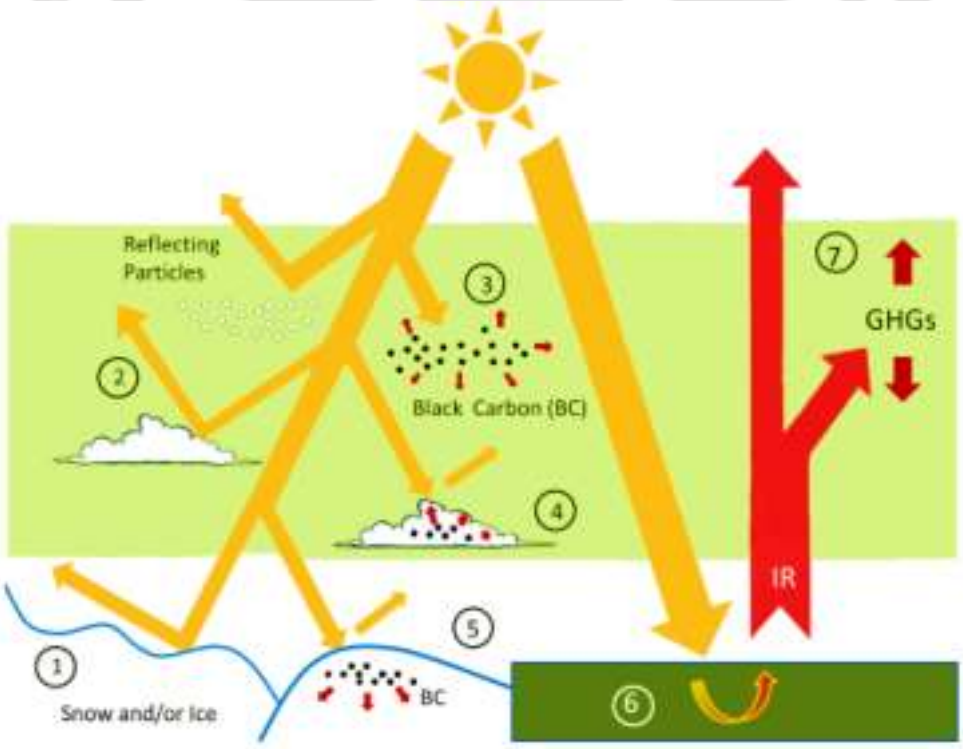

Fig. 2.3 Effect of Black Carbon on climate as compared to greenhouse gases (USEPA, 2012).

1. Penetrated sunlight reflects off from snow and ice.
2. Non-light absorbing clean clouds or transparent particles reflect sunlight, thereby reducing absorbed solar energy by the surface.
3. Suspended BC absorbing incoming solar radiation and warming the atmosphere.
4. BC laden clouds absorbing more solar energy than normal clouds become of short life span and less likely to precipitate.
5. BC laden snow and ice absorb more solar energy than the normal one, accelerating melting speed.
6. Earths surface absorbs incoming solar radiation and reflects it into the atmosphere as infrared radiations.
7. Partial absorbance of infrared radiations by greenhouse gases and re radiating back to earth resulting in global warming.

2.5 Impact on human health

Atmospheric BC is closely related to health impacts (Magalhaes et al., 2018; WHO, 2012). When inhaled, BC is deposited in the lungs via the respiratory system causing significant acute health effects and premature deaths (Jansen et al., 2005; WHO, 2012). The internal lung surface area of the human body ranges from 130 to 180 m^2, while it has also been reported that 1 m^2 kg^{-1} body weight is a real value for the lung surface of mammals (Fröhlich et al., 2016). The BC particles have a very high surface area of about 74 to 89 m^2 g^{-1} (Hammes et al., 2008). BC can either cause health effects or act as a carrier of chemical species (Wang et al., 2014). Its small size, irregular morphology, and notably bulky surface area facilitate the absorption of atmospheric volatile organic compounds and polycyclic aromatic hydrocarbons and enter deep into the bronchial tree (Jansen et al., 2005). BC exposure and health risk outcomes are linked with cardiovascular health effects, neurodevelopmental behavioral intellectual disorders in newborns and contrary birth consequences, and breathing mortality and morbidity due to long-lasting disruptive respiratory infection, lung cancer, asthma (Matt et al., 2004; Wu et al., 2018). Some studies expressed the special health effects of BC effluence in an equal number of daily passive-smoking cigarettes (PSCs), built on

the existing epidemiologic evidence (Van der Zee et al., 2016). Van der Zee et al. (2016) described the health risk exposure to 1 μg m^{-3} (of BC) being ~4 PSC day^{-1} for similar health consequences. This study includes Lung cancer (LC), Cardiovascular mortality (CM), Low Birth Weight of infants (LBWI), and Lung function decrement in children in % (PLFD), respectively. Using this approach, Wu et al. (2018) studied the health risks in terms of passive cigarette equivalents w.r.t. the possibility of LC, CM, LBWI, PLFD, individually in Tibetan Plateau (Qinghai), Pani et al. (2020) over an urban region (Chiang Mai), Thailand in north peninsular, and Ambade et al. (2021) over Jamshedpur, an urban site in eastern India.

2.6 Impact due to COVID-19 related shutdown

The COVID-19 pandemic forced partial or complete lockdown leading to the sudden closure of anthropogenic activities. The lockdowns were lifted gradually, and the actions were successively increased. During the lockdown, the total or partial shutdown of anthropogenic activities (stone quarries, road construction, open burning of biomass, hill cutting, vehicular movement, etc.) improved the air quality concerning $PM_{2.5}$, PM_{10}, BC, NO_2, SO_2, CO, NH_3, and O_3 pollutants in Indian mega-cities, e.g., New Delhi (National capital region), Kolkata (Eastern India), Mumbai (Southern India) (Chowdhuri et al., 2020; Goel et al., 2021; Mahato et al., 2020; Kumari and Toshniwal, 2020) and $PM_{2.5}$ worldwide (Chauhan and Singh, 2020). The lockdown also reduced India's aerosol optical depth (AOD); nearly 45% of the AOD dropped during lockdown periods (Ranjan et al., 2020). In a study by Mahato et al. (2020), PM_{10} and $PM_{2.5}$ concentrations decreased by about 60% and 40%, respectively, throughout the initial lockdown (LD1: March 25-April 14) in the National capital region (Delhi) as compared to 2019. Chowdhuri et al. (2020) reported a significant decrease in a lightning flash by about 49% in summer because of lockdown in Kolkata, India. Pathak et al. (2021) assessed the impacts of lockdown over the upper Brahmaputra river basin (Dibrugarh) of Northeast India. They observed that the air quality in respect of O_3, NO_2, NO_x, CO, SO_2, PM_{10}, $PM_{2.5}$, PM_1, and BC improved moderately during lockdowns compared to 2015-2019. Gogoi et al. (2021) reported a decrease in BC by about 60% and about 30% over Indo-Gangetic plain and Northeastern India, respectively, during LD2. It also found that the BC was high over the IGPs and Northeast India compared to the rest of India. The COVID-19 amid lockdown also reduced the air impurity levels (by 30-50%) in the neighboring region

(Southwestern China) (Chen et al., 2020) and other areas in the world (Chauhan and Singh, 2020).

2.7 Impact of meteorology on Black Carbon

Cao et al. (2010) measured BC concentrations in the southeast Tibetan Plateau along the valley of the Yarlung Tsangpo river during winter period, November 2008 to January 2009. This study found that the mean concentration of 0.75 μg m^{-3}, which was much higher than the concentrations measured in the background and remote regions (0.004 to 0.34 μg m^{-3}). Further analysis suggested that the major contaminating sources were from the BC emissions in eastern Indian and Bangladesh. The heavy emissions in China had no substantial effects on the southeast Plateau in winter due to west prevailing winds. It also found that Yarlung Tsangpo river valley causes a leaking-wall, whereby under certain meteorological conditions, BC particles are being transported up onto the glacier. The analysis suggested that leaking-wall effect cannot occur when the prevailing winds were north-west winds, during which the transport along the valley of the Yarlung Tsangpo river was obstructed. As a result, large variability of BC concentration was observed due to change of prevailing wind directions. Coincidentally, it is upper stream of the Brahmaputra river and hence these glaciers have an impact on origins of Brahmaputra river.

Chakrabarty et al. (2012) conducted BC measurements for a week during January to February 2011 in Guwahati, India, the largest city in the BRV region. This study found that the diurnal variation of BC coincided with the diurnal variability of local weather parameters. High BC concentrations in the morning hours were attributed to pollutants being trapped near the surface in a residual shallow nocturnal boundary layer. Also, in morning hours, BC concentration was high due to anthropogenic activities including transportation emissions from the morning commute and biomass burning associated with domestic heating. During mid-afternoon, BC was mixed vertically by the deepening boundary layer and dispersed horizontally by higher wind speeds. After sunset, reduced vertical mixing results from sinking boundary layer and consequently BC mass concentrations increased until 20:30 to 23:00 LST as emissions were trapped near the surface. All anthropogenic emissions are reduced as the night progresses and BC concentrations decreased slowly.

Safai et al. (2014) monitored BC constantly at Pune, India from January to December 2005. This study reported that BC concentrations were maximum (∼80% more than the annual mean), mainly due to prevailing atmospheric conditions like wind speed. In monsoon season, BC concentrations were minimum (∼60% less than the annual mean) due to washout effects of rain and south westerly winds from marine areas. The morning and evening peak of BC in diurnal variation was related to change in the local boundary layer and the intensity of local traffic emissions.

Sarkar et al. (2015) observed BC aerosols over a high-altitude station in Darjeeling in the eastern part of the Himalayas in India from January 2010 to December 2011. This study investigated the long-range transport of BC aerosols along with the meteorological impacts on these aerosols. In pre-monsoon, the contribution of local emissions (massive tourist activities), long-range transport, and mountain wind transport were 56%, 27%, and 17%, respectively, towards the total BC loading over the study region. Moreover, heavy rainfall during the monsoon resulted in minimum BC concentration due to below-cloud scavenging of BC aerosols.

Barman and Gokhale (2019) investigated the deposition and long range transport of vehicular BC emissions using HYSPLIT model in 2016-17. This study found that the BC emissions originated in the northeastern city of Guwahati, India are transported over and in the Brahmaputra river valley and the Himalayas. This study reported that the deposition of BC in Himalaya was high during winter than the pre-monsoon seasons. The deposition was high in March and subsequently decreased from April to May due to rainy events.

Ambade et al. (2021) carried out BC monitoring from December 2017 to November 2018 at the industrial site in the eastern, India. During monsoon months, low BC concentrations waer reported because of extensive rainfall. The BC concentration were found almost half than the winter season. Correlation analysis has found a strong relationship between BC and $PM_{2.5}$. However, an inverse relationship was noticed between BC and temperature, precipitation, wind speed and humidity during the study period.

Cui et al. (2021) conducted measurements of BC aerosols from December 2019 to November 2020 in the rural environment of Qingdao, Northeastern China. This study found

that the boundary layer height (BLH) influence presented evidently seasonal dependence, while there was no significant seasonality for horizontal wind speed. This study also concluded that the vertical dilution effect would have seasonal dependence with the highest efficiency during winter under high BLH conditions.

Chaudhury et al. (2022) analyzed the BC concentration measured at ten strategic locations in Guwahati, India and reported that the temporal variation of BC concentrations at higher levels followed the temporal variation of the traffic pattern, while the local meteorological fluctuations at the surface level height interfered with this relationship.

2.8 Measurements and methods of quantification

There are no specific instruments to measure BC in the atmosphere because BC is not well defined. Though, two techniques are available, filter-based technique and direct technique. Based on two approaches, the instruments detect all aerosols that absorb light at specific wavelengths. The methods are mentioned what the scientific community is using to measure atmospheric BC. The most common technique is to measure the absorption of BC with a filter-based absorption photometer. The available methods are Particle Soot/Absorption photometers (PSAP), Photoacoustic Spectrometer (PAS), Continuous Light Absorption Photometer (CLAP), Aethalometer (Lack et al., 2014; Drinovec et al., 2015). Above all, Aethalometer measurements are most common nowadays. The concept is similar for all filter-based instruments. While ambient air is filtered, BC is deposited on a filter media, and optical attenuation of transmitted light is measured. The deposited particles related aerosol absorption coefficient (b_{abs}) is calculated by Beer-Lambert law (Weingartner et al., 2003) as given by equation 2.1.

$$I = I_o e^{-b_{abs} \times z} \tag{2.1}$$

where I_o and I denote the intensity of incoming and remaining light after passing through a filter with a thickness of z. This study used the dual spot Aethalometer (AE-33) model for BC measurements and discussed in Chapter 3. Fig. 2.4 shows the measurement of the carbonaceous components of particles.

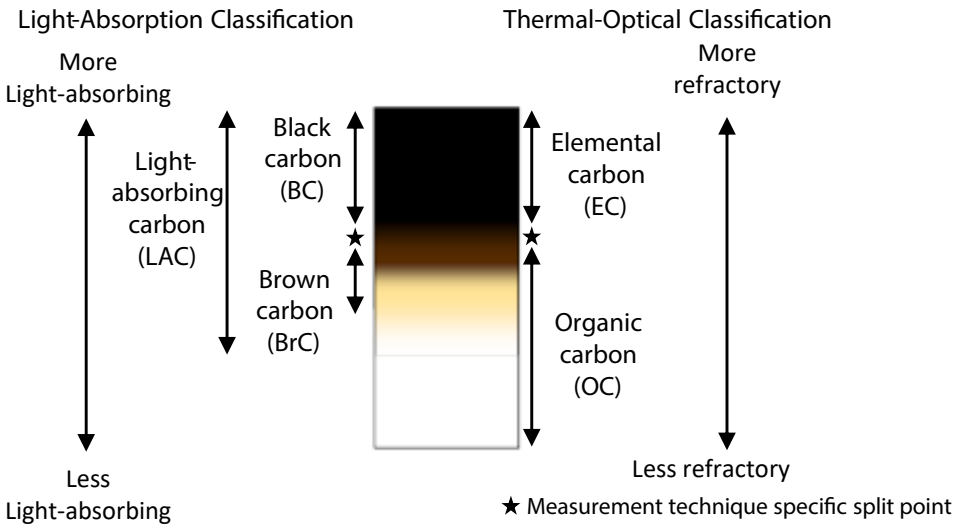

Fig. 2.4 Measurement of the carbonaceous components of particles (USEPA, 2012).

2.8.1 Source apportionment

The Aethalometer (AE-33) model is based on the change in the aerosol light absorption from inadequate burning of fossil fuel (FF) and biomass (Sandradewi et al., 2008). FF combustion has a vast share of BC, whereas BB has a considerable amount of B_rC entirely reliant on burning material (Zotter et al., 2017). The two-component mixing model (AE-33) is sensitive to the presumed Angstrom Absorption Exponent (AAE) values associated with FF (AAE_{FF}) and BB (AAE_{BB}) and also on the spectral choice. A few studies used 370-880 nm (Vaishya et al., 2017; Dumka et al., 2018, 2019; Liu et al., 2018; Mousavi et al., 2018) and others used 470-950 nm (Sandradewi et al., 2008; Barman and Gokhale, 2019).

The AAE values depend on fuel type changes, combustion efficiency, and aging progressions in the near-UV rather than the visible and near Infrared range (Kirchstetter et al., 2004; Bond and Bergstrom, 2006; Stockwell et al., 2016). Dumka et al. (2018), using the site-specific spectral properties in Delhi, estimated the share of both BB and FF to the whole BC. It improved the results significantly compared to the other study using the default Aethalometer setting (AAE_{FF} as 1.0, AAE_{BB} as 2.0) in a similar region (Tiwari et al., 2015). Dumka et al. (2018) used AAE_{FF} as 1.0 and AAE_{BB} as 1.8 for the approximation of the BC_{FF} and BC_{BB} in Delhi, India, likewise Pani et al. (2020) in Chiang Mai, Thailand and Vaishya et al. (2017) in Gorakhpur (IGPs), India. The AAE_{BB} and AAE_{FF} value in the range of 1.68-2.2 and 0.9-1.1, respectively, are used in source apportionment studies (Stockwell et al., 2016;

Zotter et al., 2017; Dumka et al., 2018; Barman and Gokhale, 2019; Pani et al., 2020). The AAE_{BB} strongly depends on biomass and combustion type and can vary up to 3.5 (Dumka et al., 2018; Deng et al., 2020).

2.8.2 Light absorption properties

The optical properties of BC, primary brown carbon (B_rC_{pri}), and secondary brown carbon (B_rC_{sec}) are different. B_rC absorbs sunlight at shorter wavelengths (Andreae and Gelencsér, 2006). Atmospheric B_rC is originated from primary emissions or formed through multi-phase reactions in the ambient air (Laskin et al., 2015). Secondary organic aerosols from BB are more absorptive at shorter wavelengths than the primary organic aerosols (Saleh et al., 2013). Consequently, B_rC_{sec} is a leading contributor to the universal radiative driving budget. The $b_{abs\_B_rC}$ involvement varied typically depending on meteorological conditions and wavelength (from UV to IR). The radiation wavelengths emitted by the sun that reaches the earth begin around 280 nm (UV-B), peak in the mid-visible range, and reach out past 2000 nm (infrared). The shorter the wavelength, the higher its energy (Fig. 2.5a). Fig. 2.5b shows that BC is more effective in absorbing solar energy across the entire solar spectrum than B_rC. When the light absorption curves for BC and B_rC are superimposed upon the solar spectrum, the significance of the different absorption efficiencies between BC and B_rC becomes evident (Fig. 2.5c). It means that BC will absorb more solar radiation than B_rC.

Li et al. (2018) conveyed 10-16% contribution (at 405 nm) in pre-monsoon and 19-15% in winter at rural and urban sites in Guangzhou, China, while increasing in rural areas. Using a similar approach, Qin et al. (2018) reported a $b_{abs\_B_rC\_370}$ value of 13.67 Mm^{-1} along with contributions (~24%) at suburban Guangzhou, and China and Liakakou et al. (2020) also stated a similar B_rC contribution (21.65%) at the urban background of Athens, in winter. In winter, another study conducted by Yuan et al. (2016) presented a ~6% $b_{abs\_B_rC\_405}$ contributions at an urban and ~12% rural location in the Pearl River delta, China. Overall, a summary of the literature review shows generally more outstanding contributions in rural regions due to the more significant influence of BB from agricultural actions.

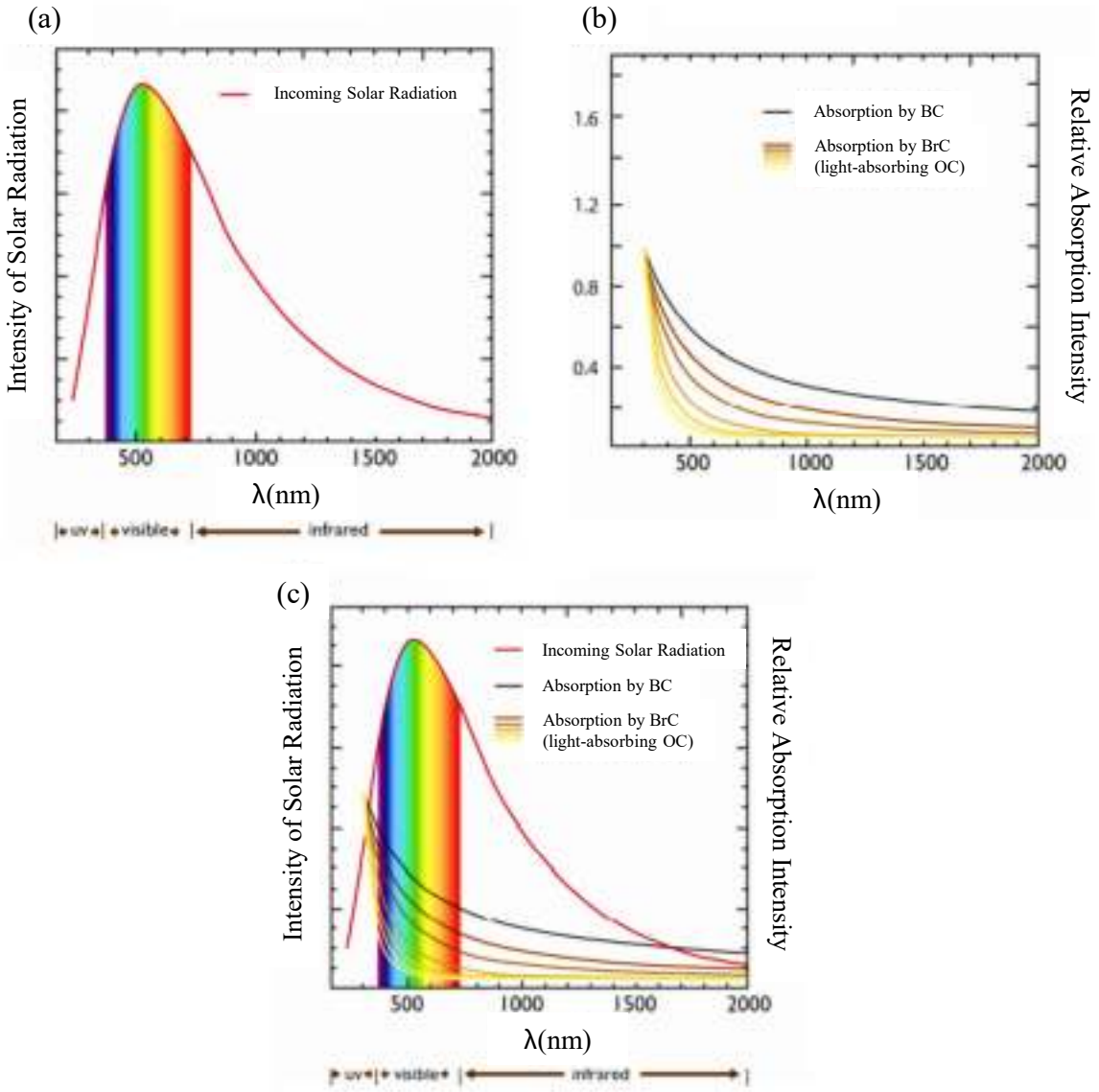

Fig. 2.5 Light absorption by Black Carbon, Brown Carbon, and ambient mixtures (USEPA, 2012).

Another significant point on the distinction between $b_{abs\_B_rC}$ and b_{abs_BC} absorption constituents is the dust involvement on total babs at a shorter wavelength, which can cause overestimation of BB% on dusty days (Liakakou et al., 2020). Zhao et al. (2019) utilized iron (Fe) content and MAC values as well for dust samples to evaluate its influence on entire b_{abs} at a remote place in the Tibetan plateau, resulting in a yearly input of ~4% and ~9% at 808 nm and 405 nm, separately. Another study conducted in Athens revealed an insignificant influence of dust on spectral absorption and scattering properties (Katsanos et al., 2019). Similarly, by considering 166 days with dust events for four years' data in Athens, Liakakou et al. (2020) found that the dust events disturb the estimations of B_rC absorption by ~4%, which are inside the uncertainties of the approximation method (Qin

et al., 2018). Humic-Like Substances (HULIS) initiating from BB absorb intensely at short wavelengths (370 nm), whereas nitro-aromatic compounds engage more at wavelengths greater than ~400 nm (Graber and Rudich, 2006; Satish et al., 2017).

2.8.3 Dispersion modelling

There is rising concern that the natural reserves on the Himalayas are in retreat due to aerosol BC (Barman and Gokhale, 2019), a light-absorbing fraction of carbonaceous aerosols. Across the Himalayan region, substantial biomass-burning (BB), forest fires, and burning of agricultural residues throughout the year add BC to the atmosphere (Tiwari et al., 2016; Prabhu et al., 2020). BC has a considerable warming potential with the rate of warming changes with location and elevation (Ramanathan and Carmichael, 2008). The mountainous and hilly topography experience additional quick variations in temperature than surroundings at minor peaks (Goldreich et al., 1986). Thus, hilly regions with considerable human settlements may substantially impact the BC and its contribution to light absorption.

Forecasting dispersion of particulate pollution in hilly terrain is challenging mainly because of wind-flow patterns. The models such as ISCST (Industrial source complex short term), CALPUFF (unsteady-state Lagrangian puff model), and AERMOD (steady-state UPEPA regulatory model) are widely used for studying dispersion of airborne pollutants (Al-Jeelani, 2013; Huang et al., 2019; Michanowicz et al., 2016; Tartakovsky et al., 2013, 2016; Vaitieknas and Banaityte, 2007; Venkatram et al., 2009). AERMOD is the advanced Gaussian plume model (USEPA, 2021). For near-field applications (less than 50 km), it accounts for airborne pollutant impacts in flat and complex terrain within the same modelling framework (USEPA, 2021; Huang et al., 2019).

Venkatram et al. (2009) estimated the effect of traffic emissions on near-road air quality using AERMOD by interpreting on-site measurements of three VOC species: benzene (C_6H_6), 1,3-butadiene (C_4H_6), and toluene (C_7H_8). The site measurements were taken at high spatially resolved intervals of 10 m to 100 m from the highway in Raleigh, North Carolina, US. The AERMOD performance in modelling the near-road concentrations supported its use for local scale estimations of traffic impacts in the absence of concentration measurements.

Al-Jeelani (2013) studied traffic emissions at Haram Mosque in Makkah, Saudi Arabia.

The study comprised measurements of pollutants including NO_2, SO_2, CO, O_3, PM_{10}, and $PM_{2.5}$ using a mobile laboratory at three locations. Industrial Source Complex-AERMOD (ISC-AERMOD) model was used for numerical calculations and pollutant dispersion. For numerical analysis, pollution dispersion modelled for a one-hour average over four months considering four seasons: winter (January), spring (May), summer (June), fall (September). It was observed that the high-rise buildings acted as a flow obstacle. Mean pollutant dispersion was found in the south and southeast direction in January and June, along with the highest mean concentrations during the same months.

Tartakovsky et al. (2016) studied the dispersion of total suspended particles (TSP) and PM_{10} emissions from five stone quarries in a hilly area east of Israel's coastal plain using AERMOD and CALPUFF. They found AERMOD's predictions better than those obtained by CALPUFF.

Huang et al. (2019) applied the AERMOD model to simulate the dispersal of odor, hydrogen sulfide (H_2S), ammonia (NH_3), and respirable dust from a broiler, dairy, and cage layer barn emissions of the Prairies in Canada. The model predicted the impacts of odor up to about 3 km.

Pandey and Sharan (2021) explores the feasibility of using the AERMOD model as a source-receptor relationship for a point-source identification. This study concluded that the point source is estimated with reasonable accuracy if the AERMOD model is utilized along with the least squares inversion technique for source identification.

A study by Al-Jeelani (2013) of dispersion of traffic emissions of various air pollutants at Haram Mosque in Makkah, Saudi Arabia, using AERMOD, found that high-rise buildings act as flow obstacles. The AERMOD model was also applied to evaluate volatile organics from traffic emissions (Venkatram et al., 2009). Thus, AERMOD is a well-considered air pollutant dispersion model, mostly applied to point sources (about 100 m stack height) in flat terrains (Venkatram et al., 2009; Al-Jeelani, 2013; Tartakovsky et al., 2013) and hilly terrain (Tartakovsky et al., 2016).

2.9 Summary

BC is the product of incomplete combustion of solid and liquid fuel, has high global warming potential, and impacts air quality from local to intercontinental distances. It has measurable effects on atmospheric warming through radiative absorption and scattering and land warming through changes in albedo, which make the BC a potent driver of climate change. Fossil fuel particularly the vehicular emissions contribute to BC. Microclimatic factors, including solar radiation, tend to have a noticeable impact on BC. The confined valleys tend to show an enhanced concentration of BC due to the movement of wind being obstructed by the geographical entities. BC emissions need to be controlled from biofuel combustion and direct vehicular emissions to prevent acute impact on local and regional climate. Epidemiological studies establish the link of cardiopulmonary mortality and morbidity with exposure to BC. According to some toxicological studies BC acts as a carrier of a large number of substances of erratic harmfulness to the mortal group. BC needs immediate attention because of its rising trend and higher global warming potential. A serious concern about BC is due to its impacts on the Himalayan glaciers located in the proximity of the Brahmaputra river valley. Thus, the rise in BC mainly due to rising traffic needs special attention in Guwahati, the most urbanized city in northeast India. The AERMOD model predicts concentrations well in the near-road environment.

The long-range transport, deposition in the Himalayas, and radiative effects of BC are studied (Barman and Gokhale, 2019; Chakrabarty et al., 2012). Guwahati's carbonaceous aerosol characteristics and source apportionment studies are carried out using the default Aethalometer model (Barman and Gokhale, 2019; Tiwari et al., 2016). These studies did not use site-specific properties on the optical characteristics of BC and the B_rC absorption properties. The surface characterization of B_rC found in India, which may help study its impact on climate change, is not found in the literature. Also studies on the surface characterization of B_rC, both primary and secondary, for the BRV region are not found.

3

Field Work and Research Methodology

The data for carrying out the research have been collected in the study region for the winter season from Jan-Mar 2020 as per the standard methodology (CPCB, 2011). The other necessary allied data were taken from the project entitled "Urban Black Carbon - Global Impacts and Local Mitigations" funded by the Science and Engineering Research Board (SERB) of Department of Science & Technology, Government of India (Grant No: EMR/2014/001039). The methodology adopted in this research has been shown in Fig. 3.1.

3.1 Description of the study region and selection of monitoring locations

Northeast India (NE-I) is a transitional region between the Indian Himalayan Region (IHR) and the Indo-Gangetic plains (IGPs). It is recognized as one of the passages over which airborne contaminants are transported to Eco-sensitive Himalayan margins, especially during the winter season (Barman and Gokhale, 2019). The mighty Brahmaputra river has cut through IHR to escape into the greater plains such as northeast India and Bangladesh via Tibetan Plateau. Hence, the sampling site falls in the lower Brahmaputra River basin (BRB). Guwahati is the largest city and the only gateway to the northeast India. It is also a part of the Indo-Burma biodiversity hotspot. This city is hugely congested and overpopulated; the population of Guwahati in 2011 was around 1.1 million, and population density was 2900 persons per km^2. The narrow streets of Guwahati with frequent traffic jams add a huge quantity of fine particulate matter originating from incomplete combustion of fossil fuel (Barman and Gokhale, 2019).

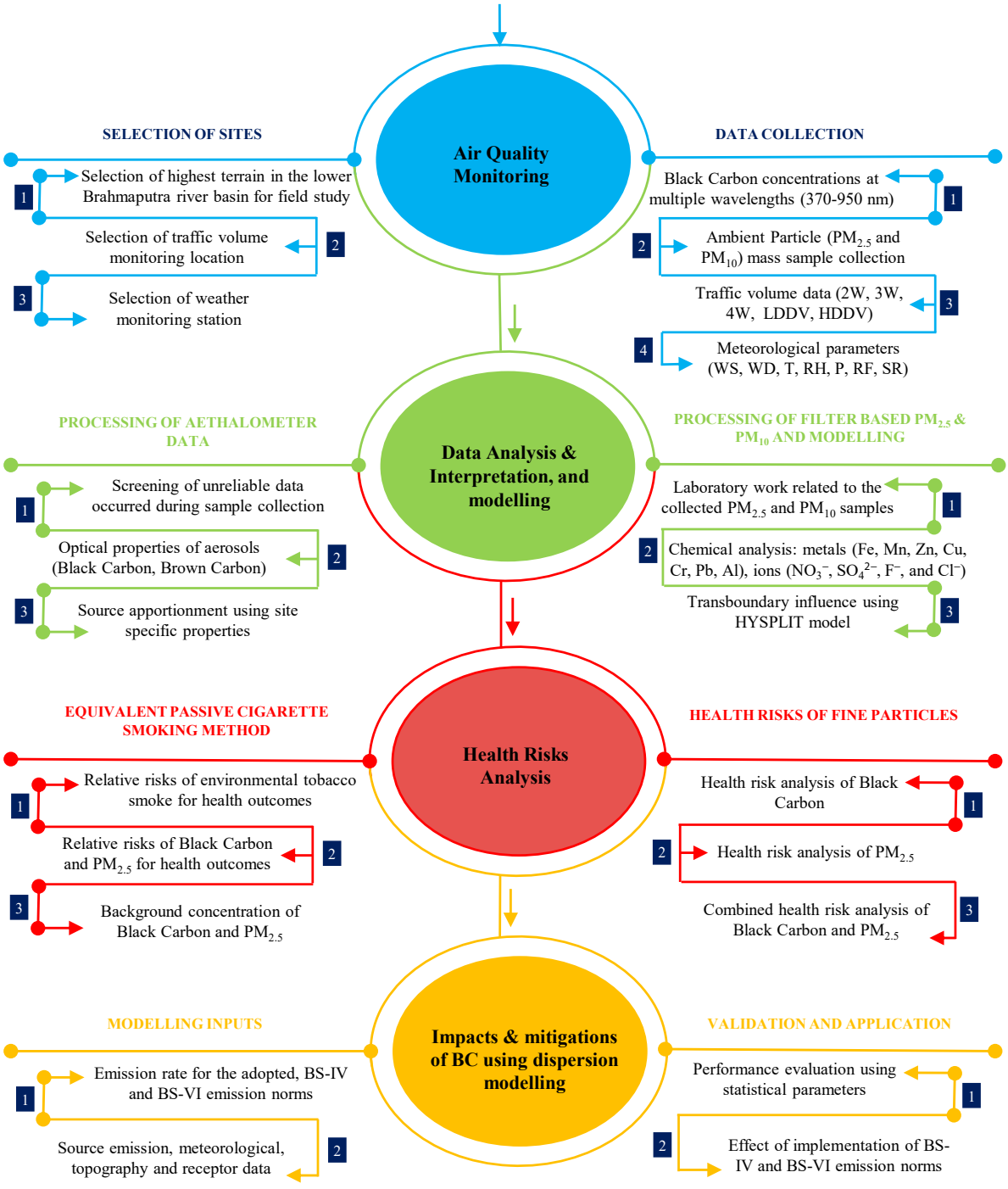

Fig. 3.1 Flow chart of research methodology.

The large vehicle population in Guwahati, particularly the heavy-duty diesel vehicles (Barman and Gokhale, 2019), and 2-wheelers are the prime sources of BC emissions, besides open burning biomass. Heavy Duty trucks (Mining-Dumper, Tipper Lorry, Freight-Trailer, etc.) are allowed from late evening to late morning since these are the only roads to enter the other NE-I states. However, buses, mopeds, light-duty diesel automobiles, and two- and three-wheelers are not restricted, which leads to dense traffic congestion. Because of its land-locked geography, during winter, there is often an accumulation of airborne pollutants in the lowermost layer leading to bad air quality (Chakrabarty et al., 2012; Tiwari et al., 2016). In this study, the study area is referred to a complex terrain due to this regions characteristics.

A real-time BC measurement campaign was carried out in Guwahati in Assam, northeast India, from January to March 2020 (winter season). It is located in a lower Brahmaputra River basin of NE-I. The sampling train was positioned on the top floor of a hospital building (∼11 m above the highest terrain) of Maa Kamakhya Temple on the Nilachal hills (91.71°E, 26.16°N, 225 m above mean sea level). The Kamakhya temple is an autochthonous place of worship and an important pilgrims destination. The pilgrims come to this place annually on a mix-proportion of vehicles. Many small vendors' stalls, shops, a health care center, and residential houses are located near this station. Many people, thus, may be exposed to higher levels of traffic-related air pollutants. Besides vehicles, the rural habitation in the area has open biomass burning for heating (mainly in winter), agricultural remaining, and cooking purposes. The nearby sources of local emissions were cement and brick kilns industries in the surrounding with a trafficked National highway - NH27 and NH427 at a distance of ∼3.5 km to the west and NH427 at ∼2 km to the north at 51 m elevations. The location of the study region and two monitoring sites in Guwahati are shown in Fig. 3.2 and Fig. 3.3.

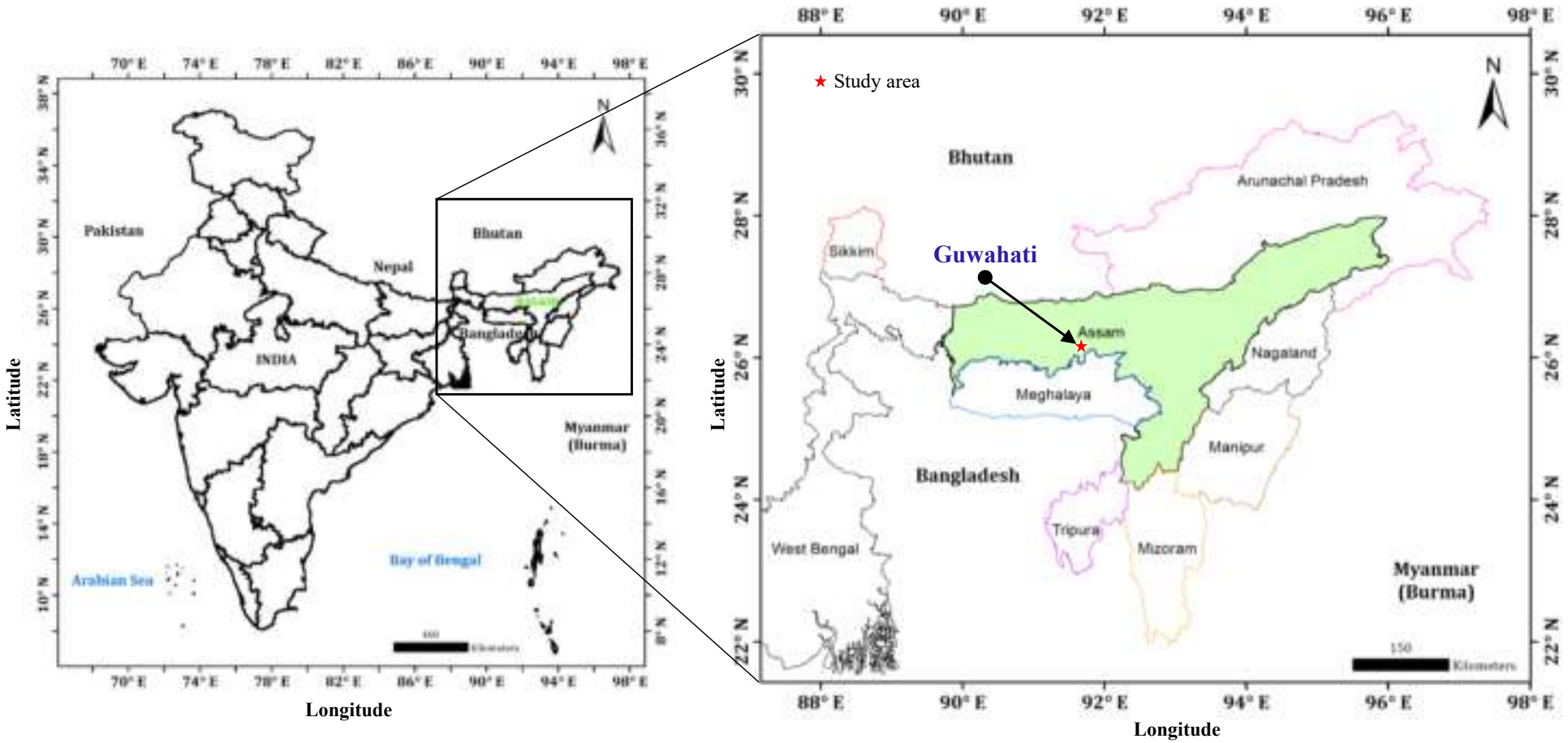

Fig. 3.2 The Guwahati (XY, solid red star) location in Assam, Northeast India, and neighboring regions (Drawn with ArcGIS v10.6.1).

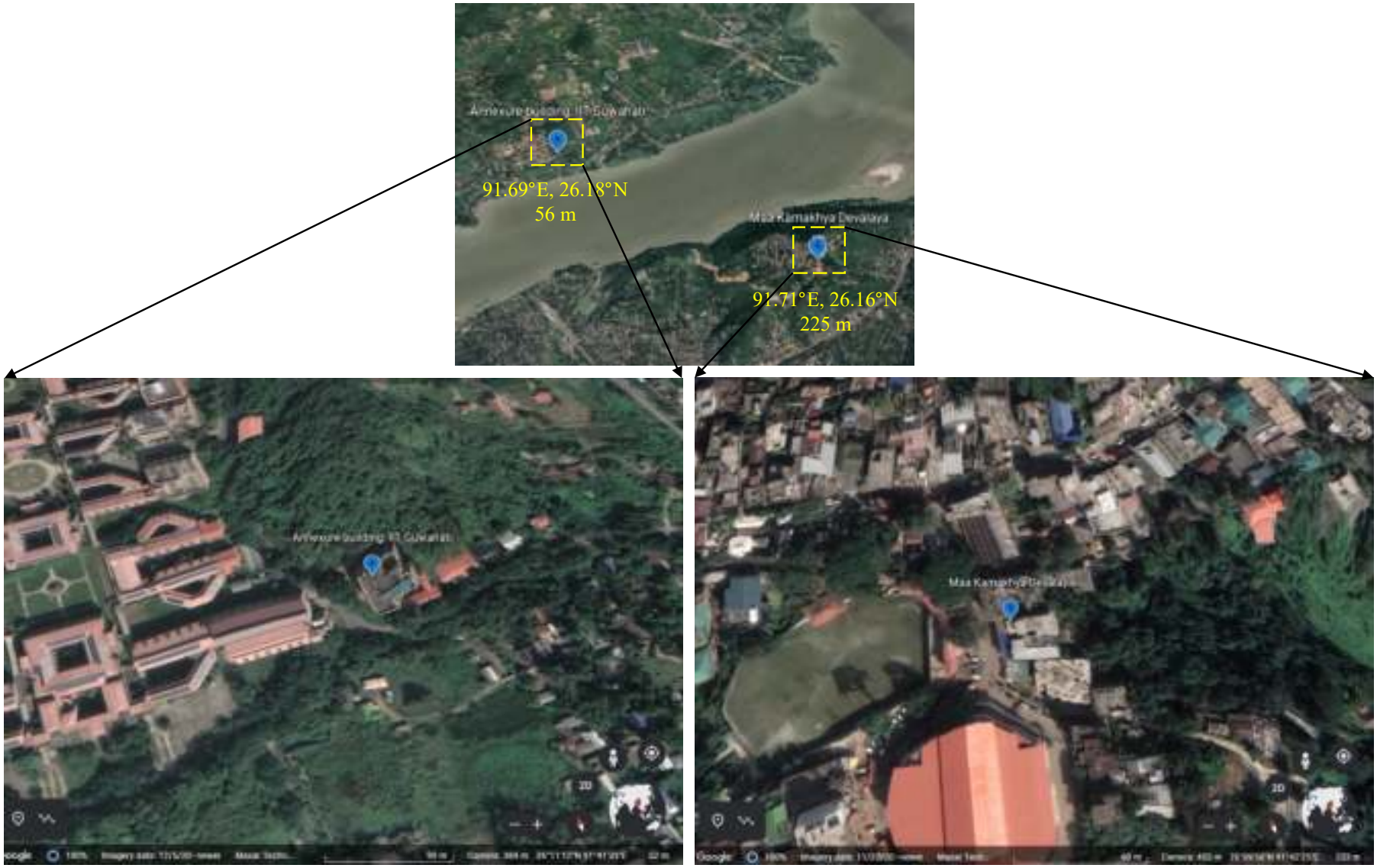

Fig. 3.3 Two monitoring location in Guwahati, Northeast India (Source: Google Earth).

3.2 Field work

The field work was carried out to collect the primary data on the concentration of pollutants such as BC, $PM_{2.5}$, PM_{10}, meteorology, and traffic characteristics during the period from Jan to June 2020, covering two seasons. The pollutant concentration measurements were carried out for at least two weeks each month. The traffic volume study was carried out for two weeks, and meteorological monitoring was carried out for the entire study period. The whole setup mentioned above was synchronized daily and checked for the appropriate flow rate to ensure the data quality. All the instruments were equipped with a backup power supply, which powered them for nearly 15 minutes during the electricity interruption period. The standard guidelines given by the Central Pollution Control Board (CPCB) of India for monitoring pollution data were followed (CPCB, 2011). Table 3.1 shows the list of different parameters collected at two locations.

Table 3.1 Summary of data collected at two locations in the Brahmaputra River Valley region, Northeast India.

Location name	Elevation [msl]	Period	Parameters
Kamakhya hill top	225	Jan to March 2020	Black Carbon, $PM_{2.5}$, PM_{10}, Traffic data
IIT Guwahati	56	March to June 2020	Black Carbon, Meteorology*

* It is continuously recorded from Jan to June 2020 at IIT Guwahati.

3.2.1 Measurement of ambient Black Carbon concentrations

The aerosol light absorption was measured using a dual spot multi-wavelength Aethalometer (Model number AE-33, Magee Scientific Inc., Berkeley, CA, USA) at wavelengths (λ) of 950, 880, 660, 590, 520, 470, 370 nm. It measures the light attenuation (threshold of 120) from LED lamps at multiple wavelengths with a typical half-width of 20 nm. The two-spot (0.79 cm^2) - measurement technique eliminates filter-matrix scattering and non-linear loading effects. BC was sampled at a flow rate of 0.12 $m^3\ h^{-1}$ over a $PM_{2.5}$ cut cyclone and rain/insect guard with a minimum detection limit of 0.005 $\mu g\ m^{-3}$ and its uncertainty of 10%. Drinovec et al. (2015) give more details on its operation. The filter tape roll (30 mm × 10 m) of TFE-coated glass fiber filters (M8060) was used for sampling. The multiple-scattering-enhance factor was set to 1.57, and AE-33 was operated as per recommended surrounding conditions listed in the AE-33 model user manual. The 1-min raw data obtained

from AE-33 was screened for zero, negative, and unreliable values; missing values occurred during the instruments internal calibration (e.g., optical stability test, tape error, clean air test) and averaged hourly. Further, the aerosol absorption coefficient (b_{abs} in Mm^{-1}) and Black Carbon concentrations (in $\mu g\ m^{-3}$) were not calculated for such bad raw data, which affects the hourly values on a few days.

To control the COVID-19 epidemic, a lockdown in Northeast India was announced by the Indian government. The entire setup mentioned above was installed at the rooftop (∼12 m above the ground level) of the Air and Noise Pollution Laboratory, Department of Civil Engineering, IIT Guwahati (Fig. 3.3). BC mass concentrations and meteorological parameters were recorded on the university grounds of IIT Guwahati during the COVID-19 pandemic lockdown. The COVID-19 pandemic forced partial or complete lockdown leading to the sudden closure of anthropogenic activities. The lockdown in four phases and the limitations in several activities started from March 24 to May 31, 2020. Each stage had a different relaxation scale in several essential activities such as public transportation and essential industries opening. Hence, the sampling was also done in six different stages: pre-lockdown (February 12- March 21), lockdown 1 (March 25 to April 14), lockdown 2 (April 15 to May 3), lockdown 3 (May 4 to 17), lockdown 4 (May 18 to 31), and post-lockdown (June 7 to July 3 2020). The lockdown period was divided into different phases based on the measures taken and the standard operating procedures issued by the Indian government to extend the lockdowns from time to time, depending upon the situation of the pandemic. The lockdowns were lifted gradually, and the actions were successively increased. This lockdown period allowed analyzing the variation in the concentration and sources of Black Carbon in the fastest growing city situated in a small to the steep-sloped hilly region of the Brahmaputra valley, Northeast India.

3.2.2 Measurements of ambient $PM_{2.5}$ and PM_{10} concentrations

$PM_{2.5}$ and PM_{10} samples were collected from Jan to Mar 2020 using a low volume fine particulate sampler equipped with the corresponding particle size impactor (model: Envirotech APM 550M). This instrument is designed for simultaneous offline measurements of two-particle sizes at a flow rate of 1 $m^3\ hr^{-1}$. Everyday samples were collected on pre-desiccated Teflon filter tapes (2 μm, 46.2 mm Dia., Whatman, USA) and analyzed

gravimetrically using an electronic weighing balance (model: Sartorius CD-225D, Germany, sensitivity: ±0.001 mg) in a temperature and relative humidity-controlled room. The filters were weighted thrice before and after sample collection. The residual mass was obtained by deducting the mean of post- and pre-sampling weights. Afterward, filters were kept in PTFE cassettes in the zipped pouch at –4°C before chemical characterization.

3.2.3 Chemical analysis of $PM_{2.5}$ and PM_{10} samples

The chemical analysis was performed to the $PM_{2.5}$ and PM_{10} samples for the quantification of metals and ions. The analysis of the PM samples was carried out separately from Apr to May 2020. As we had only one filter paper and were required to analyze both metals and ions, the sampled Teflon filter was carefully cut into two halves. A one-half portion of each sampled filter was extracted twice in 5 ml ultrapure (resistivity: 18.2 Ωm.cm at 25°C) water for 30 min to get water-soluble ions. The total solvent extracts (10 ml) were filtered using 0.2 μm PVDF syringe filters and analyzed using ion chromatography (model: IC, Metrohm 792 basic IC, Switzerland). Multi-element standard solution (Centipur, Merek, Darmstadt, Germany) of anions was used in different concentrations for a five-point calibration. In total, four anions: nitrate (NO_3^-), sulfate (SO_4^{2-}), fluoride (F^-), and chloride (Cl^-) were measured. The method for detection limits NO_3^-, SO_4^{2-}, F^-, and Cl^- were 0.02, 0.02, 0.05, 0.03 μmol L^{-1}, respectively. The accuracy of the method was studied through recovery tests. Ion recovery efficiency and reproducibilty were determined by spiking the known amount of ion mass on the unexposed filter paper, extracting it, and analyzing it on IC. Ion recovery for all species was between 88 and 104% (accuracy: 4-12%), and precision was within 5% of the known concentration. Due to a technical error in the instrument, cations were not analyzed.

For metals, a remaining half portion of the filter sample was digested in a mixture of 2.5 ml HNO_3 (nitric acid) (~69% w/w), 2.5 ml of $HClO_4$ (per-chloric acid) (~65% w/w), and 5 ml of HF (hydrofluoric acid) (~49% w/w), on a hot plate in operating conditions of ~90°C temperature for a period of ~75 minutes. The solution was diluted up to 50 ml with distilled deionized water and stored at 4°C in prewashed polyethylene specimen tubes until the analysis. Four-point calibration with prepared standards was done for heavy metals, and coefficient of determination (R^2 as 0.99) was obtained for the calibration curves. A

constant calibration verification was performed for every tenth sample runs in the diagnostic sequence. Air sample extraction and chemical analysis of metal and ions were carried out as per the USEPA compendium methods. The minimum detection limit of the AAS (model: SpectrAA 55) instrument for Iron (Fe), Manganese (Mn), Zinc (Zn), Copper (Cu), Chromium (Cr), Lead (Pb), and Aluminium (Al) is 0.06, 0.02, 0.01, 0.03, 0.06, 0.10, 0.03 mg L^{-1}. Metal recovery efficiencies were determined by spiking the known quantity of metal mass on the filter paper and extracting and analyzing it, as per the developed standard operating procedures on AAS. The recoveries for the metals were in the range of 85-98%. The precision and accuracy of the instrument were within 4% and in the range of 2-15% for the analyzed metals, respectively.

3.2.4 Measurement of meteorological parameters

Besides source conditions and characteristics, local meteorology plays a significant role in the dispersion of air pollutants. A wireless weather station was installed to record the local meteorological conditions (Model: Vantage Pro, California, USA) installed (∼2 km to the west-north-west) on the roof top of Air & Noise Pollution (ANP) Laboratory (∼12 m above the ground level) on the campus of the Indian Institute of Technology (IIT) Guwahati (26.1878°N, 91.6916°E, Elevation: 56 m [m.s.l.]) (Fig. 3.4). The data was recorded at five-minute interval. A data logger was used to back up the monitored meteorological data. The meteorological parameters includes atmospheric temperature (°C), wind speed (m s^{-1}), rainfall (mm), relative humidity (%), barometric pressure (mbar), wind direction (°), and surface-reaching solar radiation (W m^{-2}). It is capable of measuring the pre-tested values of meteorological parameters with maximum accuracy: Atmospheric Temperature (0.1°C precision ± 0.5°C), Relative Humidity (1% RH precision ± 3% RH), Rainfall (214 cm^2 collector with 0.2 mm bucket), Wind Speed (0.4 ms^{-1} steps ± 5%), Wind Direction (16-point compass), Barometric Pressure (internal console ± 1.0 mbar), and surface reaching Solar Radiation (detects SR at wavelengths of 300 to 1100 nm ± 5%). It can transfer the recorded data to the console unit placed up to 300 m distance (Jenkins, 2014). In this study, the sunshine hours were taken as 7 per day (09:00-16:00 LST). The measurements of meteorological parameters were carried out from Jan to June 2020, covering the Indian winter and pre-monsoon seasons.

Fig. 3.4 Wireless weather station (Vantage pro2, USA) installed at the Air Pollution Laboratory, IIT Guwahati rooftop.

3.2.5 Traffic volume study

To determine the various traffic characteristics, video cameras were installed at two locations- parking lot area (L1) in the Kamakhya hilltop (26.16473°N, 91.707038°E, 225 m [a.s.l.]), Assam Trunk road (L2) in the foothills of the valley (26.159981°N, 91.70603°E, 66.83 m [a.s.l.]). The L1 is ~225 degrees to the north of the monitoring station. Fig. 3.5 shows the geographical location of the traffic monitoring locations. The traffic data was recorded from 07:00 to 20:00 LST each day (referred to as daily in this study). After that, the videotapes were manually analyzed to determine the traffic characteristics such as hourly traffic volume, traffic speed, traffic flow rate, and traffic composition.

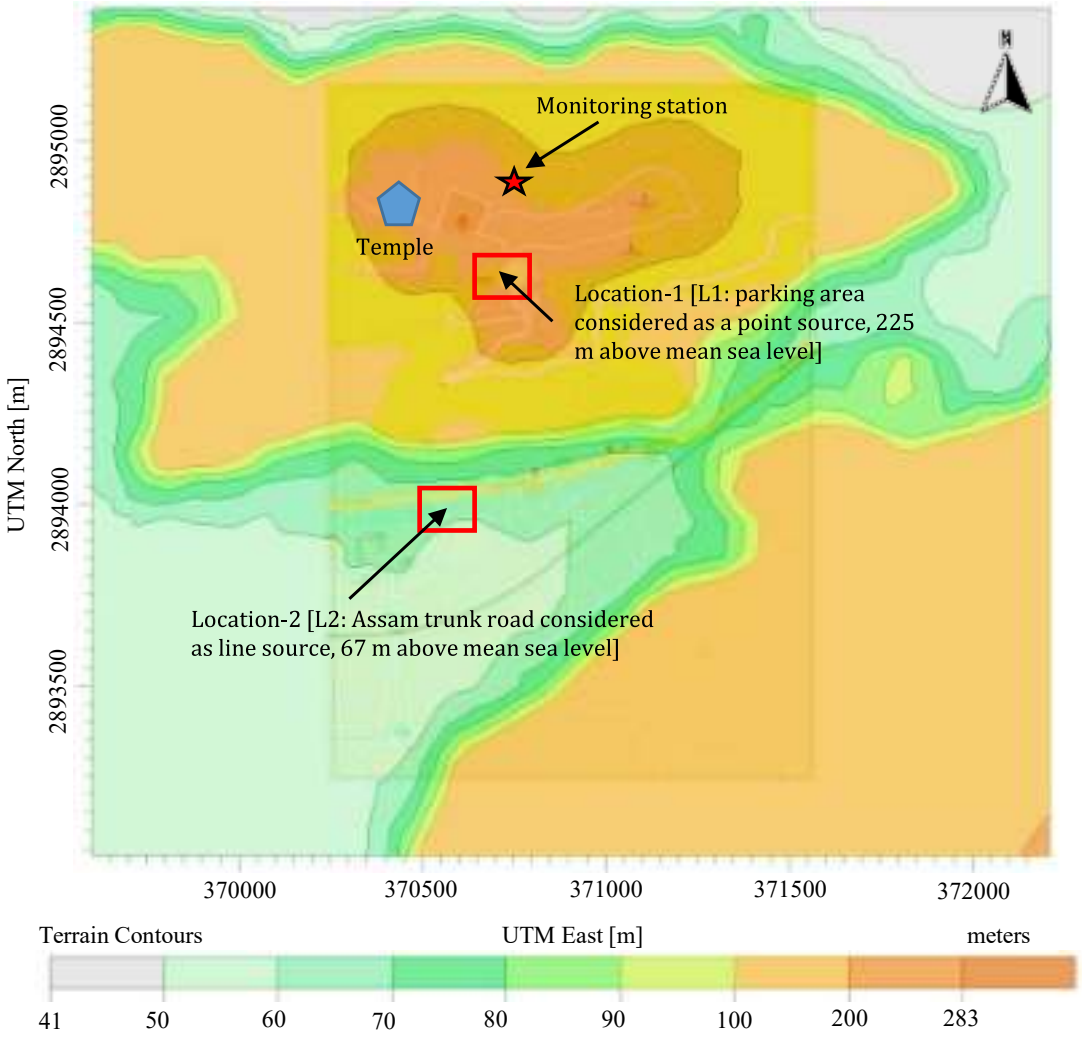

Fig. 3.5 The details of two traffic monitoring locations in the Brahmaputra River valley, Northeast India.

As per the Automotive Research Association of India (ARAI, 2008, 2017), the traffic composition was classified into five different categories termed as two-wheelers (2W: motorcycles, mopeds, and scooters), three-wheelers (3W: Auto-rickshaws), four-wheelers (4W: passenger cars), light transport vehicles and mini passenger carriers (LDDV), and buses and heavy trucks (HDDV).

3.3 Estimation of Wavelength-dependent light absorption coefficient

The AE-33 model was used to assess the sources like biomass (BB) and fossil fuel (FF) burning originated BC in the ambient BC concentrations (Sandradewi et al., 2008). This method assumes that the optical absorption of BC at a particular wavelength ($b_{abs\_BC\_\lambda}$) is a sum contributes of biomass and fossil fuel burning, and the equivalent absorption coefficient follows λ^{-1} and λ^{-2} spectral dependences, respectively. The light absorption by carbonaceous constituents includes BC, primary Brown Carbon (B_rC_{pri}), and secondary Brown Carbon (B_rC_{sec}) . The Aethalometer provides the estimates of BC concentrations at seven wavelengths (λ) of 950, 880, 660, 590, 520, 470, 370 nm using associated aerosol absorption coefficient (b_{abs}) and default mass absorption cross-section (MAC) values of 7.19, 7.77, 10.35, 11.58, 13.14, 14.54, and 18.47 m^2g^{-1}, respectively at each wavelength. The aerosol light absorption coefficient (b_{abs}) at a specific wavelength (λ) is calculated by equation 3.1.

$$b_{abs}(\lambda) = BC(\lambda) \cdot MAC(\lambda) \tag{3.1}$$

3.4 Source apportionment of Black Carbon using improved light-absorption method

The AE-33 provides estimates of the biomass burning percentage (BB%) utilizing an approach with default Angstrom Absorption Exponent (AAE) values of 1.0 for fossil fuel (AAE_{FF}) and 2.0 for biomass burning (AAE_{BB}). However, since AAE varies with the site characteristics, default AAE_{FF} and AAE_{BB} values in the AE-33 model lead to incorrect estimates of BC associated with fossil fuel (BC_{FF}) and biomass burning (BC_{BB}) (Dumka et al., 2018). Hence, the AAE values were calculated from the derived $b_{abs}(\lambda)$ at the spectral band of 370-880 nm by equation 3.2.

$$AAE = \frac{\ln\left(b_{abs\_370\ nm}/b_{abs\_880\ nm}\right)}{\ln\left(370/880\right)} \tag{3.2}$$

The values, which lie at the side of the calculated $AAE_{370\text{-}880}$ series, were obtained as $AAE_{FF} = 1.0$ and $AAE_{BB} = 1.7$ (Fig. A.1a). The BC, BC_{FF}, and BC_{BB} were estimated by the

AE-33 model using the equations from 3 to 9 (Sandradewi et al., 2008). The AE-33 model adopts that BC is originated only from BB and FF combustion sources, which can be written as given by equation 3.3.

$$BC = BC_{FF} + BC_{BB} \tag{3.3}$$

The spectral b_{abs} for the pair of the wavelength (370, 880 nm) is divided as given by equations 3.4-3.5:

$$b_{abs}(370\ nm) = b_{abs\_FF}(370\ nm) + b_{abs\_BB}(370\ nm) \tag{3.4}$$

$$b_{abs}(880\ nm) = b_{abs\_FF}(880\ nm) + b_{abs\_BB}(880\ nm) \tag{3.5}$$

The right-side unknown terms of equations 3.4 and 3.5 need to be calculated for approximating the light elimination employing FF and BB at 370 and 880 nm. Equations 6-7 relate to the wavelengths (370, 880 nm) and b_{abs} for FF and BB. The values of AAE_{FF} as 1.0 and AAE_{BB} as 1.7 were primarily used in equations 3.6 and 3.7.

$$\frac{b_{abs\_FF}(370\ nm)}{b_{abs\_FF}(880\ nm)} = \left(\frac{370}{880}\right)^{-AAE_{FF}} \tag{3.6}$$

$$\frac{b_{abs\_BB}(370\ nm)}{b_{abs\_BB}(880\ nm)} = \left(\frac{370}{880}\right)^{-AAE_{BB}} \tag{3.7}$$

By solving equations 3.4-3.7, the BC_{FF} and BC_{BB} at 880 nm were obtained, given by equations 3.8 and 3.9.

$$BC_{FF}(880\ nm) = \frac{b_{abs\_FF}(880\ nm)}{MAC(880\ nm)} \tag{3.8}$$

$$BC_{BB}(880\ nm) = \frac{b_{abs\_BB}(880\ nm)}{MAC(880\ nm)} \tag{3.9}$$

3.5 Estimation of Brown Carbon

The assumption for estimating the Brown Carbon (B_rC) absorption ($b_{abs\_B_rC}$) is that BC is the lone absorber at higher wavelengths (950 and 880 nm). The value of AAE_{BC} is taken as 1. Hence, the whole b_{abs} was separated into $b_{abs\_B_rC}$ and b_{abs_BC} contributions in the spectral range of 370-660 nm, using equation 3.10 (Qin et al., 2018).

$$b_{abs}(\lambda) = b_{abs\_BC}(\lambda) + b_{abs\_B_rC}(\lambda) \tag{3.10}$$

Then, the b_{abs_BC} was concluded from 880 nm to the smaller wavelengths (370-660 nm) by AAE_{BC} as 1.0 in equation 3.11, and $b_{abs\_B_rC}(\lambda)$ was estimated by equation 3.10.

$$b_{abs\_BC}(\lambda) = b_{abs}(880\ \text{nm}) \cdot \left(\frac{\lambda}{880}\right)^{-AAE_{BC}} \tag{3.11}$$

3.6 Estimation of secondary Brown Carbon

The $b_{abs}(\lambda)$ is due to other carbonaceous aerosols from primary and secondary sources (Wang et al., 2019). BC is assumed to be radiated from simply primary sources. Hence, the absorption of secondary B_rC in $b_{abs}(\lambda)$ ($b_{abs\_B_rC\_sec}(\lambda)$) was calculated by equation 3.12.

$$b_{abs\_B_rC\_sec}(\lambda) = b_{abs}(\lambda) - b_{abs\_pri}(\lambda) \tag{3.12}$$

where, $b_{abs\_pri}(\lambda)$ indicates the light absorbed by mutually primary non-combustion and combustion sources. The light absorption of primary non-combustion ($b_{abs\_pri\_non\text{-}com}$) sources is negligible even in heavily stagnated natural background sites (Teich et al., 2017); hence it was neglected. Equation 3.13 can be written from the BC tracer technique.

$$b_{abs\_pri\_comb}(\lambda) = \left(\frac{b_{abs}(\lambda)}{BC}\right)_{pri} \cdot [BC] \tag{3.13}$$

The $(b_{abs}(\lambda)/BC)_{pri}$ ratios were calculated by minimum R^2 method (shown in Fig. A.1b), in which a series of arbitrary values were chosen inside the range of estimated $b_{abs}(\lambda)/BC$ ratios at a particular wavelength (Wang et al., 2019).

3.7 Health risk analysis

The health risks of BC's exposure for the residents of the study region were estimated in equal amounts of passively smoked cigarette (PSC) (Van der Zee et al., 2016). The number of passively smoked cigarette (N_{PSC}) equal to 1 $\mu g\ m^{-3}$ increase in BC concentration intended for a particular health consequence was calculated by equation 3.14.

$$N_{PSC} = \frac{\left(\frac{\ln (RR_{BC})}{\Delta_{Concentration}}\right)}{\left(\frac{\ln (RR_{ETS})}{\text{assumed number of PSC}}\right)} \cdot \Delta BC \tag{3.14}$$

where, $\left(\frac{\ln (RR_{BC})}{\Delta_{Concentration}}\right)$ denotes a resultant risk for change in $\Delta_{Concentration}$ of BC, $\left(\frac{\ln (RR_{ETS})}{\text{assumed number of PSC}}\right)$ shows the risk of environmental tobacco smoke (ETS) exposure for the total passively smoked cigarette per day, RR denotes the likelihood of evolving a disease persuaded by the exposure to atmospheric pollutants, RR_{BC} & RR_{ETS} denote the relative risk (RR) of aerosol BC and ETS exposure for the particular health outcomes (Table 3.2 and Table 3.3) and ΔBC denotes the change between BC's estimated and background mass concentration. This assessment followed the hypothesis of (Van der Zee et al., 2016), in which as per the (Global Adults Tobacco Survey, 2019) (http://gatsatlas.org/), estimates daily consumption of 14 cigarettes was assumed equivalent to tobacco consumption in Guwahati, Assam India. It was anticipated that the everyday exposure of people is equal to the daily mean concentration of BC. The health risk estimates for air pollutants and ETS exposure are estimated with standard error (SE). The background concentration of BC was taken as per the 1.25th percentile from the entire dataset (Rupakheti et al., 2017; Pani et al., 2020), i.e., $\sim 4\ \mu g\ m^{-3}$.

Similarly, the health risks of $PM_{2.5}$ were estimated in terms of the number of PSC to 10 $\mu g\ m^{-3}$ increase in $PM_{2.5}$ concentration. Furthermore, the combined health risks of BC and $PM_{2.5}$ were also estimated for four different health outcomes.

Table 3.2 Risk estimates for ETS exposure (compared to no ETS exposure) concerning health outcomes (Van der Zee et al., 2016).

Outcome	Description	Risk estimate (95% CI)	Exposure	References
Lung cancer (LC)	Incidence (> 15yrs)	1.21 (1.13-1.30)	At home; in non-smokers	Surgeon General Report, 2006
Cardiovascular mortality (CM)	Ischemic heart disease (IHD) mortality > 15 yrs	1.27 (1.19-1.36)	At home or at work; in non-smokers	Surgeon General Report, 2006; Öberg et al., 2010
Percentage lung function decrement in school aged children (PLFD)	Percentage reduction in Forced Expiratory Volume in 1s (FEV1)	1.4% (1.0-1.9%)	Either parent	Cook et al., 1998
Low birth weight (LBW)	Prevalence of LBW < 2500g at term	1.38 (1.13-1.69)	Any exposure at work or at home; in non-smoking mothers	Windham et al., 1999

Table 3.3 Risk estimates (95% CI) for equivalent Black Carbon concentration and the established health outcomes (Van der Zee et al., 2016).

Outcome	$PM_{2.5}$ (per 10 $\mu g\ m^{-3}$)	EBC (per 1 $\mu g\ m^{-3}$)	References
Lung cancer (LC)	1.09 (1.04-1.14)	1.05 (0.02-1.08)	Van der Zee et al., 2016
Cardiovascular mortality (CM)	1.20 (1.09-1.31)	1.13 (1.09-1.18)	Smith et al., 2009
Percentage lung function decrement in school-aged children (PLFD)	1.5% (–0.3-3.2%)	1.3% (0.3-2.2%)	Van der Zee et al., 2016
Low birth weight (LBW)	1.19 (1.00-1.42)	1.16 (0.93-1.44)	Van der Zee et al., 2016

3.8 Dispersion modelling of traffic-derived Black Carbon emissions

3.8.1 AERMOD air quality model

AERMOD is an advanced steady-state Gaussian plume model developed by USEPA as a modified version of Industrial Source Complex (ISCST3) (USEPA, 2012). The basic assumption is that the pollutants originated from the plume disperses in vertical and horizontal directions following the Gaussian or normal distribution, while traveling in the down wind direction. The extent of dispersion depends on the wind speed, wind direction, and turbulence in the lateral and vertical movements, characterized by their probability density function. It can model multiple sources (for example, point, line, area, volume, etc.) in flat and complex terrain. AERMOD model calculates the pollutant concentration by summing up the contributions from the direct source, indirect source, and penetrated source (Weil et al., 1997). It can be written as given by equation 3.15.

$$C_T\{x, y, z\} = C_d\{x, y, z\} + C_i\{x, y, z\} + C_p\{x, y, z\} \tag{3.15}$$

where, C_T denotes the total concentration, C_d denotes the direct source concentration, C_i denotes the indirect source concentration, and C_p denotes the penetrated source concentration. x, y, and z denote the receptor distance in the x, y, and z direction.

The direct source describes the dispersion of plume material that reaches the ground directly from the source via downdrafts. It is calculated as given by equation 3.16 (Weil et al., 1997).

$$C_d\{x,y,z\} = \frac{Qf_p}{2\pi u\sigma_y\sigma_z} \cdot exp\left(\frac{-y^2}{2\sigma_y^2}\right)\left[exp\left(-\frac{Z-\varphi_{dj}+2Z_i{}^2}{2\sigma_z^2}\right) + exp\left(-\frac{Z+\varphi_{dj}-2Z_i{}^2}{2\sigma_z^2}\right)\right] \tag{3.16}$$

where, Q denotes the source emission rate (g s^{-1}), f_p denotes a fraction of the source material that remains trapped in CBL, u denotes the wind velocity (m s^{-1}), σ_y & σ_z denote the dispersion of coefficients in the y and z direction (m), φ_{dj} denote the the height of the direct source (m), Z_i denotes the the height of CBL (m), and Z denotes the height of receptor (m), respectively. The height of the direct source is calculated as: $\varphi_{dj} = h_s+\Delta h+wx/u$ where, h_s, Δh, w, x, u denote the height of the stack (m), plume rise (m), updraft velocity (m),

downwind distance (m) and wind velocity (m/s), respectively.

The indirect source is included to treat the first interaction of the updraft plume with the elevated inversion. It means that the plume that initially rise to the top of convective boundary layer in updrafts return to the ground via downdrafts. It is calculated as given by equation 3.17 (Weil et al., 1997).

$$C_i\{x,y,z\} = \frac{Qf_p}{2\pi u\sigma_y\sigma_z}\cdot exp\left(\frac{-y^2}{2\sigma_y^2}\right)\left[exp\left(-\frac{Z-\varphi_{dj}+2Z_i^{\,2}}{2\sigma_z^2}\right)+exp\left(-\frac{Z+\varphi_{rj}-2Z_i^{\,2}}{2\sigma_z^2}\right)\right] \quad (3.17)$$

where, $\varphi_{rj} = h_s + wx/u$ is the height of indirect source (m). It can also be written as $\varphi_{rj} = \varphi_{dj} - \Delta h$.

The penetrated source is included to account for material that initially penetrates the elevated inversion but subsequently can re-enter the convective boundary layer via turbulent mixing of the plume. It is simple Gaussian form for both vertical and horizontal plume distributions. It is calculated as given by equation 3.18 (Weil et al., 1997).

$$C_p\{x,y,z\} = \frac{Q(1-f_p)}{2\pi u\sigma_y\sigma_z}\cdot exp\left(\frac{-y^2}{2\sigma_y^2}\right)\left[exp\left(-\frac{Z-h_{ep}+2Z_i^{\,2}}{2\sigma_z^2}\right)+exp\left(-\frac{Z+h_{ep}+2Z_i^{\,2}}{2\sigma_z^2}\right)\right] \quad (3.18)$$

where, the penetrated plume height (h_{ep}) is the height of the plume centroid above the mixed layer. It can be calculated as $h_{ep}=(h_s+z_i)/2 + 0.75\Delta h$.

The pollution concentration contributed by all three sources are substituted in equation (3.15) to get the total concentration at the particular receptor.

3.8.2 Structure for AERMOD model

The presence of obstacles (e.g., slight to steep slopes and building heights) significantly influences the meteorological conditions (e.g., wind field, fog occurrence) and dispersion pattern of air pollutants (Hnová et al., 2021). Hence, three primary data inputs were prepared to run the AERMOD model: vehicular emission rate, atmospheric data (temperature, wind speed, cloud cover, wind direction, relative humidity, mixing height, precipitation, pressure), and topography data (altitude, hills and valleys elevation). The AERMOD modelling system has two modules: AERMET to process the meteorology to produce the meteorological data

contours for both observed and WRF processed met data, and AERMAP to process the terrain data to create the topography data contours for identified receptors (USEPA, 2012). Composed with vehicular emission rates, the outputs of these two modules were incorporated into the third section, AERMOD- to produce BC concentration contours at the receptors in the modelling domain for the specified interval. Fig. 3.6 shows the process flow chart for this study.

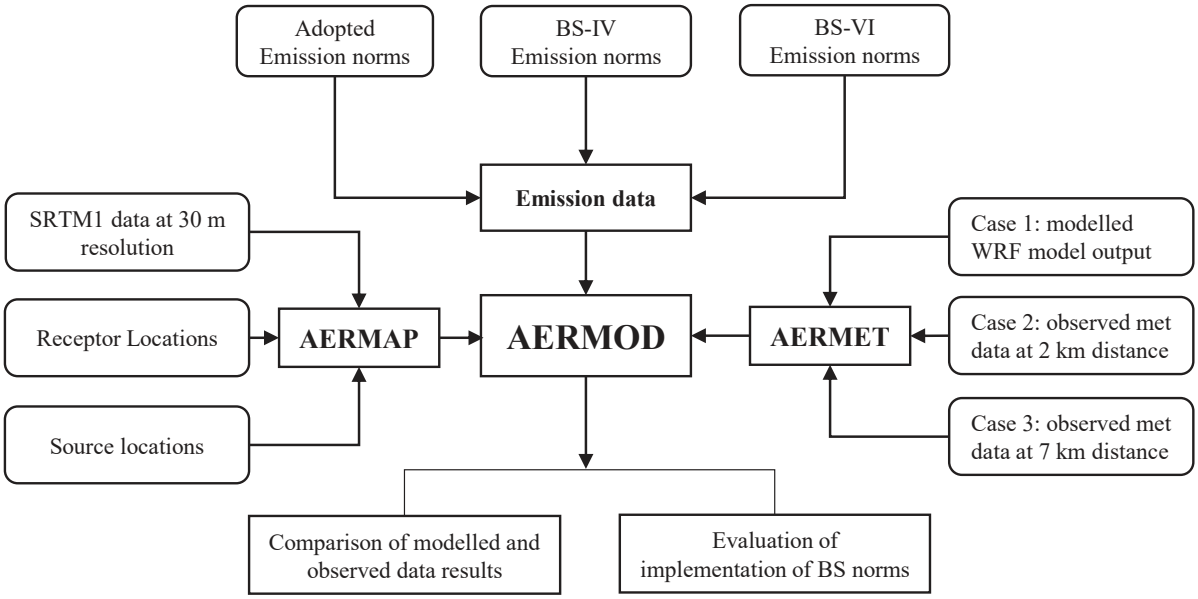

Fig. 3.6 Schematic methodology for the AERMOD study.

3.8.2.1 Emission source data

The road traffic at L1 (Fig. 3.5) was considered congested since the vehicles were stopped at the parking lot area. The road traffic at L2 was deemed to be free-flowing to account for a variable emission since, during congestion, emission may be constant. L1 and L2 were treated as area and line source types, respectively. The background concentration of BC_{FF} was obtained as the 1.25^{th} percentile of the estimated BC_{FF} concentration from the whole dataset (Kondo et al., 2006), i.e., $\sim 3\ \mu g\ m^{-3}$. This concentration is used as a boundary concentration in AERMOD calculations of the contribution from local sources.

3.8.2.2 Meteorological data

Two sets of weather data were used as an input to the AERMOD model in this study- data from a Weather Station (observed met data) and Weather Research Forecasting model (WRF)-produced meteorological data (modelled met data). It is assumed in the AERMOD

that concentrations at all distances during a modelled period are governed by the temporal-average meteorology of the period. The observed and the modelled meteorological data, including surface meteorological conditions and upper air sounding records, were used for the dispersion modelling. These data were processed in the AERMET that generated two meteorological data profiles for AERMOD modelling. In the observed meteorological data, cloud cover is needed by the weather-related preprocessor AERMET for generating the input records. Though, cloud cover is barely recorded in typical weather stations. However, surface-reaching solar radiation (in W m^{-2}) data was available from the weather station. Hence, we used equation 3.19 to derive the cloud cover data (Kasten and Czeplak, 1980; Kim and Hofmann, 2005).

$$SR = SR_o(1 - 0.75\ c^{3.4}) \tag{3.19}$$

where, SR and SR_o represent the solar radiation separately under cloudy/actual/real-time and clear sky situations, respectively and c denotes the cloud cover (0 to 1). The peak value amongst the quantities in each month is presumed to signify solar radiation during clear sky situations. In contrast, the value at a specific hour on the day is presumed to denote the real-time solar radiation situations in the simulated period. The mixing heights were obtained at one hour from the HYSPLIT model through the turbulent kinetic energy outline technique (Draxler and Rolph, 2016; Dumka et al., 2018). The Upper air estimator tool of the AERMET view was used to estimate the upper-air parameters. The reason for using observed meteorological data was to compare the obtained results processed using WRF data, which may still provide valuable results. We have also used the meteorological data from the pollution control board (PCB) located at 7 km southeast-south.

3.8.2.3 Topography data

The topography may cause acceleration, deceleration, and refraction of wind arrangements to a significant level. Complex topography produces limited-scale movements of air pollutants (Hnová et al., 2021). The Shuttle Radar Topography Mission of one Arc-second (SRTM1) data at ~30 m resolution was used in the domains AERMAP module. Currently, SRTM is a complete elevation resolution digital topographic catalogue of Earth (Tartakovsky et al., 2016). Terrain elevations were in meters relative to the mean sea

level built on the WGS84 coordinate system, Zone 46R, which varied from 44 to 354 m in the specified domain. A buffer of 10 m was considered from the predefined extent of the modelling domain for proximity analysis. Additionally, the surface roughness, brown ratio, and net radiation were also included. The AERMAP was utilized to formulate the topography info built on the source locations, SRTM data, and receptor locations.

3.8.2.4 Receptor data

For receptor locations in the complex terrain, the modelling process employed a Cartesian receptor grid with 100 m receptor spacing, in addition to two discrete receptors. The Cartesian receptor grid varied as per modelling extent. The modelling extent was 1050 × 1350 m from SW coordinates (26.157508°N, 91.701921°E). The 154 receptors excluding L1 and L2 locations were defined in the modelling domain, each with a different height due to uneven terrain heights.

3.8.3 Emission rate

The emissions (in mg s^{-1}) were calculated by equation 3.20.

$$ER_w = \frac{\Sigma_{j=1}^{n} N_j \cdot EF(i,j) \cdot ATS}{N_{vehicles}} \tag{3.20}$$

where, ER_w denotes the weighted emission rate (mg s^{-1}), N_j denotes the number of vehicles of an individual category, EF (i,j) denotes the emission factor of pollutant i for j^{th} vehicle category, and $N_{vehicles}$ denotes the total number of vehicles, respectively. ATS denotes the average speed of the traffic fleet (km hr^{-1}). The average speed of the traffic fleet is considered as 20 km hr^{-1}, which is analyzed from the videotapes.

The adopted emission factors were obtained from Table 2.3 (Paliwal et al., 2016). ARAI (2017) proposed the new emission norms for $PM_{2.5}$ only. So, we calculated the BC emission rates for BS-IV and BS-VI emission norms from the share of fossil fuel-derived BC in $PM_{2.5}$. It was 11% (ranged from 6-20%) during the study period. 2W and 4W vehicles were considered gasoline engines; hence the fraction is taken as 6%. Similarly, 3W, LDDV, and HDDV vehicles were considered diesel engines; the fraction is taken as 20%. So based on these assumptions, BS-IV and BS-VI emission rates were calculated and listed in Table 3.4.

Table 3.4 Emission rates of BC_{FF} from the adopted emission factor (Paliwal et al., 2016), BS-IV and BS-VI emission norms (ARAI, 2017).

Vehicles type	Emission factor (g km^{-1})			Emission rate (mg s^{-1})		
	BC_{FF} (Adopted)	$PM_{2.5}$(BS-IV)	$PM_{2.5}$(BS-VI)	BC_{FF} (Adopted)	BC_{FF}(BS-IV)	BC_{FF}(BS-VI)
2W	0.02	–	0.0045	0.1111	0.1111	0.0015
3W	0.15	0.0425	0.025	0.8333	0.0472	0.0277
4W	0.09	0.025	0.005	0.5000	0.0083	0.0015
LDDV	0.17	0.06	0.012	0.9444	0.0667	0.0133
HDDV	0.415	0.02	0.01	2.3055	0.0222	0.0111

3.8.4 Modelling conditions

To determine the best modelling predictions for the study domain, few conditions were used to conduct the modelling studies. The conditions are:

1. Prediction of BC_{FF} concentrations at location L1 and L2 using the background concentration as a boundary condition.
2. Prediction of BC_{FF} concentrations using daytime (07:00 to 20:00 LST) emission rate.
3. Prediction of BC_{FF} concentrations in hilly terrain, only to reveal the obstruction in BC dispersion that could occur due to uneven terrain.

For AERMOD modelling under these conditions, a traffic volume study was conducted at two unlike locations, L1 and L2. Due to the unavailability of data at nighttime, the model prediction was performed for the specified time.

3.8.5 Application of AERMOD

The model was also applied to BC pollution reduction due to the implementation of Bharat Stage (BS) emission norms i.e., BS-IV (equivalent to Euro 4) and BS-VI (equivalent to Euro 6) in India. These emission norms were implemented in 2017 (BS-IV) and 2020 (BS-VI) to reduce emissions from vehicles fitted with direct gasoline injection and compression ignition or diesel engines. It is important to note that BS-VI norms apply to all categories of vehicles all over India since April, 2020. At the same time, a significant fraction of the traffic fleet comprises the vehicles of BS-II, BS-III, and BS-IV vehicles. Many autos in the city have two-stroke engines. The results of new emission norms are not yet realized as the penetration of BS-VI vehicles is in a negligible fraction.

3.8.6 Performance evaluation

Due to the effect of arbitrary atmospheric developments, there may not be any flawless model in air quality modelling (Chang and Hanna, 2004). The model operational efficiency can be evaluated by relating the modelled and observed concentrations of the pollutants using appropriate statistical measures as listed in Table 3.5.

Table 3.5 List of statistical measures for testing air quality models' performance (Willmott, 1982; Chang and Hanna, 2004).

Formula	Description of the parameter	Acceptable range
$FB = \frac{1}{0.5} \times \frac{(\overline{C_o} - \overline{C_p})}{(\overline{C_o} + \overline{C_p})}$	FB is the fractional bias, measures relative bias, and indicates only systematic errors, varies from –2 to +2 with the desired value of 0. –2 represents extreme under prediction and +2 extreme over prediction	–0.5 to 0.5
$NMSE = \frac{\overline{(C_o - C_p)^2}}{\overline{(C_o C_p)}}$	NMSE is the normalized mean square error, measures relative scatter, and reflects systematic and unsystematic (random) errors. NMSE ranges from 0 to ∞, where 0 represents perfect agreement.	<= 0.05
$GMB = \exp(\overline{lnC_o} - \overline{lnC_o})$	GMB is the geometric mean bias, measures relative bias, and indicate only systematic errors desired value 0.	0.75 to 1.25
$GV = \exp[\overline{(lnC_o - lnC_p)^2}]$	GV is the geometric variance, desired value 0.	1 to 1.25
$R = \frac{\overline{(C_o - \overline{C_o})(C_p - \overline{C_p})}}{(\sigma_{C_o} \sigma_{C_p})}$	R is the correlation coefficient. Ranges from 1 to –1, where 1 and –1 represent perfect correlation, and 0 indicates no correlation.	–1 to 1
$FAC2 = \frac{C_p}{C_o}$	FAC2 is the factor of two, and the desired value is 0.	0.5 to 2.0
$d = 1 - \frac{\Sigma_{i=1}^{n} (C_{o_i} - C_{p_i})^2}{\Sigma_{i=1}^{n} \left[\lvert C_{p_i} - \overline{C_o} \rvert + \lvert C_{o_i} - \overline{C_o} \rvert \right]^2}$	d is the index of agreement, measures the degree of model prediction, varies from 0 and 1. It determines the magnitude of agreement between observed and modelled values considering the sensitivity of differences between the values.	0.4 to 1.0
$R^2_{CV} = \max\left(0, 1 - \frac{RMSE^2}{MSE_{observed}}\right)$	R^2_{CV} is the cross-validation of R^2.	
$RMSE = sqrt[\overline{(C_p - C_o)^2}]$	RMSE is the root mean square error. It gives information about the non-systematic component of the differences in measurements and always non-negative.	>=0
$MSE_{observed} = [\overline{(C_o - \overline{C_o})^2}]$	MSE is the mean squared error of observed values. It is always strictly positive and not zero.	

C_o and C_p are observed and modelled value, $\overline{C}$: mean value over the datasets, σ_{C_o} and σ_{C_p} : standard deviation over the observed and modelled datasets.

Hanna (1993, 1988) recommended the usage of numerical performance methods such as fractional bias (FB), geometric mean bias (GMB), geometric variance (GV), correlation coefficient (R), and the fraction of extrapolations within a factor of two observations (FAC2), normalized mean square error (NMSE), an index of the agreement for testing the performance of air quality models. The model was also quantitatively evaluated using specific multiple out of sample cross-validation and external validation methods (Willmott, 1982; Keller et al., 2015). Cross-validation was assessed using two measures termed root mean square error (RMSE) and cross-validation R^2 (R_{CV}^2) (Keller et al., 2015). For each period, BC concentrations were estimated at the monitoring site L1. The index of association, covariation, or correlation between observed and estimated concentrations measures the strength of model predictions. Standard statistical indicators are the Pearson product-moment correlation (r), the proportion of variance explained by estimated BC concentrations, and R. It is also common to find r or Rs statistical significance to corroborate the correlation coefficients interpretation (Willmott, 1982). Table 3.5 shows the statistical parameters applied to validate the model output.

4

Data Analysis and Interpretation

In this section, the data collected during the fieldwork have been analyzed for meaningful interpretation and discussed in detail. The process of data description and interpretation helps to transform the data into information.

4.1 Black Carbon concentrations

The hourly-averaged BC concentration for the winter season was found to be 10.02 ± 4.72 $\mu g\ m^{-3}$ with the highest of 30.48 $\mu g\ m^{-3}$ on most foggy days as shown in Fig. 4.1. In January, it was 11.83 ± 2.56 $\mu g\ m^{-3}$, in February, it was 10.58 ± 2.17 $\mu g\ m^{-3}$ and in March, it was 7.69 ± 1.61 $\mu g\ m^{-3}$. The BC concentration level ranked from high in January to low in March. During a few rain events, the sudden decrease in the BC concentration (up to 2.10 $\mu g\ m^{-3}$) was observed. However, daily-averaged BC concentrations were found to be higher during weekend (10.89 $\mu g\ m^{-3}$) than weekdays (9.72 $\mu g\ m^{-3}$) during the study period.

Table 4.1 summarizes ambient BC concentrations reported in Guwahati and other cities worldwide in previous studies. During winter, Barman and Gokhale (2019) analyzed BC in an urban and a rural sites and found the highest winter average BC concentration of 22.44 $\mu g\ m^{-3}$ and 20.58 $\mu g\ m^{-3}$, respectively. The increase of BC in winter might be attributed to vehicular activities, biomass burning for heating purposes, unfavorable meteorological conditions, and the region's topography. The average BC concentration in this study during winter 2020 was similar to that in Helsinki, Finland (10.4 ± 20.3 $\mu g\ m^{-3}$), lower than Delhi (24.4 ± 12.2 $\mu g\ m^{-3}$) and higher than Beijing, China (5.31 ± 6.26 $\mu g\ m^{-3}$). By contrast, developed and hilly cities like Los Angeles, USA (8.45 $\mu g\ m^{-3}$) and Chiang Mai, Thailand (2.7 ± 1.0 $\mu g\ m^{-3}$) exhibit lower BC concentrations than Guwahati.

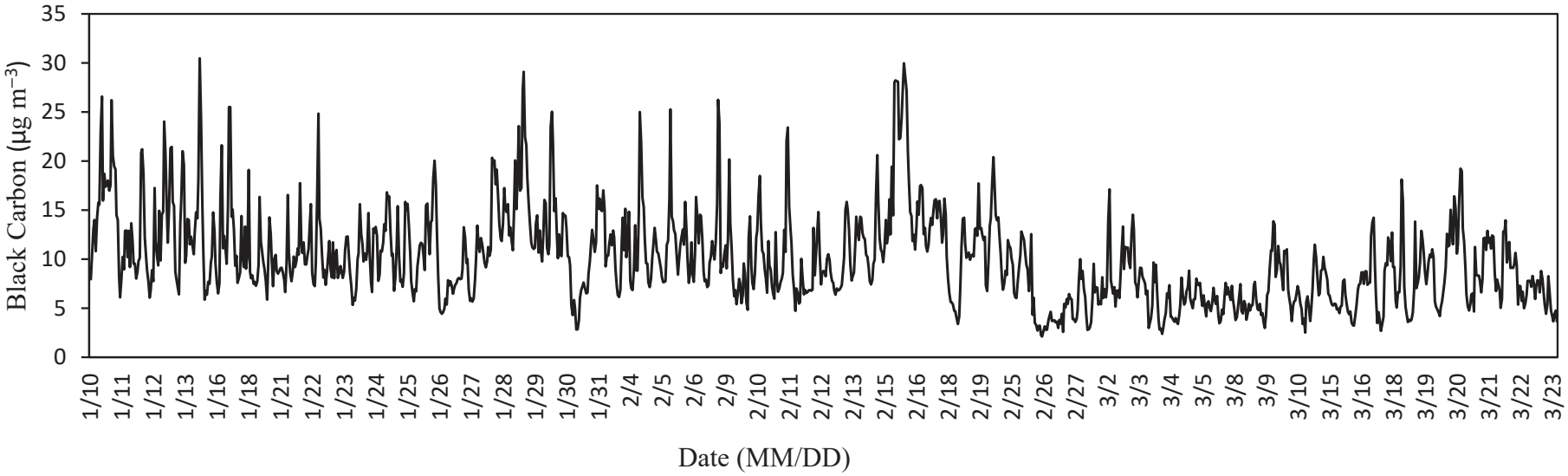

Fig. 4.1 Hourly time series of Black Carbon concentrations during the winter period.

Fig. 4.2 shows the winter diurnal variation of hourly-average BC concentration. It has been observed that the BC concentration peaked in the morning rush hours (08:30 to 10:30 LST). This may be caused by increased vehicular activity during these hours, lower mixing layer height, and extended fog in the valley. BC concentration was minimum during afternoon (02:30 to 3:30 LST). The thermal convection is high and atmospheric boundary layer is deep during these periods. This causes rapid dispersion of BC from surface level. The atmospheric boundary layer depth decreases when sunset happens and a nocturnal layer begins to form at closer ground level. This causes inversion and trapping of pollutants ultimately leading to build up of BC concentration. The low BC concentrations during midnight and early morning hours can be attributed to the low anthropogenic activities. The hourly-mean BC concentration was comparatively higher during winter daytime (10.16 ± 2.64 $\mu g\ m^{-3}$) than nighttime (9.86 ± 0.49 $\mu g\ m^{-3}$).

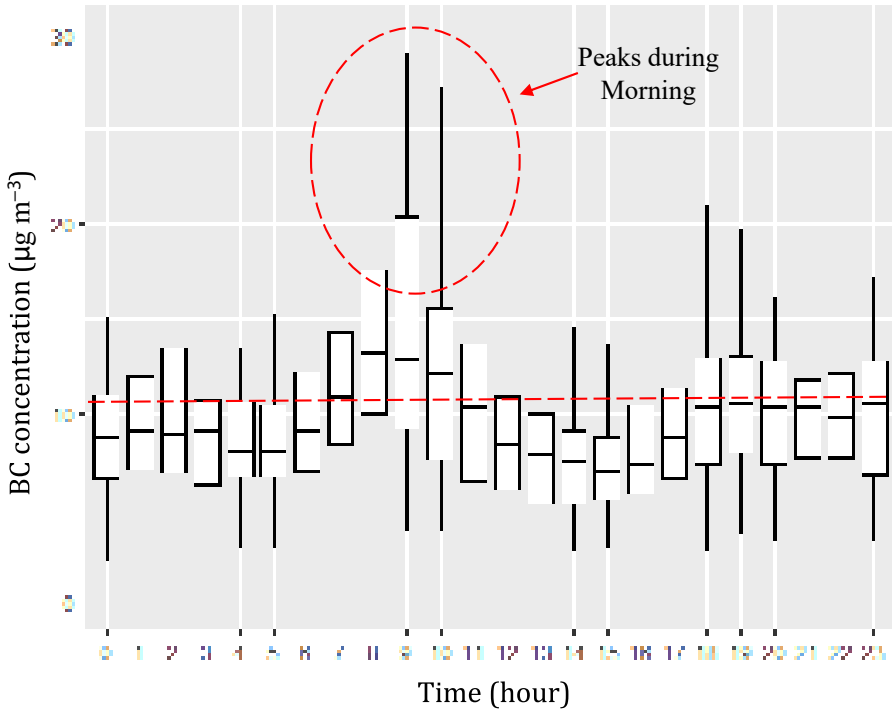

Fig. 4.2 Winter mean diurnal pattern of hourly-average Black Carbon concentrations.

Table 4.1 Comparison of Black Carbon (unit: $\mu g\ m^{-3}$) mass concentrations reported in different studies.

Measurement site	Site type	Period	Instrument	BC Mean value	References
Guwahati, India	Suburban-hilly	Jan to Mar 2020	Aethalometer AE-33	10 ± 4.72	This study
Guwahati, India	Urban	Dec 2011	Aethalometer AE-51	9-41	Chakrabarty et al. (2012)
Guwahati, India	Rural	Dec 2016 to Feb 2017	Aethalometer AE-33	20.58	Barman and Gokhale (2019)
Darjeeling, India	High altitude	Jan 2010 to Dec 2011 (winter)	Aethalometer AE-42	3.9 ± 2.2	Sarkar et al. (2015)
Delhi, India	Urban	Dec 2015 to Feb 2016	Aethalometer AE-33	24.4 ± 12.2	Dumka et al. (2018)
Delhi, India	Urban	Dec 2011 to Mar 2012	Aethalometer AE-31	12.1 ± 8.7	Tiwari et al. (2015)
Gorakhpur, India	Urban	Aug 2013 to Jul 2015 (winter)	Aethalometer AE-33	19 ± 14	Vaishya et al. (2017)
Ahmedabad, India	Urban	Dec 2016 to Feb 2017	Aethalometer AE-31	7.5	Rajesh and Ramachandran (2018)
Agartala, India	Rural	Jan 2011	Aethalometer AE-31	12.56	Kaur et al. (2020)
Vijaywada, India	Suburban	Jan to Dec 2016 (winter)	Aethalometer AE-31	4.68 ± 1.32	Prasad et al. (2018)
Dehradun, India	Urban	Dec 2019 to Feb 2020	Aethalometer AE-33	9.45 ± 2.65	Prabhu et al. (2020)
Hanle, India	Rural	Dec 2009 to Fe 2010	Aethalometer AE-31	0.07 ± 0.06	Babu et al. (2011)
Kadapa, India	Semi-arid, rural	Dec 2011 to Feb 2012	Aethalometer AE-42	2.87 ± 0.81	Begam et al. (2016)
Beijing, China	Urban	Dec 2015 to Feb 2016	Aethalometer AE-33	5.31 ± 6.26	Liu et al. (2018)
Athens, Greece	Suburban	Mar 2013 to Feb 2014 (winter)	Aethalometer AE-31	2.4 ± 1.0	Diapouli et al. (2017)
Granada, Spain	Urban	Nov 2014 to Feb 2015	Aethalometer AE-31, AE-33	2.3 ± 2.1	Titos et al. (2017)
Chiang Mai, Thailand	Urban	Mar to May 2016	Aethalometer AE-31	2.7 ± 1.0	Pani et al. (2020)
Ontario, Canada	Urban	Jun 2015 to May 2016 (winter)	Aethalometer AE-33	1.2	Healy et al. (2017)
Los Angeles, USA	Rural/agricultural	Mar 2016 to Feb 2017 (winter)	Aethalometer AE-33	8.45	Mousavi et al. (2018)
Helsinki, Finland	Suburban	Jan to May 2017	Aethalometer AE-33	10.4 ± 20.3	Helin et al. (2018)

4.1.1 Ambient Black Carbon, $PM_{2.5}$ and PM_{10} concentrations

The daily-average BC, $PM_{2.5}$, and PM_{10} mass concentrations during winter in the study region are plotted in Fig. 4.3. The real-time $PM_{2.5}$ (ranging from 37 to 153.28 $\mu g\ m^{-3}$) and PM_{10} (ranging from 56.43 to 215.73 $\mu g\ m^{-3}$) concentrations obtained from 51 each samples during winter are 79.67 ± 28.25 $\mu g\ m^{-3}$ and 118.99 ± 41.03 $\mu g\ m^{-3}$, respectively. The mean coarse mode fraction (PM_{10}–$PM_{2.5}$) was found to be 39.33 ± 20.94 (ranging from 10.24 to 97.61 $\mu g\ m^{-3}$), which corresponds to 33% of the PM_{10}, lesser to the fraction found in Guwahati (42% of PM_{10}) (Tiwari et al., 2017). Further, 71% and 60% of the days in winter exceed the daily standards specified by National Ambient Air Quality Standards, India (NAAQS-I) for $PM_{2.5}$ (60 $\mu g\ m^{-3}$) and PM_{10} (100 $\mu g\ m^{-3}$), respectively. The minimum and maximum $PM_{2.5}$ concentrations differ even five times, with the highest in January and the least in February. The low PM concentrations were observed in the month of March for a few days, which might be due to a few rain events washing out the atmospheric particles. The significant variations in the daily-average PM concentrations may be attributed to rain washouts, boundary layer dynamics, transient emission events, the mixed proportion of vehicles category (BS-II to BS-VI), and aerosols from long distances (Fig. 4.11).

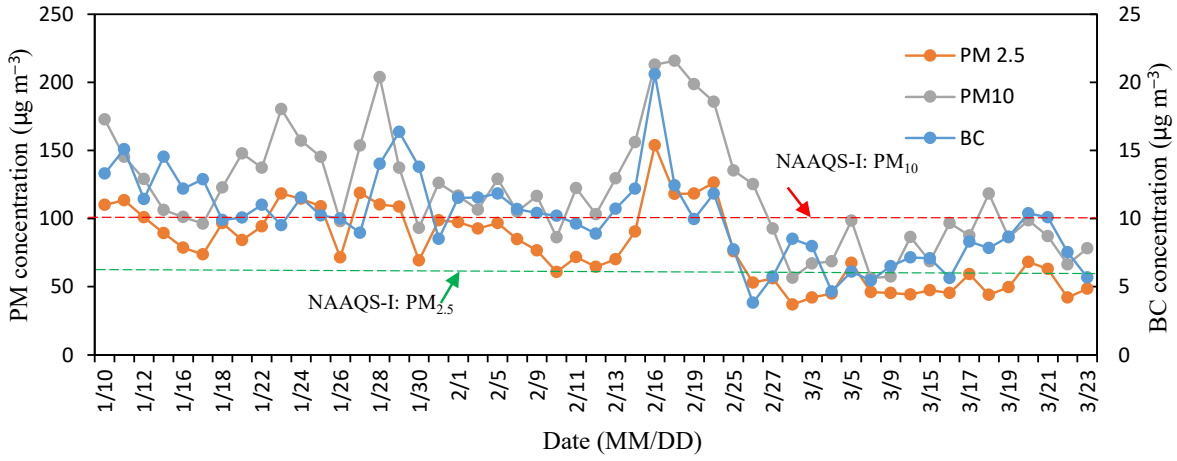

Fig. 4.3 Daily variations of $PM_{2.5}$, PM_{10}, and Black Carbon concentrations.

The large variation in PM and BC concentrations during winter period indicate that the natural cleansing mechanism (rain washouts) is effective over this region. Contrarily, low wind speed and hilly topography surrounded immediately by valley might have promoted the accumulation of airborne particles in this region. The mean $BC/PM_{2.5}$, BC/PM_{10} and $PM_{2.5}/PM_{10}$ was found to be 0.13 ± 0.03 (ranging from 0.07 to 0.23), 0.09 ± 0.03 (ranging from 0.03 to 0.15), and 0.67 ± 0.11 (ranging from 0.37 to 0.87), respectively. These ratios indicate a dominance of fine-mode particles. As per previous studies, the ratio of $BC/PM_{2.5}$ is generally higher in traffic source emissions than that from other sources (Liu et al., 2018; Zhang et al., 2013). The maximum $BC/PM_{2.5}$ appeared on 3 March 2020, which may be affected by various meteorological factors and pollution sources. On a monthly basis, the contributions of $PM_{2.5}$ to PM_{10} are the order of March (~50%), February (~63%), and January (~77%). Fig. 4.4 shows a correlation between the daily mean BC vs. $PM_{2.5}$ and $PM_{2.5}$ vs. PM_{10} concentrations. The high R^2 values of $PM_{2.5}$ vs. PM_{10} for the whole data set ($R^2 = 0.78$) indicate similarity in sources of PM pollution. At the same time, the poor correlation ($R^2 = 0.54$) of BC vs. $PM_{2.5}$ shows the possibility of different emission sources of both pollutants.

Table 4.2 also presents the results of $PM_{2.5}$ and PM_{10} concentration at Guwahati and cities around India. The concentrations were lower than the previously reported values at this region (Tiwari et al., 2017) and higher than Dibrugarh, which is located at the upper Brahmaputra river basin (Pathak et al., 2013). High $PM_{2.5}$ and PM_{10} concentrations were reported over the Indo Gangetic Plains [for example. New Delhi (Tiwari et al., 2013), Kanpur (Sharma and Maloo, 2005), Agra (Pipal et al., 2011)], which are comparable in magnitude with the current observed concentrations.

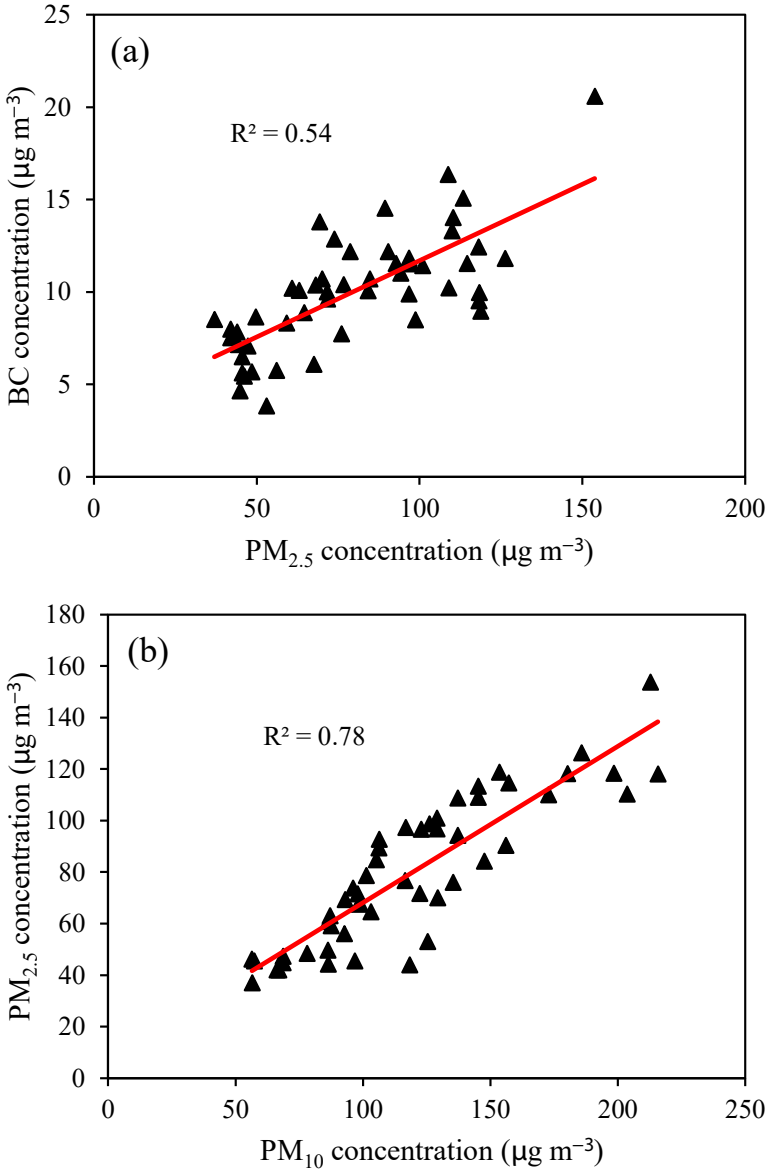

Fig. 4.4 The relationship of (a) Black Carbon vs. $PM_{2.5}$ and (b) $PM_{2.5}$ vs. PM_{10} concentrations during winter.

Table 4.2 Summary of $PM_{2.5}$ and PM_{10} concentrations during winter in India.

Location	Coordinates	Elevation*	Location type	$PM_{2.5}$ ($\mu g\ m^{-3}$)	PM_{10} ($\mu g\ m^{-3}$)	References
Guwahati	91.71°E, 26.16°N	225 m	Suburban-hilly	79.67 ± 28.25	118.99 ± 41.03	This study
Guwahati	91.66°E, 26.15°N	51 m	Urban	99.7 ± 43.2	156.6 ± 64.9	Tiwari et al. (2017)
Dibrugarh	94.6°E, 27.3°N	111 m	Urban	51.9 ± 32.4	57.2 ± 32.4	Pathak et al. (2013)
New Delhi	77.12°E, 28.35°N	296 m	Urban	80 to 900	150 to 1500	Tiwari et al. (2013)
Kanpur	80.28°E, 26.49°N	126 m	Urban	146	272.70 ± 64.64	Sharma and Maloo (2005)
Agra	78.02°E, 27.16°N	166 m	Urban	90.2 ± 7.2	278.7 ± 106.6	Pipal et al. (2011)
Agra	78.02°E, 27.16°N	166 m	Suburban	89.12 ± 37.94	234.54 ± 128.27	Pipal et al. (2011)
Hyderabad	78.4°E, 17.48°N	563 m	Urban	22-38	30-55	Latha and Badarinath (2005)
Mumbai	72.83°E, 18.96°N	4 m	Rural	64 ± 3.5	105 ± 4.5	Awasthi et al. (2011)
Udaipur	73.6°E, 24.5°N	733 m	Urban	59 ± 9.5	128.3 ± 11.5	Panicker et al. (2015)
Jabalpur	79.93°E, 23.16°N	396 m	Urban	68 ± 9.1	109.3 ± 10	Panicker et al. (2015)
Ahmedabad	72.55°E, 23.03°N	53 m	Urban	–	106	Ganguly et al. (2006)
Trivandrum	76.9°E, 8.55°N	39 m	Coastal	54.1	59.5	Pillai et al. (2002)
Kolkata	88.36°E, 22.56°N	7 m	Urban	179	304	Das et al. (2006)
Pune	73.85°E, 18.72°N	612 m	Urban	69	90	Kumar and Joseph (2006)
Anantapur	77.6°E, 14.71°N	335 m	Suburban	21.29	22.07	Balakrishnaiah et al. (2011)

* Above mean sea level

4.1.2 Chemical speciation of $PM_{2.5}$ and PM_{10}

The concentration of the ionic species and metals in $PM_{2.5}$ and PM_{10} are listed in Table 4.3. The ionic species are light scattering type aerosols, while BC is a strong absorber of solar light (Bond et al., 2013). The ratio between organic and inorganic species is commonly used in source identification and mixing processes in the atmosphere (Behera and Sharma, 2010). A multilinear regression analysis was performed between $PM_{2.5}$, BC, ionic species, and metals. The Spearman's correlation coefficients are summarized in Fig. 4.5. Statistically significant (95% confidence level) positive correlation coefficients were found among the BC, NO_3^-, F^-, Cl^- with $PM_{2.5}$, suggesting that all species, specifically NO_3^-, contribute significantly to $PM_{2.5}$. BC was highly correlated ($r = 0.88$) with $PM_{2.5}$, indicating similarity in the emission sources or reaction pathways. The weak sulfate and BC correlation (0.39) indicates a suburban environment. The highly significant positive correlation ($r > 0.70$) was observed between the groups Cl^--NO_3^- and F^--Cu in $PM_{2.5}$ at this region during winter. While, Al-SO_4^{2-}, Al-Cr, F^--Cr, BC-Mn, BC-Cr were negatively correlated. Similarly, multilinear regression analysis between PM_{10}, BC, ionic species, and metals was performed. The Spearmans correlation coefficients are summarized in Fig. 4.6, in which the warm color shows a negative correlation.

Table 4.3 Statistical description of the chemical constituents ($\mu g\ m^{-3}$) in the ambient $PM_{2.5}$ and PM_{10} collected during winter at BRV region.

Species	$PM_{2.5}$		PM_{10}		$PM_{2.5}/PM_{10}$
	Mean ± SD	Range	Mean ± SD	Range	
PM mass	79.67 ± 28.25	37-153	118.99 ± 41.03	56.43-215.73	0.67
Nitrate (NO_3^-)	5.91 ± 4.55	1.09-16.46	7.79 ± 5.57	1.93-21.49	0.75
Sulfate (SO_4^{2-})	0.57 ± 0.98	0.01-4.56	1.51 ± 0.77	0.73-3.42	0.37
Fluoride(F^-)	0.16 ± 0.05	0.08-0.28	0.20 ± 0.08	0.09-0.38	0.80
Chloride (Cl^-)	0.14 ± 0.07	0.04-0.31	0.19 ± 0.08	0.09-0.43	0.73
Iron (Fe)	2.30 ± 1.40	0.54-5.53	2.93 ± 2.05	0.34-6.50	0.78
Manganese (Mn)	1.36 ± 0.71	0.17-2.22	1.90 ± 0.58	0.43-2.63	0.77
Zinc (Zn)	1.97 ± 1.12	0.16-4.29	2.03 ± 1.14	0.05-4.00	0.97
Copper (Cu)	0.56 ± 0.38	0.05-1.68	0.96 ± 0.86	0.05-2.63	0.58
Chromium (Cr)	0.73 ± 0.30	0.07-1.18	0.87 ± 0.40	0.03-1.28	0.83
Lead (Pb)	0.95 ± 0.52	0.05-1.67	0.64 ± 0.49	0.10-1.86	1.48
Aluminium (Al)	0.78 ± 0.17	0.43-1.09	0.98 ± 0.59	0.10-2.26	0.79
$PM_{2.5}$: $NO_3^- > Fe > Zn > Mn > Pb > Al > Cr > SO_4^{2-} > Cu > F^- > Cl^-$					
PM_{10} : $NO_3^- > Fe > Zn > Mn > SO_4^{2-} > Cu > Al > Cr > Pb > F^- > Cl^-$					

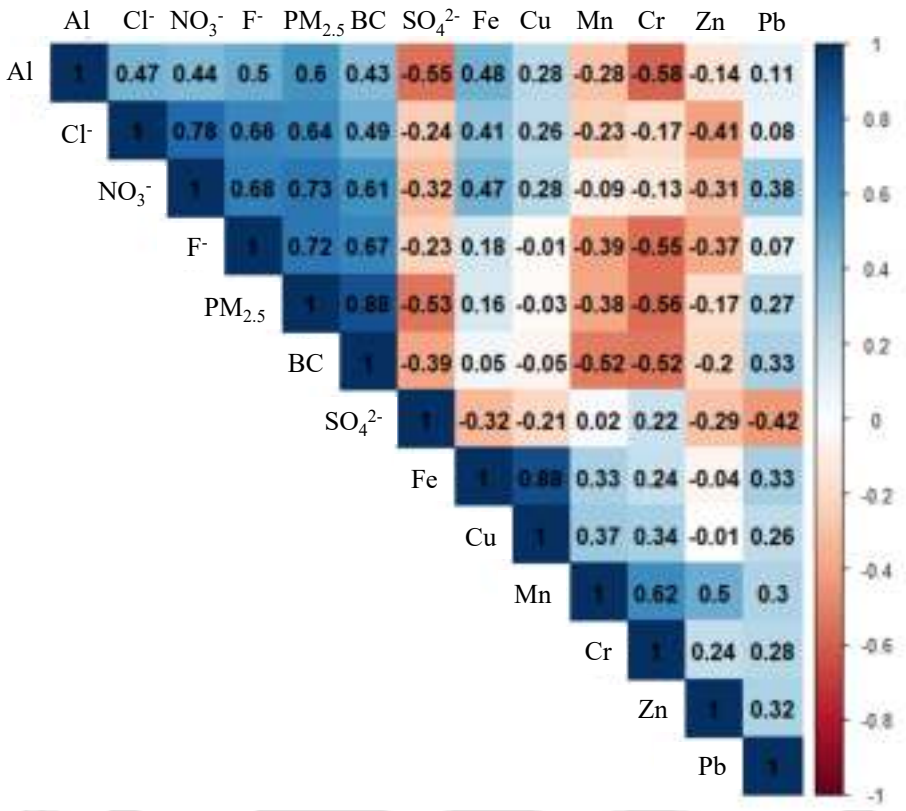

Fig. 4.5 Spearman's correlation coefficient between $PM_{2.5}$, Black Carbon, ionic species, and metals during winter.

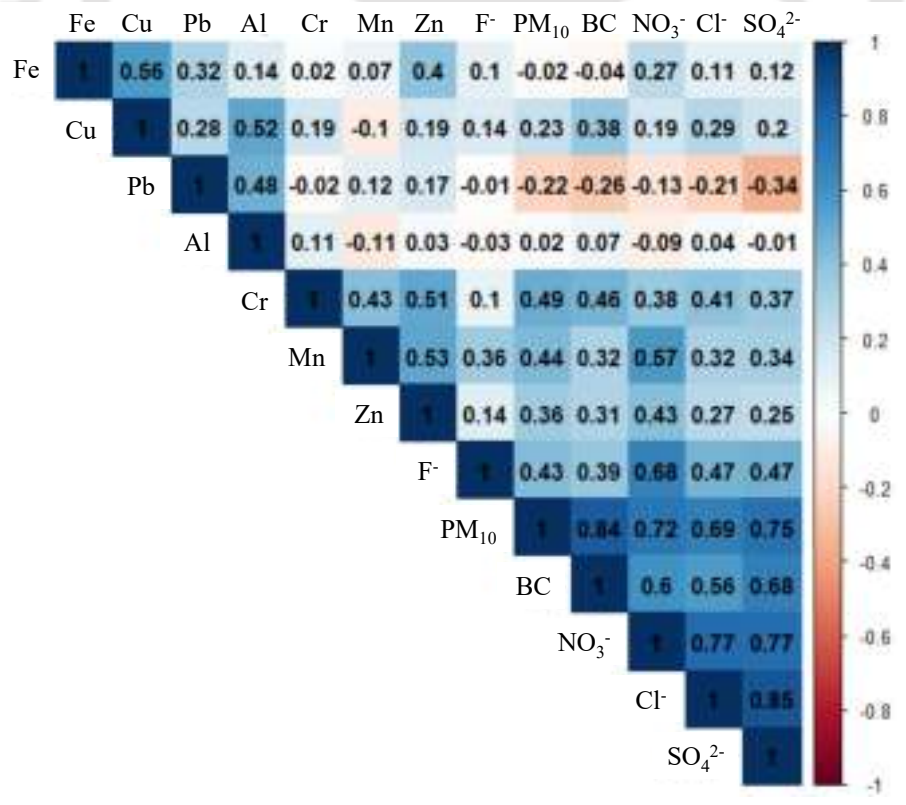

Fig. 4.6 Spearman's correlation coefficient between PM_{10}, Black Carbon, ionic species, and metals during winter.

4.1.3 Black Carbon and meteorological parameters

Fig. 4.7 shows the hourly variation of BC concentrations and the meteorological parameters during the winter. The low concentration hours were attributed with the high wind speeds as well as an increase in atmospheric temperature. These conditions were favorable for an increased mixing height and lateral dispersion. The decreasing and increasing trends can be attributed to the temperature as well as wind speed. When the wind speed and temperature starts to increase, BC concentration shows decreasing trend and vice versa. The wind flow helps in the lateral dispersion of the pollutants from its origin. The wind rose of each month were almost similar to their winter season wind roses (Fig. A.2). Here, it is seen that the wind flow distribution pattern during winter season was completely under the calm condition.

Fig. 4.8 shows the relationships between the BC concentration and meteorological parameters. The BC concentration shows a good relationship with the meteorology. The linear fit between two variables shows the nature of the relation. It shows that the BC is inversely proportional to the temperature and directly proportional to relative humidity and atmospheric pressure. However, in some cases, it is not the case. So further, Spearmans rank correlation coefficient analysis was conducted for establishing the relationship of BC with the meteorological parameters.

Fig. 4.9 shows the monotonic relationship between BC concentration, constituents, and meteorological parameters. BC has a positive correlation with relative humidity, wind direction, and atmospheric pressure, while it is negatively correlated with wind speed, temperature, and solar radiation.

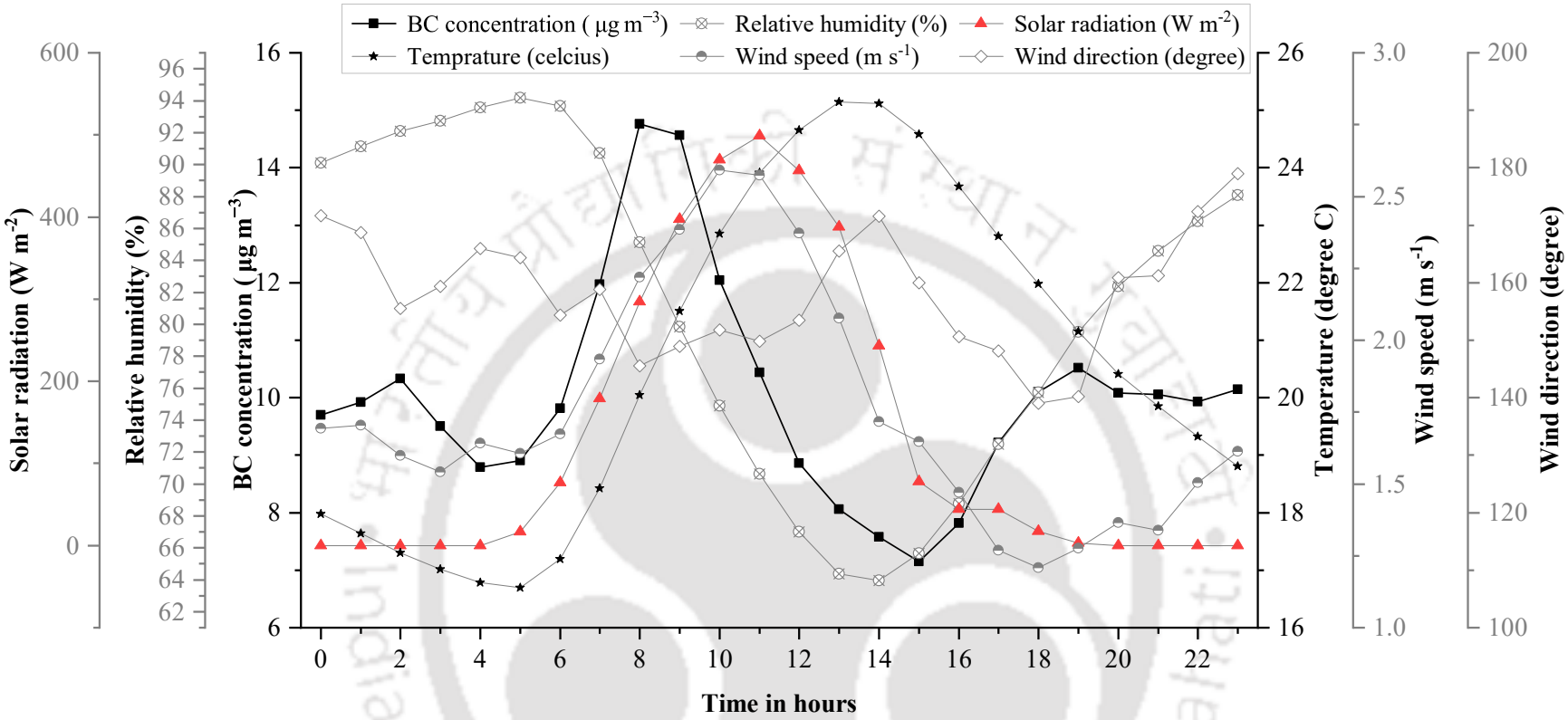

Fig. 4.7 Hourly variation of Black Carbon concentration with the meteorological parameters during the winter period.

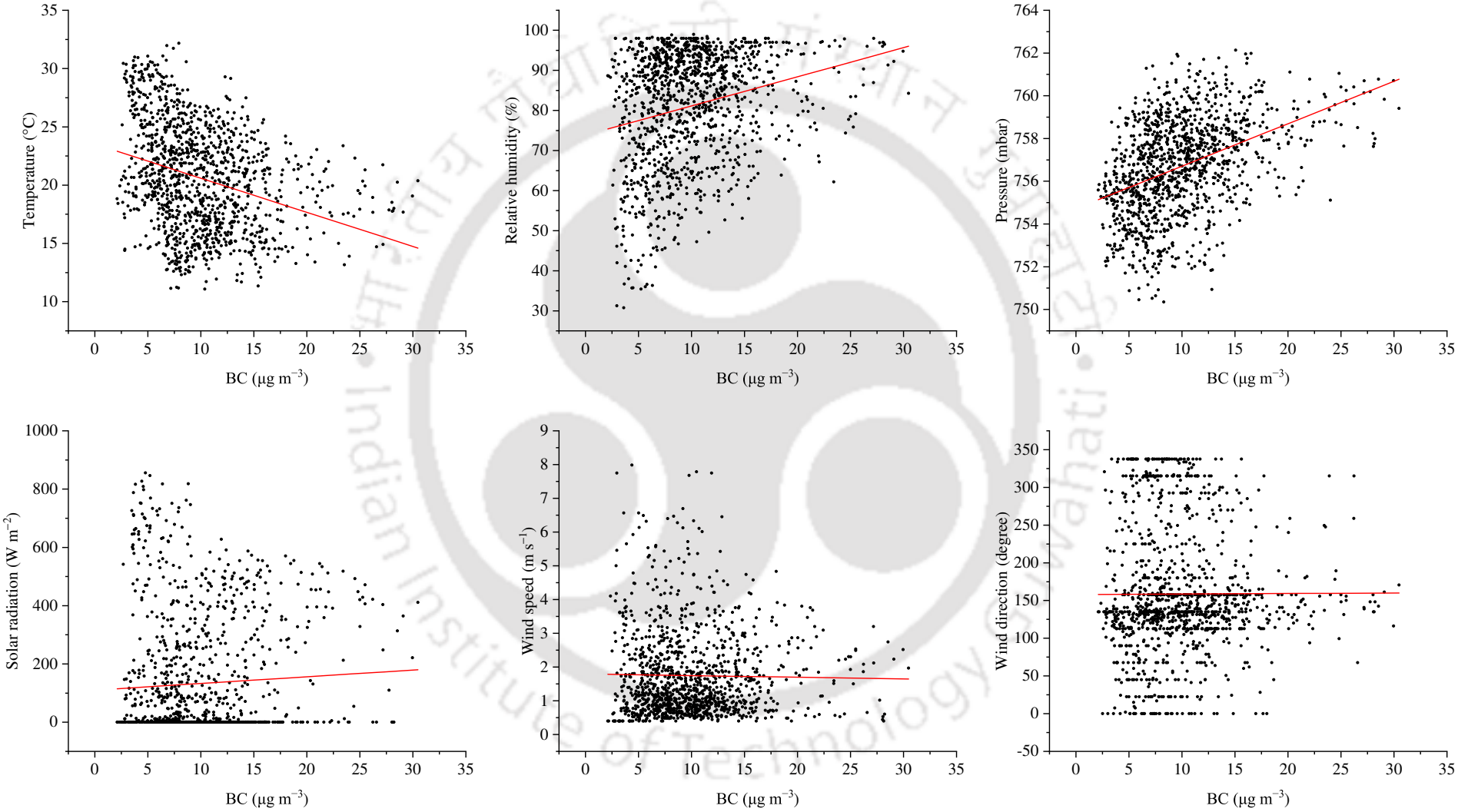

Fig. 4.8 Relationships of hourly-average Black Carbon with the meteorological parameters during the winter period.

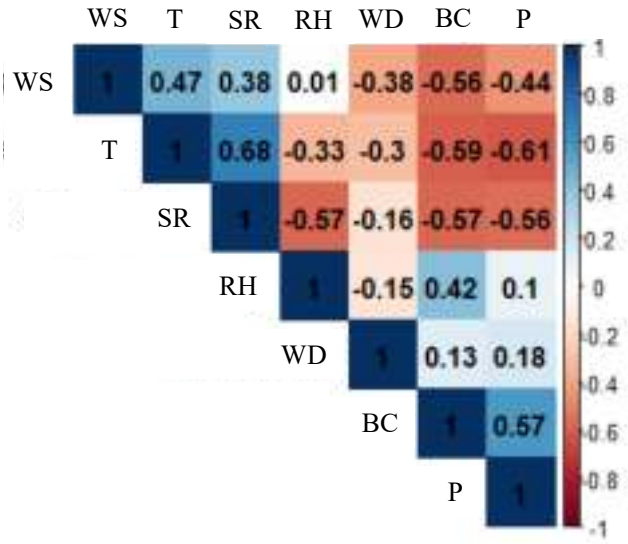

Fig. 4.9 Spearmans rank correlation coefficient between different parameters.

Fig. 4.10a-b show the bivariate polar graphs and condition probability function (CPF) polar plots as a function of BC's wind speed and wind direction. The polar plot shows the influence of the various sectors and the roles of local sources in the BC concentrations (Fig. 4.10a). It was seen that the highest BC level was from the nearby sources. From Fig. 4.10a, it was found that the concentration emitted was of the range of 8-9 $\mu g\ m^{-3}$ from nearby sources for the winter season. There are no prominent nearby sources for BC generated from fossil fuel other than the traffic. Fig. 4.10b shows the wind directions that dominate a high concentration of BC, which is not evident from Fig. 4.10a. Fig. 4.10b clearly shows the highest BC concentration over the study location primarily associated with weak winds ($< 2\ m\ s^{-1}$) from the southeastern direction. This is helpful in the further analysis of the dispersion modelling. It is observed that for the 90^{th} percentile concentration of BC in which, for most wind speed directions, the probability of BC concentrations being greater than the 90^{th} percentile is zero. The calculated percentile is shown at the bottom of the CPF plot.

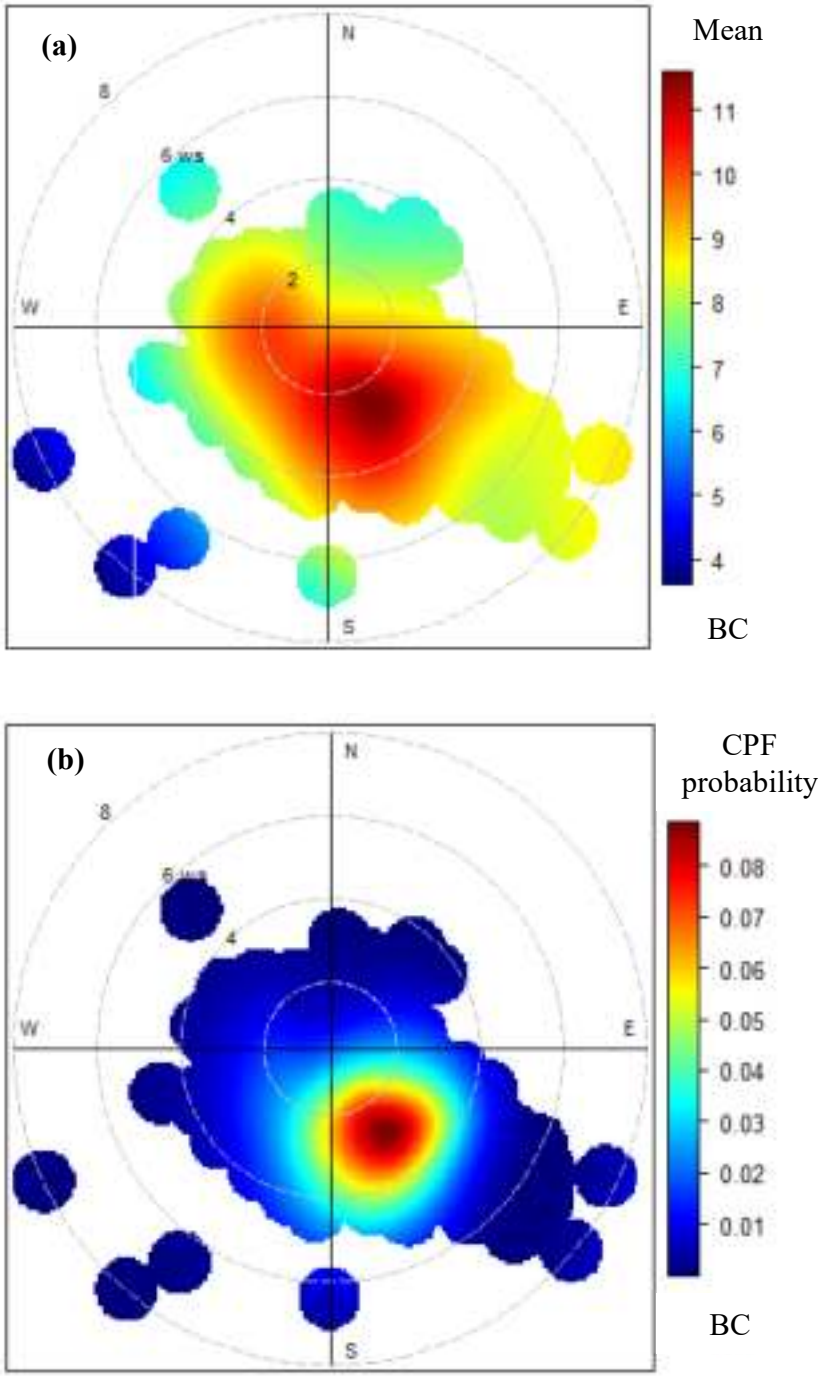

Fig. 4.10 Bi-variate polar plot (a) and CPF plot (b) of Black Carbon concentration higher than the 90th percentile as a function of wind speed and wind direction.

4.2 Trans-boundary influence and fire counts

Apart from the dominance of local sources, the trans-boundary influence on the BC was studied using back-trajectories HYSPLIT model with the help of Fig. 4.11. The back trajectories analyzed by HYSPLIT modelling confirmed the origin of the air masses flowing from northwestern Indo-Gangetic plains to northeastern directions, as shown in Fig. 4.11.

A relatively large intensity of fires was clearly apparent over mountainous regions along the Meghalaya and Nagaland states during March and April 2020. Total fire activities over this region sharply decreased in May probably due to the arrival of the Indian summer monsoon (Fig. 4.12). The fire maps (at >90% confidence interval) for selected months were downloaded from the Fire Information for Resource Management System (FIRMS: https://firms.modaps.eosdis.nasa.gov/) and showed them in Fig. 4.12. This fire spot data was a combined product from Terra and Aqua MCD 14 ML at 1 km resolution.

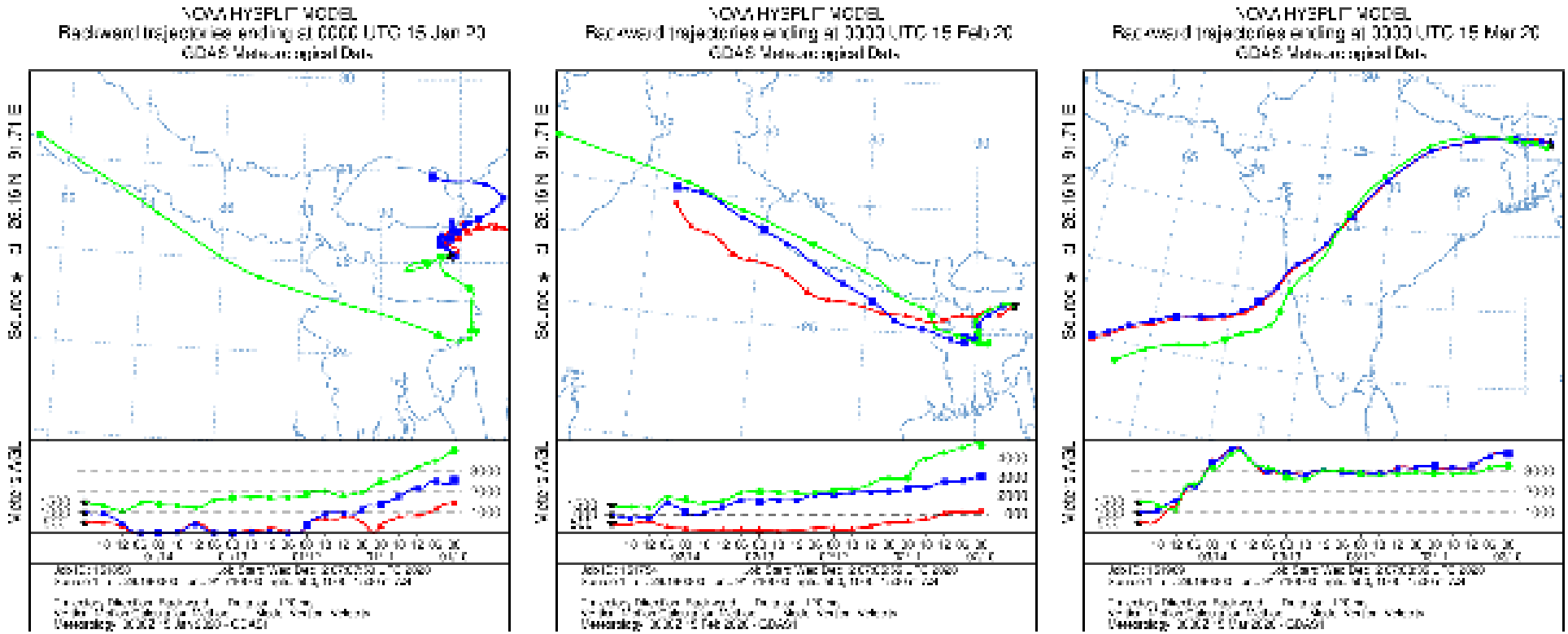

Fig. 4.11 Five days air-mass back trajectories at 500 m above ground level over the monitoring station, indicated by a solid black star.

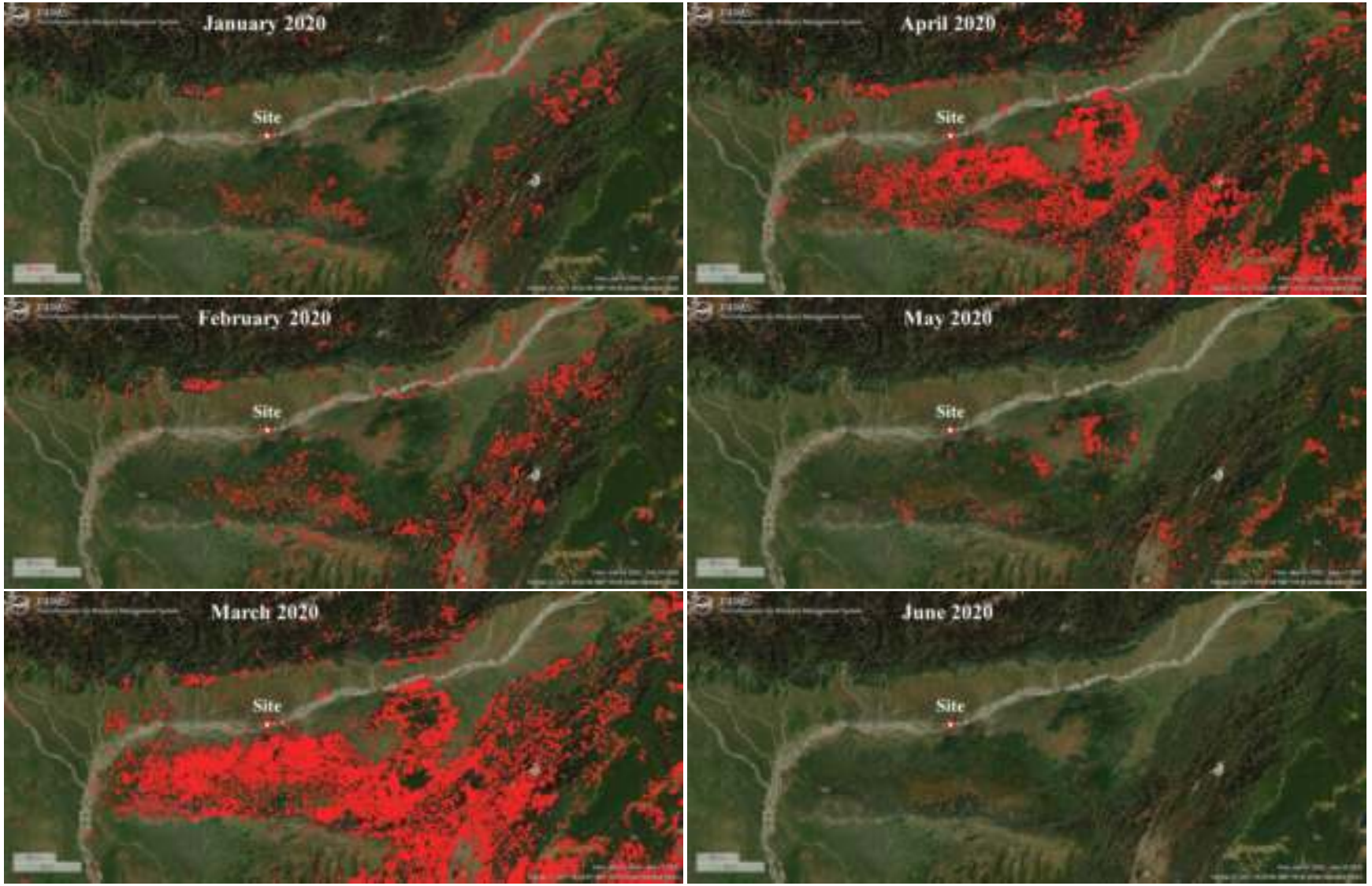

Fig. 4.12 Monthly fire counts over northeastern region of India. The red star shows the location of Guwahati.

4.3 Impacts of Black Carbon and $PM_{2.5}$ on human health

In this study, we have estimated the health risks of atmospheric BC to the local inhabitants of the study region in equivalent amounts of passive cigarettes. BC also contains trace metals and PAHs (IARC, 2014; Lin et al., 2019). Health risks of BC pollution and PSC are comparable (Van der Zee et al., 2016; Wu et al., 2018; Pani et al., 2020) because (i) both risks have the same exposure route, i.e., inhalation (ii) both lead to similar health effects, and (iii) exposure to both environmental tobacco smoke and BC pollution is mostly instinctive (Van der Zee et al., 2016). The health risk estimation tool is proposed by Van der Zee et al. (2016), which is used in this study to estimate the health risks of BC for the four health outcomes, i.e., Low Birthweight of infants (LBWI), percentage lung function decrement of school-aged children (PLFD), lung cancer (LC), and cardiovascular mortality (CM). The tool is primarily based on relative risks. It estimates the risk from the meta-analysis of the reported concentration-response function, which helps characterize the connection between a defined change in BC concentration and health outcomes. We have used the RR as proposed by Van der Zee et al. (2016), which were derived from rigorous systematic reviews. Second, the primary source of uncertainty is the assumed number of daily cigarettes smoked indoors.

We assumed that the daily exposure level of total BC for the people living in Guwahati was equivalent to the daily mean EBC level, which refers to the surplus amount concerning the background BC. The background BC level was for the whole dataset (Jan-March 2020) as the 1.25^{th} percentile of BC concentrations, i.e., $\sim 4\ \mu g\ m^{-3}$ for Guwahati in this study. Table 4.4 presents the summary of health risk estimates of BC expressed in an equivalent number of PSC for each month and the entire study period. Overall, the health risk estimates of BC in this study reached as high as 52.77, 139.98, 51.19, and 24.12 passively smoked cigarette-equivalents to the risk of LBWI, PLFD, CM, and LC, respectively. Exposure of BC pollution in Guwahati was found equivalent to a relatively high number of PCSs concerning the risk of PLFD and a relatively lower number of PSC to the risk of LC. Pani et al. (2020) estimated the health risks posed by BC, reaching maximum values of 6.8, 14.5, 43.5, and 15.3 number of PSC for LC, CM, PLFD, and LBWI, while another study conducted by Wu et al.

(2018) estimated the same risk, reaching maximum values of 31.8, 67.4, 184.4, and 69.5 number of PSC for LC, CM, PLFD, and LBWI, respectively, over the Qinghai-Tibet Plateau. Van der Zee et al. (2016) reported the health risk exposure to 1 $\mu g\ m^{-3}$ of BC being equivalent to 4 PSC per day across for the same four health outcomes. The health risk estimates of BC in Guwahati across all the four health outcomes were equal to 32, 27, and 14 PSC per day for January, February, and March, respectively (Table 4.4). Although these equivalence estimates offer indicative measures of health risks, they carry uncertainty that can only be used to define a considerable health threat to local inhabitants. As Guwahati is typically situated in hilly regions where weak wind speed and topography facilitate the trapping of pollutants, BC can enhance the severity of air pollution by modifying the boundary layer (Wang et al., 2019; Pani et al., 2020) during the winter season and results in more enormous adverse health risks.

The health risk estimates of $PM_{2.5}$ in the study region across all the four health outcomes were equivalent to 39, 28, and 7 PSC per day for January, February, and March, respectively (Table 4.5). The health risk estimates of BC and $PM_{2.5}$ in the study region across all the four health outcomes were equivalent to 37, 30, and 11 PSC per day for January, February, and March, respectively (Table 4.6). These estimates are presented for an increment of 10 $\mu g\ m^{-3}$ in $PM_{2.5}$ and 1 $\mu g\ m^{-3}$ in BC concentration, which is commonly used to express relative risks of these air pollutants (Van der Zee et al., 2016). Overall, the combined (BC and $PM_{2.5}$) health risks into equivalent passively smoked cigarettes were 26 (5) during winter 2020 in Guwahati (Table 4.6). These estimations reveal health risks but with some uncertainty and only describe a significant health hazard to the residents of BRV. These results are necessary to issue public health advisory during haze occasions to safeguard the exposed individuals within the populations.

Table 4.4 Summary of health risk estimates of Black Carbon expressed into equivalent numbers of passively smoked cigarettes per day.

Parameters	January		February		March		Winter	
	Mean	SE	Mean	SE	Mean	SE	Mean	SE
Low Birth Weight of Infants (LBWI)	25	21	21	18	11	9	19	16
Lung function decrement (FEV1) in children (%) (PLFD)	67	27	56	22	29	12	51	20
Cardiovascular mortality (CM)	24	9	21	8	11	4	19	7
Lung cancer (LC)	12	11	10	9	5	5	9	8
Overall estimate	32	17	27	14	14	8	25	13

Table 4.5 Summary of health risk estimates of $PM_{2.5}$ expressed into equivalent numbers of passively smoked cigarettes per day.

Parameters	January		February		March		Winter	
	Mean	SE	Mean	SE	Mean	SE	Mean	SE
Low Birth Weight of Infants (LBWI)	27	16	20	12	5	3	17	10
Lung function decrement (FEV1) in children (%) (PLFD)	68	41	50	30	13	8	44	26
Cardiovascular mortality (CM)	38	11	28	8	7	2	24	7
Lung cancer (LC)	22	7	16	5	4	1	14	5
Overall estimate	39	12	28	8	7	2	25	7

Table 4.6 Summary of health risk estimates of Black Carbon and $PM_{2.5}$ expressed into equivalent numbers of passively smoked cigarettes per day.

Parameters	January		February		March		Winter	
	Mean	SE	Mean	SE	Mean	SE	Mean	SE
Low Birth Weight of Infants (LBWI)	27	14	22	12	8	5	19	10
Lung function decrement (FEV1) in children (%) (PLFD)	70	26	57	20	21	7	50	18
Cardiovascular mortality (CM)	32	7	26	6	9	2	22	5
Lung cancer (LC)	17	7	9	6	4	3	12	5
Overall estimate	37	8	30	6	11	2	26	5

4.4 Descriptive Statistics of various parameters

The statistical parameters of the observed data during winter at Kamakhya hill top and during COVID-19 lockdown at IIT Guwahati was investigated for further inferences. Table 4.7 and Table 4.8 show the descriptive statistics. The mean value for the BC concentration during winter (10.02 μg m^{-3}) was found to be higher than that of COVID-19 lockdown (3.68 μg m^{-3}) period. A large difference in standard deviation and coefficient of variation of BC indicate that the spread of the data was dissimilar during both study period. That means that BC concentration increased and decreased depending upton the vraitions in spread of source i.e. traffic flow and open biomass burning. Since, in both period the values are not same, we can infer that restriction in anthropogenic activities during COVID-19 lockdown reduced the traffic-derived BC emissions. The skewness and kurtosis of the BC data during both winter and COVID-19 lockdown period was found to be positive/right skewed. That means the data is non-normal and distribution has a heavier tail and sharper peak than the normal distribution. Q1, Meadian and Q3 shows the concentration at 25th, 50th and 75th percentiles. It can be inferred that none of the observed parameters follow normal distribution.

Table 4.7 Descriptive statistics of various parameters during winter at Kamakhya hill top.

Parameter	N	Mean	Std. Dev.	Variance	Skewness	Kurtosis	Coefficient of Variation	Minimum	1st Quartile (Q1)	Median	3rd Quartile (Q3)	Maximum	Interquartile range (Q3-Q1)
BC	1201	10.02	4.72	22.32	1.19	2.06	0.47	2.1	6.7	9.17	12.48	30.48	5.78
$PM_{2.5}$	51	79.66	28.25	798.11	0.35	-0.68	0.35	37	54.55	76	99.81	153.79	45.25
PM_{10}	51	118.99	41.03	1683.32	0.65	-0.08	0.34	56.42	90.11	116.45	141.26	215.73	51.16
T	1201	20.59	4.51	20.37	0.21	-0.69	0.22	11.02	17.06	20.44	23.73	32.17	6.65
RH	1201	81.12	14.10	198.89	-0.92	0.21	0.17	30.75	72.25	85	92.75	99	20.05
WS	1201	1.75	1.27	1.63	1.69	3.35	0.73	0.4	0.83	1.32	2.27	7.98	1.45
P	1201	756.70	2.23	4.97	-0.22	-0.36	0.00	750.35	755.25	756.86	758.35	762.13	3.09
SR	1201	133.10	203.77	41526.13	1.49	1.18	1.53	0.00	0.00	0.33	219.67	855.41	219.67

Table 4.8 Descriptive statistics of various parameters during COVID-19 lockdown at IIT Guwahati.

Parameter	N	Mean	Std. Dev.	Variance	Skewness	Kurtosis	Coefficient of Variation	Minimum	1st Quartile (Q1)	Median	3rd Quartile (Q3)	Maximum	Interquartile range (Q3-Q1)
BC	576	3.68	2.01	4.05	1.30	1.86	0.54	0.79	2.18	3.05	4.76	12.35	2.58
T	576	23.23	3.54	12.56	0.26	-0.71	0.15	16.21	20.53	22.99	25.87	32.17	5.33
RH	576	80.43	14.45	208.92	-1.07	0.43	0.17	30.75	72.31	84.33	91.58	99	19.27
WS	576	2.05	1.89	3.60	0.93	-0.11	0.92	0	0.44	1.51	3.27	8.75	2.83
P	576	755.01	1.65	2.72	-0.11	-0.36	0.002	750.45	753.88	755.14	756.09	759.30	2.21
SR	576	156.88	232.68	54140.59	1.37	0.52	1.48	0.00	0.00	8.79	245.13	860.75	245.13

5

Results and Discussion

This chapter presents the results of the research in line with the objectives outlined and discusses the outcome by comparing with the state-of-art literature. The results of analyzed data collected during winter 2020 at Kamakhya hill top are presented.

5.1 Optical properties of BC and contribution

5.1.1 Wavelength-dependent aerosol light absorption

The aerosol light absorption coefficient (b_{abs}) estimates specify a severe turbid atmosphere in this region throughout the study period. Fig. 5.1 shows the hourly time series of the screened b_{abs} at multiple wavelengths for the winter period. The average wavelength-dependent light absorption coefficient for aerosols revealed a power-law fit (insert Fig. 5.1) in the 370-880 nm band; this indicated the occurrence of the light absorbed by B_rC ($b_{abs\_B_rC}$) at shorter wavelengths. The b_{abs} values display significantly high values at shorter wavelengths reaching above 500 Mm^{-1}[†] on several days, while subsequently decreasing at the end of February, which might be attributed to rainfall. Moreover, a remarkable decrease in b_{abs} can be seen from cold to hot days, indicating a severe turbid atmosphere in this region. The winter average b_{abs} (at 370 nm) value was 231 Mm^{-1}. At 520 nm (central wavelength), it was found to be 152.7 ± 27.9 Mm^{-1}, while at 880 nm, it dropped to 77.9 ± 14.6 Mm^{-1}, implying that the light absorption was by BC alone.

[†]radiation in per million meter.

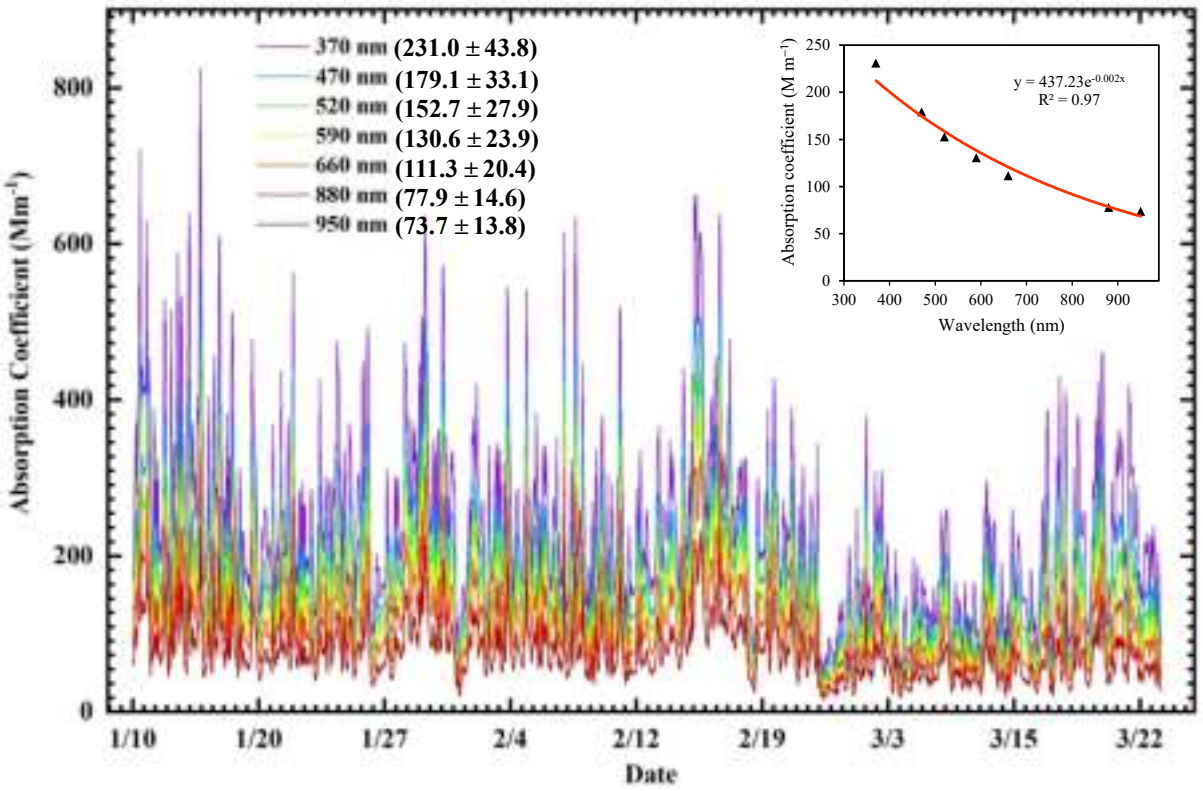

Fig. 5.1 Screened hourly time series of aerosol light absorption at seven discrete wavelengths throughout the study period.

The wavelength dependence of b_{abs} is expressed via the AAE values, which indicate different aerosol types. In this study, most of the $AAE_{370\text{-}880}$ values were in the range of 1.0-1.7 (median of 1.23), signifying the dominance of FF combustion and implying the event of both primary and secondary $b_{abs\_B_rC}$. The lower AAE values ranging from 1.18-1.20 in the morning period (09:00-11:00 LST) for both bands (370-880 nm and 470-950 nm) showed the increased influence of FF emissions released from heavy-duty vehicles in the previous night (Fig. 5.2). The peak $AAE_{370\text{-}880}$ of about 1.31 was found at 19:00 LST, aligning with the increased demand for residential cooking and heating. Dumka et al. (2018) used AAE_{FF} as1.0 and AAE_{BB} as 1.8 for the approximation of the BC_{FF} and BC_{BB} in Delhi, India, likewise Pani et al. (2020) in Chiang Mai, Thailand and Vaishya et al. (2017) in Gorakhpur (IGPs), India. The AAE_{BB} and AAE_{FF} value in the range of 1.68-2.2 and 0.9-1.1, respectively, are used in source apportionment studies (Dumka et al., 2018; Barman and Gokhale, 2019; Pani et al., 2020; Stockwell et al., 2016; Zotter et al., 2017). The AAE_{BB} strongly depends on biomass and its combustion type and can vary up to 3.5 (Dumka et al., 2018).

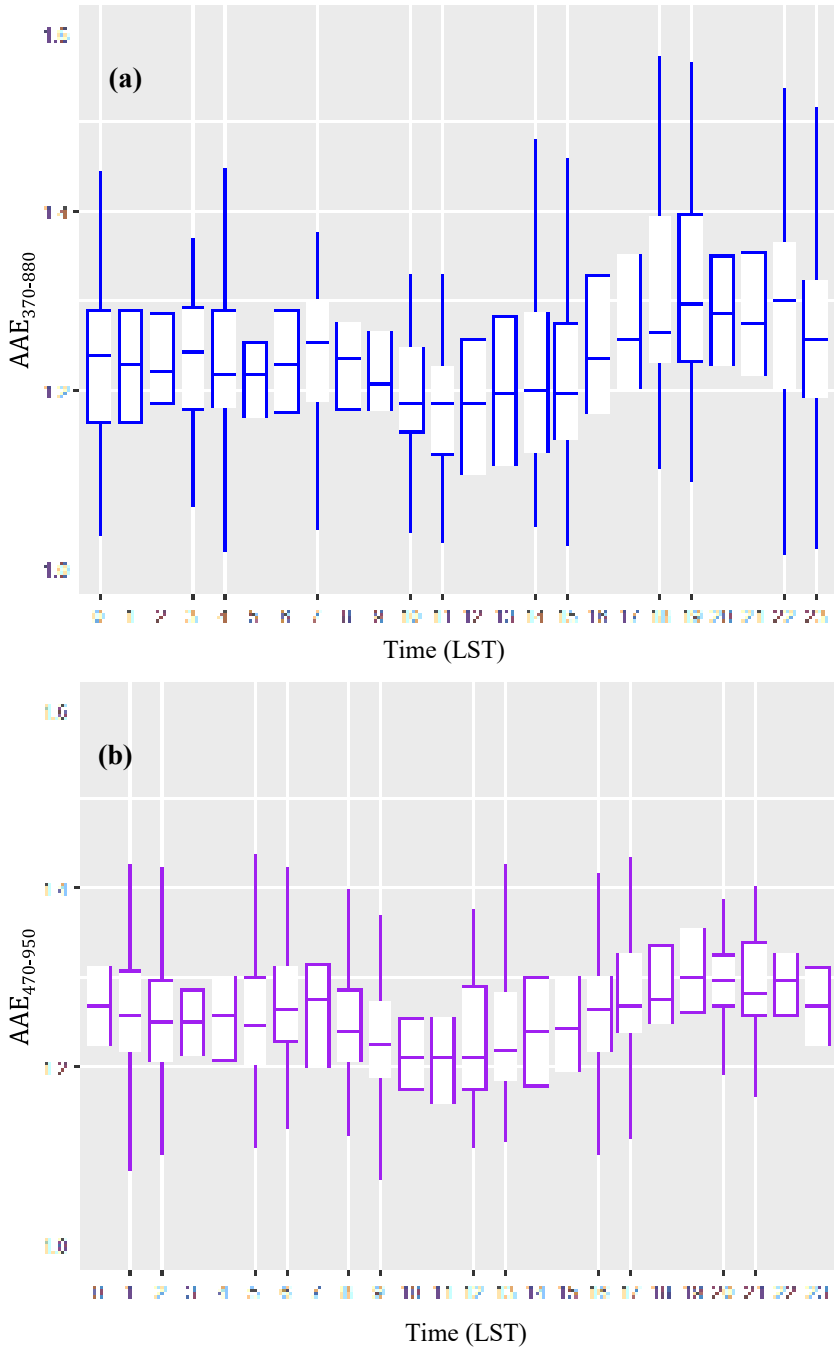

Fig. 5.2 Mean diurnal pattern of (a) $AAE_{370\text{-}880}$ and (b) $AAE_{470\text{-}950}$.

However, the fraction (for 370-880 nm) $AAE_{370\text{-}880}$>1.5 was found to be much higher (6%) than the fraction (for 470-950 nm) $AAE_{470\text{-}950}$> 1.5 (1.3%), indicating lesser impacts of BB as the wavelength increased. Hence, the pair of 370-880 nm and AAE_{FF} as 1.0 and AAE_{BB} as 1.7 was selected. This combination was used to assess the role of FF and BB in the whole BC mass. The $AAE_{370\text{-}880}$ average value was 1.25 ± 0.04. It was observed to be the highest during winter nighttime (1.28 ± 0.02).

5.1.2 Primary and secondary Brown Carbon

Fig. 5.3 shows the winter-average diurnal variation in B_rC and B_rC_{sec} absorption at 370 nm. Fig. 5.3a showed that the light absorption by B_rC ($b_{abs\_B_rC}$) at 370 nm decreased after 23:00 LST, reached a low value of 38.0 Mm^{-1} around 06:00 LST, then rapidly increased at a rate of 8.96 Mm^{-1} per hour to a daily maximum of 64.9 Mm^{-1} around 09:00 LST. From then, it decreased sharply at a rate of 5.45 Mm^{-1} per hour and reached a daily minimum (26.7 Mm^{-1}) around 16:00 LST in the afternoon. Finally, it showed a peak of 64.4 Mm^{-1} around 20:00 LST in the evening and later decreased once more.

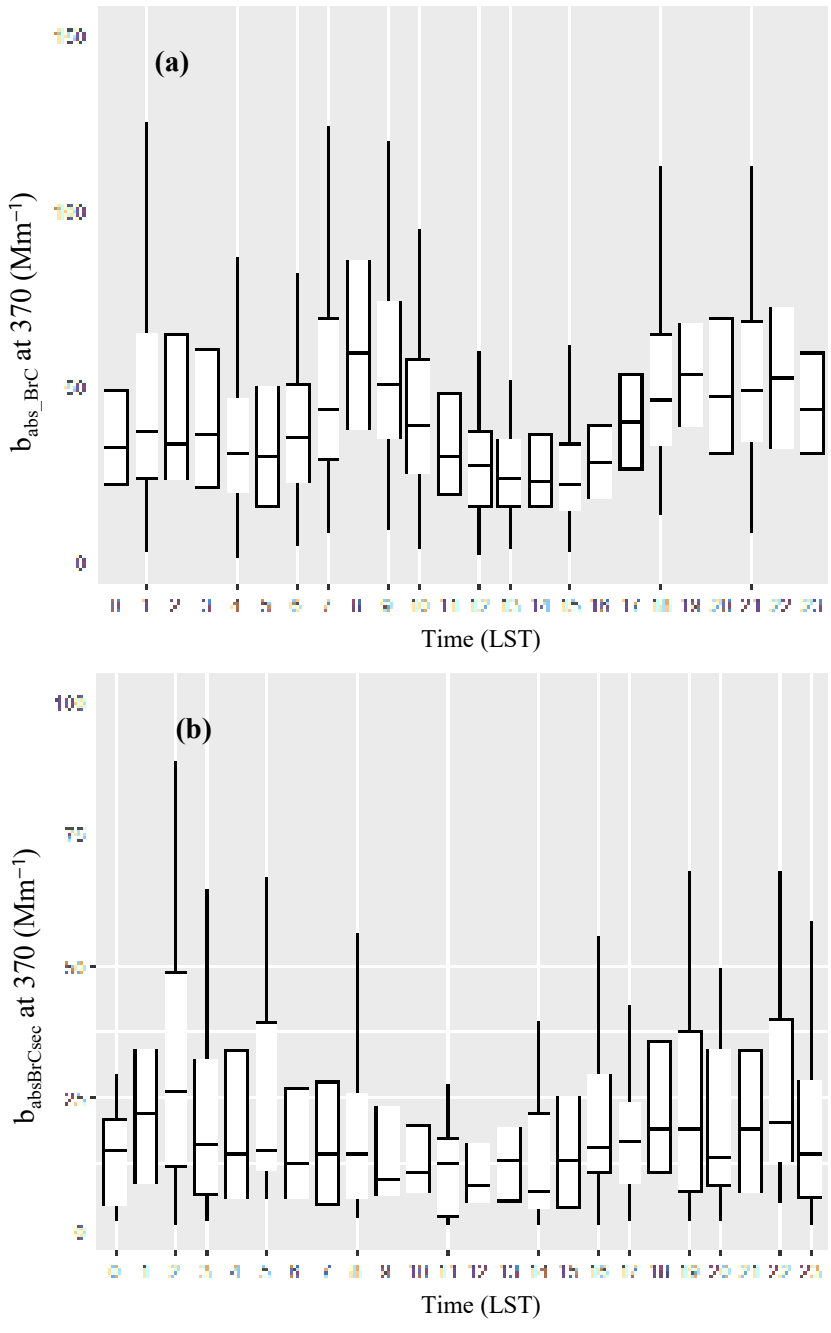

Fig. 5.3 Mean diurnal pattern of (a) B_rC and (b) B_rC_{sec} absorption to the total b_{abs}.

Similarly, Fig. 5.3b showed that the light absorption by secondary B_rC ($b_{abs\_B_rC_{sec}}$) at 370 nm increased after midnight and reached a maximum of 28.8 Mm^{-1} around 03:00 LST. From then, it decreased sharply (in between a few zigzag patterns) and reached a daily minimum of 11.21 Mm^{-1} around 15:00 LST at a rate of 1.4 Mm^{-1} per hour. Finally, it showed a small peak of 21.4 Mm^{-1} and later decreased once more.

5.2 Contribution of primary and secondary Brown Carbon

Fig. 5.4 shows the average $b_{abs\_B_rC}$ and $b_{abs\_B_rC_{sec}}$ contribution (%) to total b_{abs} at a shorter wavelength (370 to 660 nm) during winter, winter daytime, and winter nighttime. The $b_{abs\_B_rC}$ involvement varied typically depending on meteorological conditions and wavelength (from UV to IR). It was found in the range of 0-45% at 370 nm, while at 660 nm, it was 0-13% (Fig. A.3). The total average contribution of $b_{abs\_B_rC}$ and $b_{abs\_B_rC_{sec}}$ to b_{abs} was 14.2% and 5.0%, respectively, indicating significant B_rC and B_rC_{sec} contributions to light absorption during winter nighttime, and were reduced during winter daytime (13.2% and 4.5%).

The $b_{abs\_B_rC}$ absorption shows a heteroscedastic arrangement as a result of growing BC mass throughout the winter season, subsequently contained by greater concentration ranges, $b_{abs\_B_rC}$ may differ up to ~150 Mm^{-1}. This huge inconsistency could be due to the effect of different BC emission sources, altered mixing conditions, the physicochemical composition of the B_rC types, variations in solar radiation, and local meteorology (Liakakou et al., 2020; Shamjad et al., 2016). Calculations based on the field measurements showed that the average contribution of B_rC to the total b_{abs} ranged from 6.6% to 18.0%, suggesting a significant B_rC contribution to aerosol light absorption. Our evaluations revealed the B_rC contribution of 18.0% and 17.4% in winter at 370 nm and 470 nm, respectively. The B_rC contribution at different wavelengths shows a falling variation, with the highest in January corresponding to the impact of residential BB. Li et al. (2018) conveyed 10-16% contribution (at 405 nm) in pre-monsoon and 19-15% in winter at rural and urban sites in Guangzhou, China, while increasing in rural areas. Using a similar approach, Qin et al. (2018) reported a $b_{abs\_B_rC\_370}$ value of 13.67 Mm^{-1} along with contribution of ~24% at suburban Guangzhou, and China and Liakakou et al. (2020) also stated a similar B_rC contribution of 21.65% at the urban

background of Athens, in winter. In winter, another study conducted by Yuan et al. (2016) presented a ~6% $b_{abs\_B_rC\_405}$ contribution at an urban and ~12% at a rural location in the Pearl River delta, China. Overall, a summary of the literature review shows generally more outstanding contributions in rural regions due to the more significant influence of BB from domestic fuels. The significant $b_{abs\_B_rC}$ contributions projected in suburban Guwahati reveal enormously absorbing B_rC aerosols during the winter (especially on winter nights until the early morning) produced by BB for heating purposes.

A huge secondary organic carbon fraction of organic particles is contributed from remote and sparsely populated areas (Zheng et al., 2017), whereas the fastest growing city of Northeast, India, found the contribution of $b_{abs\_B_rC_{sec}}$ during winter nighttime of 9.8% than daytime (7.3%). The average $b_{abs\_B_rC_{sec}}$ contributed about 48% of the total $b_{abs\_B_rC}$ at 370 nm, 33% at 470 nm, 26% at 520 nm, 21% at 590 nm, and 19% at 660 nm with higher contributions for nighttime (21-49%) compared with the daytime (17-46%). These results show a significant contribution from secondary sources to B_rC absorption in the lower Brahmaputra river basin of Northeast India, especially during the nighttime.

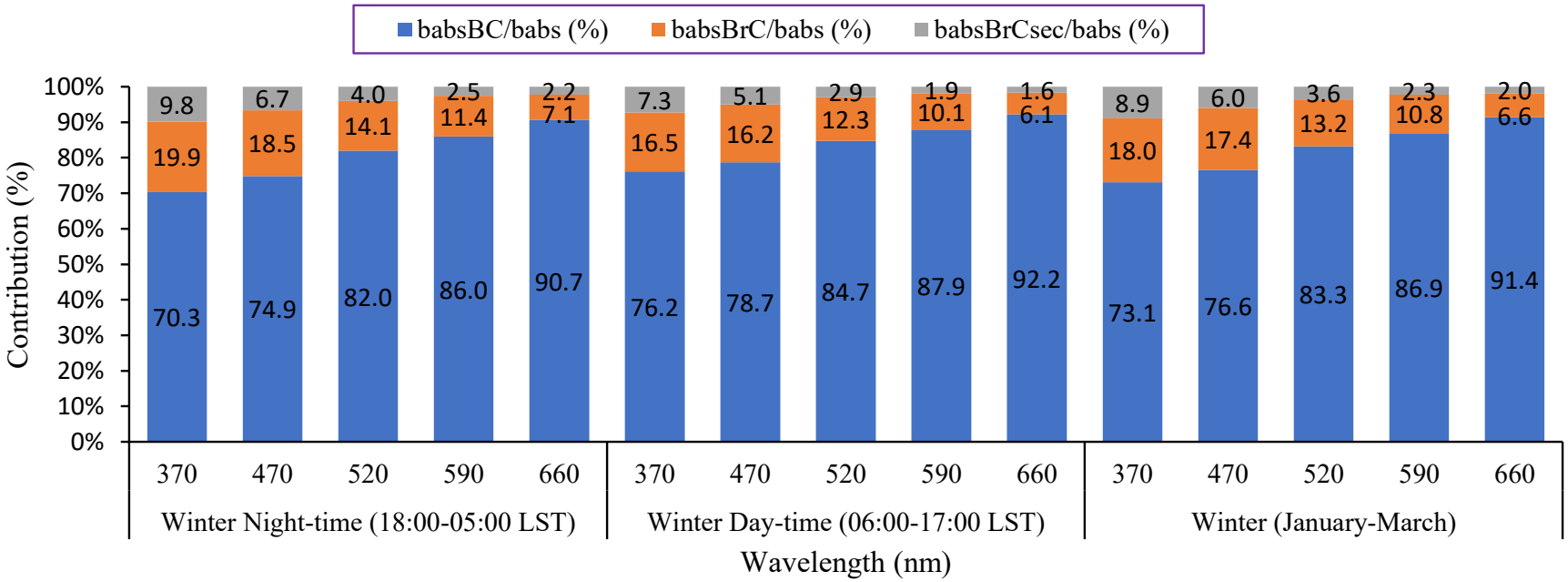

Fig. 5.4 Contribution of the Black Carbon, Brown Carbon, and secondary Brown Carbon absorption to the total aerosol light absorption at different wavelengths.

5.3 Contribution of fossil fuel and biomass burning to Black Carbon concentration

The daily averaged BC_{880} mass concentrations ranged from 3.8 to 20.6 $\mu g\ m^{-3}$ (mean ± standard deviation of 10.0 ± 3.2 $\mu g\ m^{-3}$) (Fig. 5.5a). The last few days of the study period (in March 2020) pertaining to the COVID-19 pandemic showed the lowest BC concentrations, which reduced to 2.10 $\mu g\ m^{-3}$. It shows the direct effect of no vehicular activities. The daily averaged BC_{FF} concentrations at 880 nm ranged from 3.0 to 16.3 $\mu g\ m^{-3}$, while the corresponding range for the BC_{BB} was from 0.7 to 6.5 $\mu g\ m^{-3}$ (Fig. 5.5b-c). Such a high BC level may have negative impacts on human health and the eco-sensitive areas of this region.

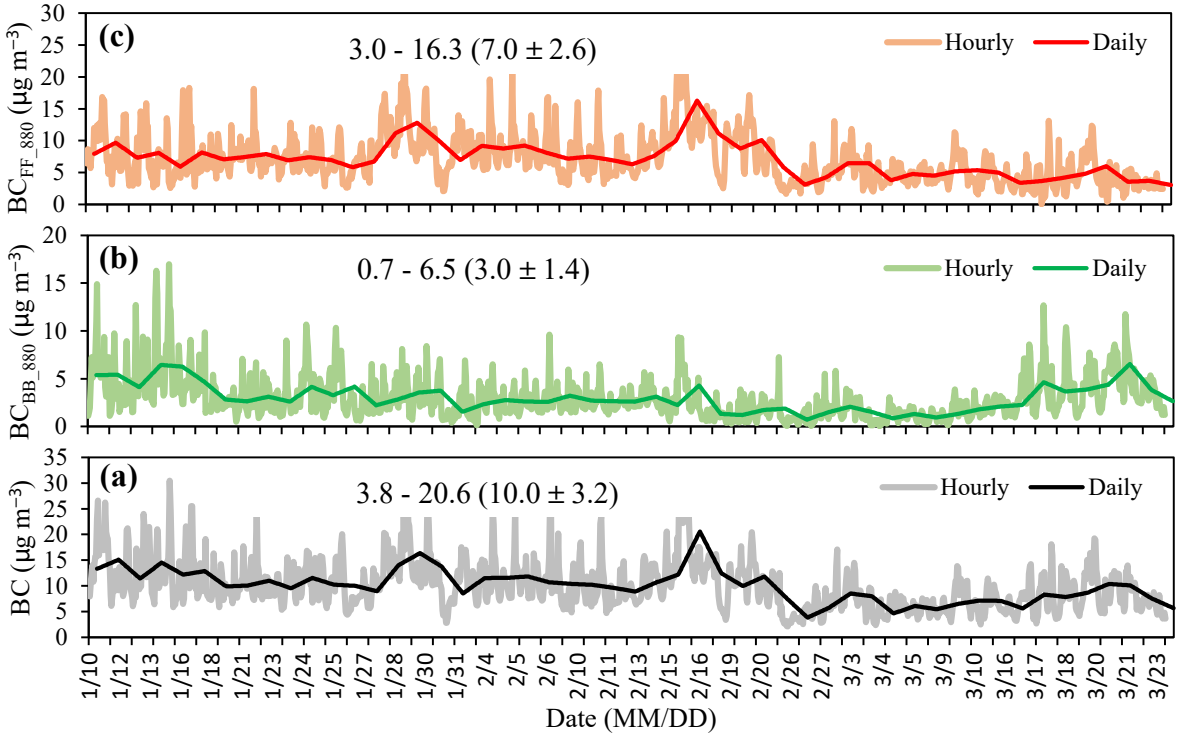

Fig. 5.5 Hourly and daily variation of (a) BC_{880}, (b) BC_{BB_880} and (c) BC_{FF_880} concentrations in Guwahati during January to March 2020. The range, the mean values, and standard deviation (in parenthesis) are given in each plot.

Daily contribution of BC_{FF} to the total BC at 880 nm varied significantly in the range of 35.2% to 89.32%, and the daily BC_{BB}/BC fraction ranged from 10.7% to 64.8%. The winter average contribution of BC_{BB} to BC at 880 nm was 30%, much smaller than that of BC_{FF} (70%) (Fig. 5.6). The contribution of FF dominates the BC with 70% due to many vehicular activities, while it was estimated to be 82% using the default technique of the AE-33 model (Fig. 5.7).

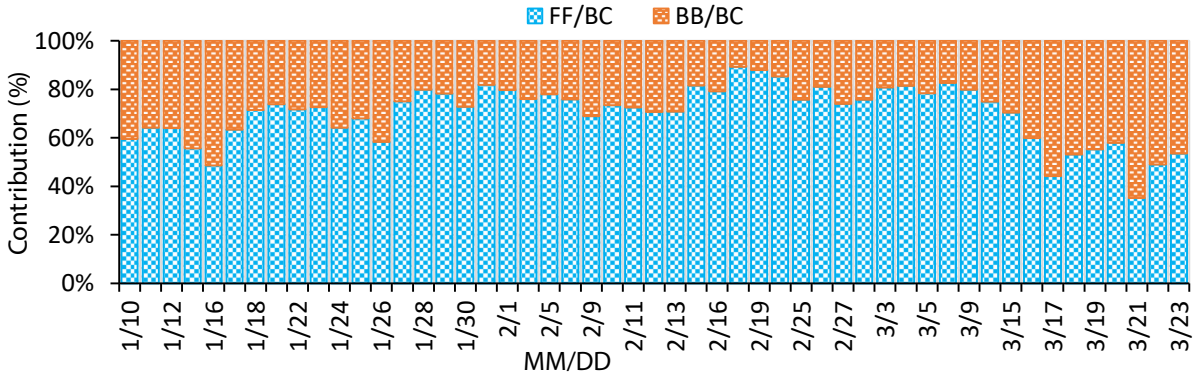

Fig. 5.6 Daily contribution of FF and BB to the total Black Carbon in winter 2020.

The BC_{FF} and BC_{BB} mass concentrations were estimated using the MAC values of the AE-33 model so that a direct comaprision can be made with the literature BC levels over BRV. In Guwahati, the highest BC concentration (by AE-33) near urban rodways is about 23 μg m^{-3} within the lowest layer of about 12 m from the ground (Barman and Gokhale, 2019). Another study in December 2011 is 9-41 μg m^{-3} measured using a micro Aethalometer (AE-51) (Chakrabarty et al., 2012). Table 5.1 summarizes the BC_{BB} vs BC_{FF} contributions from earlier studies in India and overseas, along with the present results. However, the present BC_{BB} values were near to those found in Delhi (Dumka et al., 2018) and Gorakhpur in winter (Vaishya et al., 2017), a current study in Guwahati (Barman and Gokhale, 2019) show only 14% involvement for the BC_{BB} (**??**). The dissimilarity may be justified by the difference in the techniques used. The BC_{BB} contribution increased in urban areas, which might be due to the emissions transported from forest fires and agricultural burning (Pani et al., 2020). The BC_{FF} constituent is entirely attributed to automobile emissions in metropolises worldwide (Dumka et al., 2018; Mousavi et al., 2018; Vaishya et al., 2017; Zotter et al., 2017). In March, the comparatively lower BC in the last few days could be attributed to the intermittent pre-monsoon showers and the nationwide lockdown imposed due to the

COVID-19 pandemic, which stopped the traffic activities.

5.4 Sensitivity analysis of the Aethalometer (AE-33) model

The sensitivity of the Aethalometer model was investigated by using different AAE_{FF} and AAE_{BB} combinations (Fig. 5.7). This analysis was conducted by changing the AAE_{FF} and AAE_{BB} values from 0.9 to 1.1 and 1.6 to 2.2, respectively. The BC_{FF}/BC ratio increased with an increase in AAE_{FF} value, and there was even a more rapid increase in that fraction when AAE_{BB} increased. While the BC_{BB}/BC fraction decreased with the increasing AAE_{FF} and AAE_{BB} values. In this test, the BC_{FF} contributions were in the range from 57% (AAE_{FF} = 0.9, AAE_{BB} = 1.6) to 91% (AAE_{FF} = 1.1, AAE_{BB} = 2.2). This analysis also indicates that the apportionment results are more sensitive to the changing AAE_{BB} values than to AAE_{FF} values. For example, keeping the AAE_{FF} value at 1.0, the BC_{FF}/BC increased from 64% to 87% for the AAE_{BB} value from 1.6 to 2.2. However, a slower increase in BC_{FF}/BC fraction, 83% to 91%, was found when AAE_{FF} value changes from 0.9 to 1.1 by fixing the AAE_{BB} value at 2.2. It is different from previous studies over Delhi in India (Dumka et al., 2018) and Granada in Spain (Titos et al., 2017). Both found the Aethalometer model was more sensitive to AAE_{BB} than to AAE_{FF}.

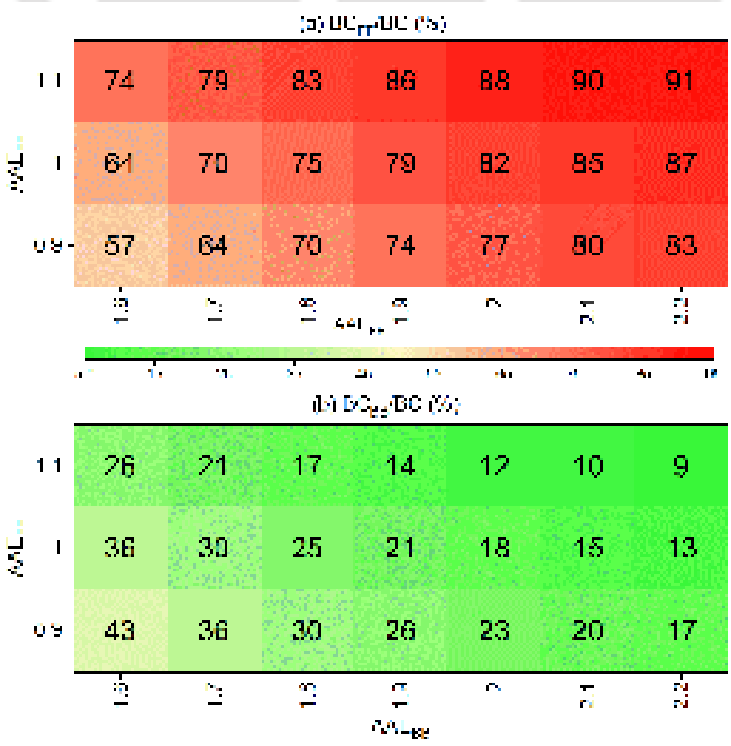

Fig. 5.7 Variations in the (a) BC_{FF}/BC and (b) BC_{BB}/BC fractions at 880 nm with AAE_{FF} and AAE_{BB}.

Table 5.1 Contribution of the BC_{FF} and BC_{BB} in the total BC at different sites worldwide.

Measurement site	Site type	Period	BC_{FF}(%)	BC_{BB}(%)	References
Guwahati, India	Suburban-hilly	Jan to Mar 2020	70%	30%	This study
Guwahati, India	Rural	Dec 2016 to Feb 2017	86%	14%	Barman and Gokhale (2019)
Guwahati, India	Urban	Dec 2016 to Feb 2017	85%	15%	Barman and Gokhale (2019)
Delhi, India	Urban	Dec 2015 to Feb 2016	72%	28%	Dumka et al. (2018)
Delhi, India	Urban	Dec 2011 to Mar 2012	94%	6%	Tiwari et al. (2015)
Gorakhpur, India	Urban	Aug 2013 to Jul 2015 (winter)	74%	26%	Vaishya et al. (2017)
Ahmedabad, India	Urban	Dec 2016 to Feb 2017	77%	23%	Rajesh and Ramachandran (2018)
Agartala, India	Rural	Jan 2011	56%	44%	Kaur et al. (2020)
Vijaywada, India	Suburban	Jan to Dec 2016 (winter)	79%	21%	Prasad et al. (2018)
Dehradun, India	Urban	Dec 2019 to Feb 2020	83%	17%	Prabhu et al. (2020)
Beijing, China	Urban	Dec 2015 to Feb 2016	50%	60-83%	Liu et al. (2018)
Zurich, Swiss	Urban	Jan 2006	81%	19%	Zotter et al. (2017)
Athens, Greece	Suburban	Mar 2013 to Feb 2014 (cold period)	79%	21%	Diapouli et al. (2017)
Granada, Spain	Urban	Nov 2014 to Feb 2015	70%	30%	Titos et al. (2017)
Chiang Mai, Thailand	Urban	Mar to May 2016	35%	65%	Pani et al. (2020)
Ontario, Canada	Urban	Jun 2015 to May 2016 (Winter)	65%	35%	Healy et al. (2017)
Los Angeles, USA	Rural/agricultural	2016 to 2017 (Winter)	91%	9%	Mousavi et al. (2018)
Helsinki, Finland	Suburban	Jan to May 2017	54%	46%	Helin et al. (2018)

5.4.1 Diurnal patterns of fossil fuel and biomass burning associated Black Carbon

The winter averaged diurnal patterns of BC_{FF} and BC_{BB} at 880 nm are shown in Fig. 5.8. The BC_{FF} concentrations were usually high during morning hours (08:00 to 10:00 LST) due to emissions from buses and cars, as many devotees usually visit the Ma Kamakhya temple during these hours. The daily maximum (10.7 $\mu g\ m^{-3}$) of BC_{FF} was observed around 10:00 LST and then decreased at a rate of 0.89 $\mu g\ m^{-3}$ per hour to a daily minimum (5.4 $\mu g\ m^{-3}$) around 04:00 LST. After that, it started increasing from evening to early morning hours (03:00 LST). The BC_{FF} concentration was high during the night and early morning (6:00 to 11:00 LST), which might be due to the emissions from trucks and city buses (Fig. 5.8). A noticeable variation in BC_{FF} was observed during morning rush hours (~08:30 to ~10:30 LST), while it was consistent throughout the day. High (>25 $\mu g\ m^{-3}$) BC_{FF} concentration was observed on some days. BC concentration peaks were detected in the morning rush hours on most days. This may be caused by increased vehicular activity during these hours, changes in mixing layer height, and fog occurrence in the valley. The BC_{BB} concentrations exhibit significant diurnal variations with sudden high values from evening to nighttime (~17:00 to ~23:00 LST) due to increased BB for cooking and heating (Fig. 5.8b). On some days, elevated BC_{BB} concentrations continue till morning hours. BC_{BB} showed a daily maximum around 09:00 LST (4.19 $\mu g\ m^{-3}$) and then decreased to a daily minimum of 1.72 $\mu g\ m^{-3}$ around 15:00 LST. From then, it started increasing till residential cooing hours (20:00 LST) and then started dropping till early morning hours (06:00 LST).

The main findings are: (i) the highest (0.78) BC_{FF}/BC ratios in the late morning to early afternoon hours (~11:00 to 13:00 LST), (ii) the progressive increase of BC_{BB}/BC from afternoon to evening reaching at 0.38 in 19:00 to 20:00 LST and, (iii) the more significant daily variation of the ratio values at morning and mid-night hours.

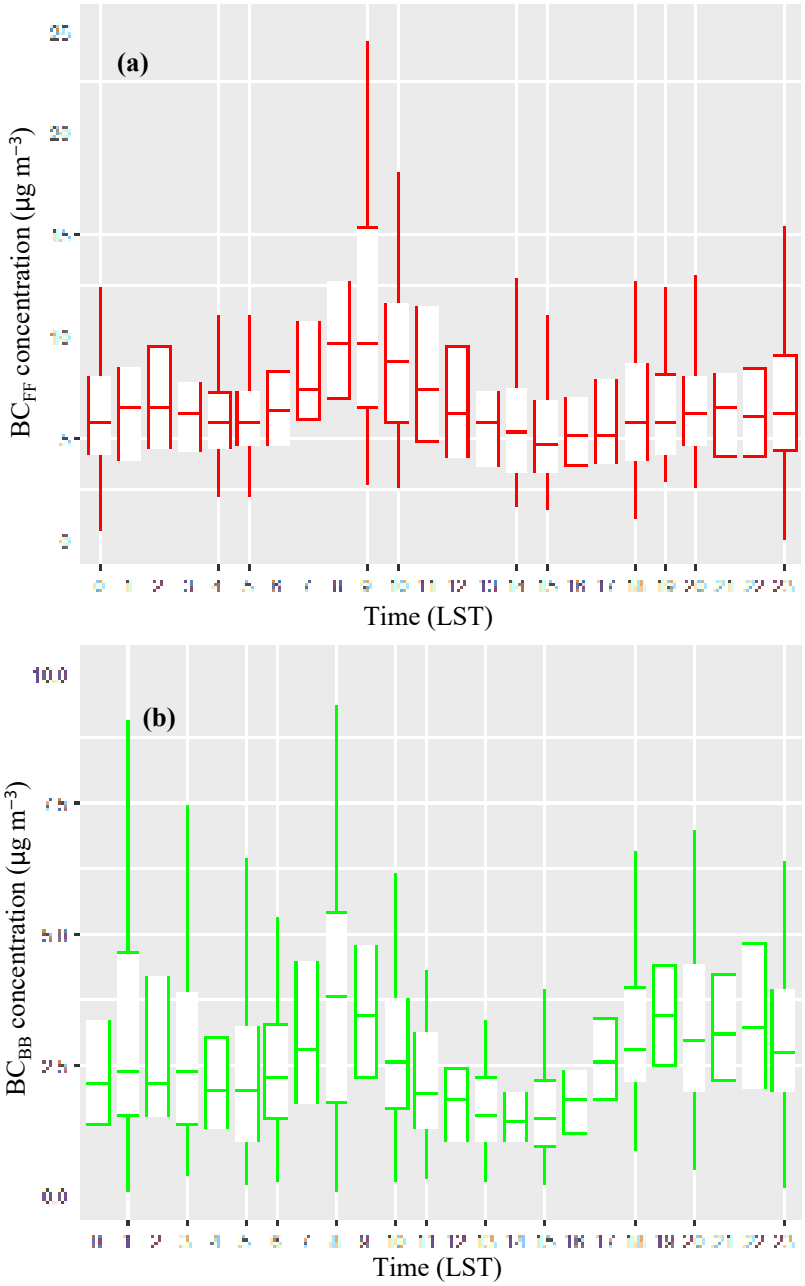

Fig. 5.8 Mean diurnal pattern of (a) BC_{FF} concentration, (b) BC_{BB} concentration.

5.5 Source apportionment and Brown Carbon spectral absorption

The $b_{abs\_B_rC}$ absorption shows a heteroscedastic arrangement due to growing BC mass throughout the winter season, subsequently contained by greater concentration ranges, $b_{abs\_B_rC}$ may differ up to ~150 Mm^{-1}. This huge inconsistency can be due to the effect of unlike BC emission sources, altered mixing conditions, the physicochemical composition of the B_rC types, variations in solar radiation, and local meteorology such as photo-bleaching (Liakakou et al., 2020; Shamjad et al., 2016). A weak dependency ($R^2 = 0.4$) amongst $b_{abs\_B_rC}$ and BC mass concentration in winter suggests the various emission sources concerning the two constituents (Fig. 5.9).

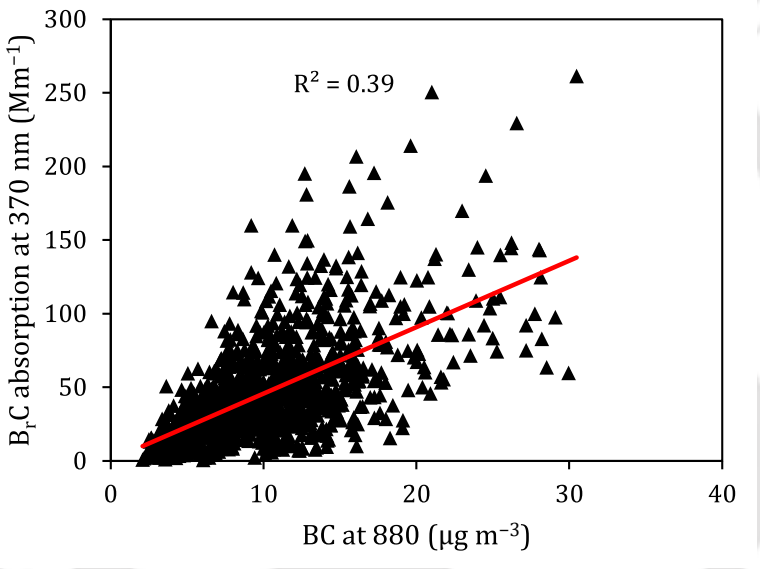

Fig. 5.9 Correlation between $b_{abs\_BrC\_370}$ with Black Carbon mass concentration at 880 nm.

Likewise, we studied the ratios of $b_{abs\_B_rC}$ at multiple wavelengths relating to that at 370 nm to study the temporal variations in absorbing constituents and the probable presence of distinct forms of chromophores accountable for variations in the $b_{abs\_B_rC}$ absorption. The additional investigation exposed a sharp rise in $b_{abs\_B_rC}$/BC ratio during the residential cooking hours in the evening (Fig. 5.10a) during winter. The daily patterns were more flexible throughout the study period at a shorter wavelength (370 nm and 470 nm), revealing a higher $b_{abs\_B_rC}$/BC ratio at similar wavelengths. For example, Humic-Like Substances (HULIS) initiating from BB absorb intensely at short wavelength (370 nm), whereas nitro-aromatic compounds engage more at wavelengths greater than ~400 nm (Graber and Rudich, 2006; Satish et al., 2017). During winter nights with enhanced wood burning for heating purposes, the ratio of b_{abs_470}/b_{abs_370} reduced, proposing a higher growth rate in b_{abs} at 370 nm (Fig. 5.10b). It indicates the presence of HULIS in B_rC_{pri} emission (Liakakou et al., 2020; Satish et al., 2017). The photobleaching result was not subsequently evident as seen in highly contaminated sites in India (Satish and Rastogi, 2019) and other parts of the world (Liakakou et al., 2020) even though the slight reduction of ratios during the early afternoon (~08:30-11:30 LST). The HULIS absorption efficiency declines at longer wavelengths, predominantly when they originate from BB, so the ratio b_{abs_590}/b_{abs_370} and b_{abs_660}/b_{abs_370} exhibit insignificant diurnal patterns (Fig. 5.10b). Instead, growth in the absorption ratios, particularly those of b_{abs_470}/b_{abs_370}, in the morning to late afternoon hour might be credited to the occurrence of nitro-phenolic and nitro-aromatics B_rC composites from the on-road stream of traffic associated volatile organic compounds (Liakakou et al., 2020; Lin et al., 2014; Satish et al., 2017).

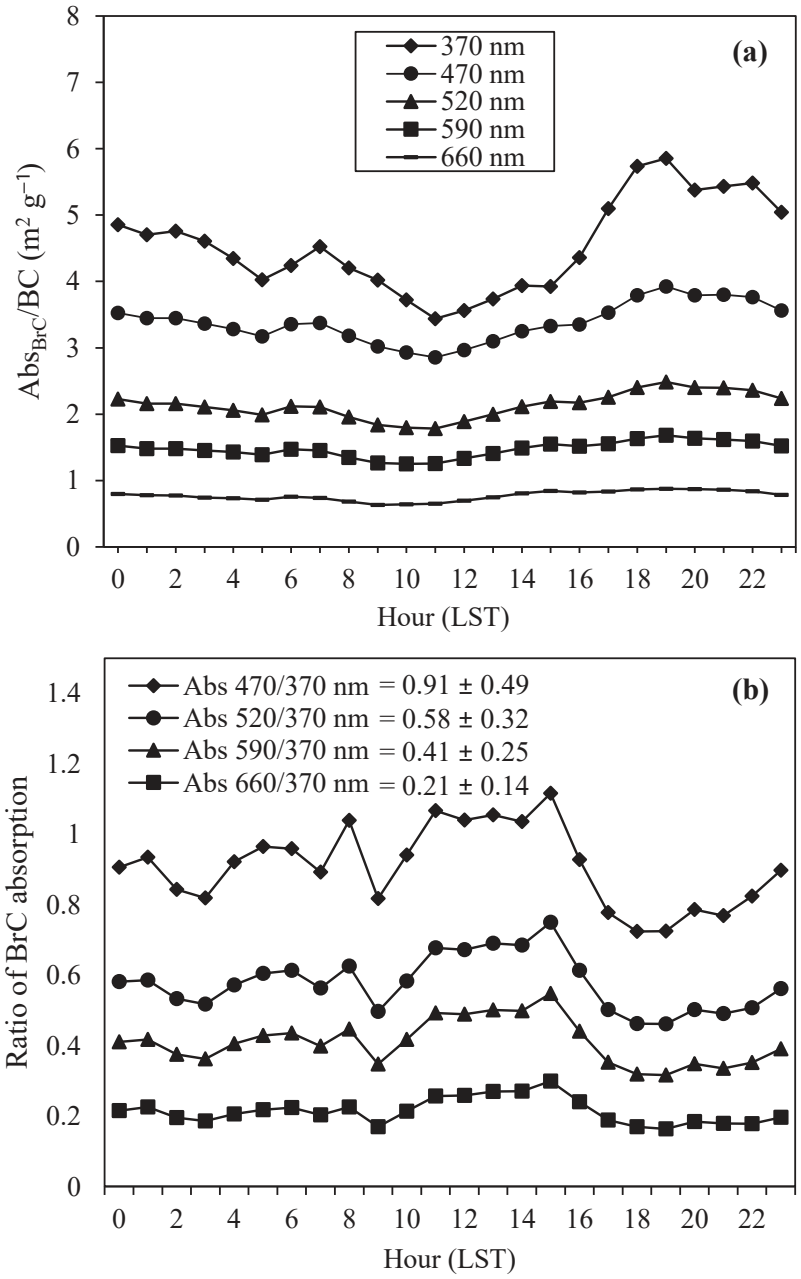

Fig. 5.10 Winter mean diurnal patterns of (a) the ratio between the B_rC absorption at different wavelengths and the BC mass and (b) the ratios of B_rC absorption between different wavelengths and 370 nm.

Another significant point on the distinction between $b_{abs\_B_rC}$ and b_{abs_BC} absorption constituents is the dust involvement on total b_{abs} at a shorter wavelength, which can cause overestimation of BB% on dusty days (Liakakou et al., 2020). Zhao et al. (2019) utilized iron (Fe) content and MAC values as well for dust samples to evaluate its influence on entire b_{abs} at a remote place in the Tibetan plateau, resulting in a yearly input of ~4% and ~9% at 808 nm and 405 nm, separately. Another study conducted in Athens revealed an insignificant influence of dust on spectral absorption and scattering properties (Katsanos et al., 2019). Similarly, by considering 166 days with dust events for four years data in Athens, Liakakou et al. (2020) found that the dust events disturb the estimations of B_rC absorption by ~4%, which are inside the uncertainties of the approximation method (Qin et al., 2018). In this study, dust contribution is assumed to be negligible because Guwahati is situated in the rocky foundation, and the site experiences no dust events in the entire sampling campaign.

Strong negative and statistically significant correlations ($R^2 = 0.80$) are found between the computed $AAE_{370\text{-}880}$ values and the estimated BC_{FF}/BC_{BB} ratio at 880 nm (Fig. 5.11). This proves the satisfactory performance of the Aethalometer model and the accurate assumption of the AAE_{FF} and AAE_{BB} values for quantifying the BC_{FF} and BC_{BB} components. The more significant slope (–16.3) indicates more sensitivity of the BC_{FF}/BC_{BB} ratio to longer wavelengths (880 and 970 nm) than shorter wavelengths (370 to 660 nm), which seems to be more appropriate for detecting the changes in BC_{FF}/BC_{BB} ratios and for BC source apportionment studies.It is noteworthy that for $AAE_{370\text{-}880} > 1.5$, the BC_{FF}/BC_{BB} ratio tends to zero (Fig. 5.12), implying that the AAE_{BB} as 1.7 used in this study corresponds to nearly pure contribution from open burning of biomass in this BRV region. Similarly, for $AAE_{370\text{-}880} < 1.1$, the BC_{FF}/BC_{BB} ratio becomes above 7.0, suggesting a clear dominance of fossil fuel combustion. Hence, the AAE_{FF} as 1.0 is considered suitable for quantifying BC_{FF} components.

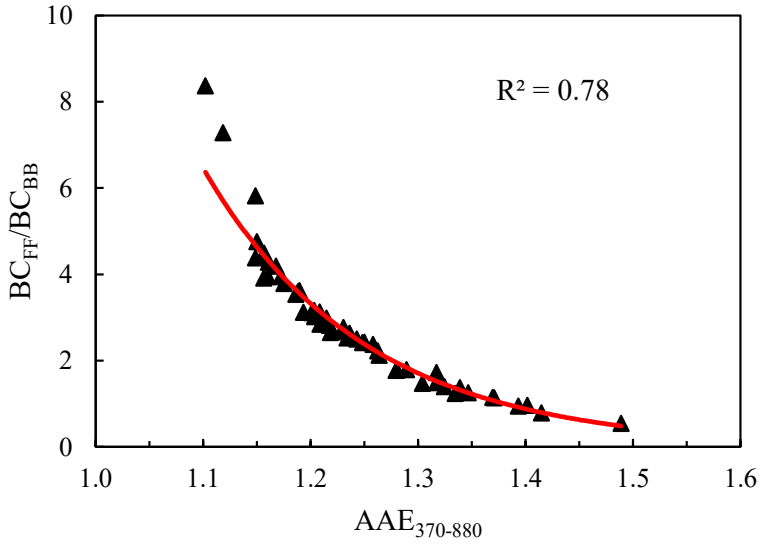

Fig. 5.11 Correlation between $AAE_{370\text{-}880}$ and BC_{FF}/BC_{BB} at 880 nm.

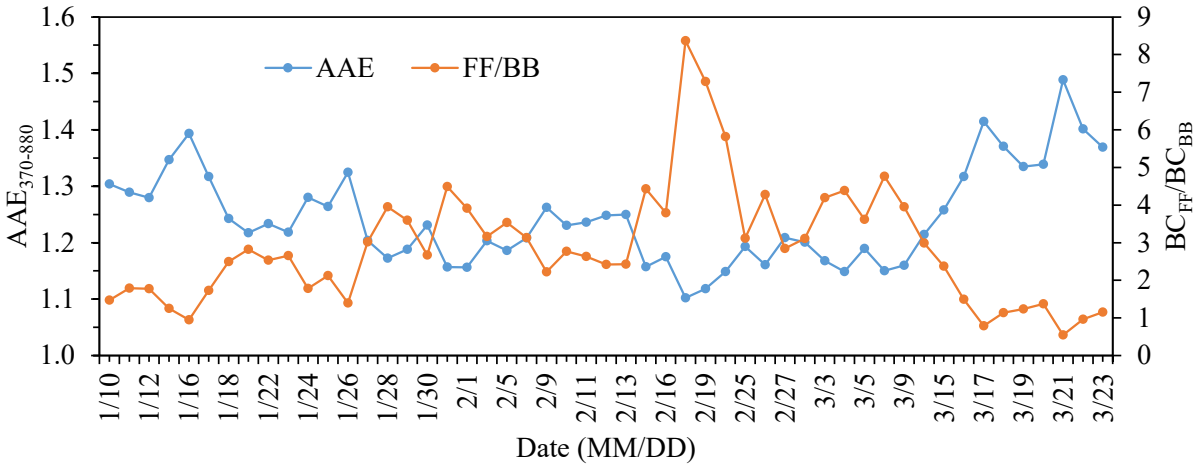

Fig. 5.12 Daily variation of the $AAE_{370\text{-}880}$ and BC_{FF}/BC_{BB} ratio at 880 nm.

5.6 Air quality modelling of traffic-derived Black Carbon

5.6.1 General

The AERMOD model is utilized to combine the BC emissions originated from moving traffic as line source and parking lot as area source over the complex terrain using observational (at two locations) and WRF-processed meteorology for the winter period. The AERMOD model is also evaluated against the observational BC concentrations in two topographical areas during winter and applied to study the reduction in BC concentrations due to implementation of emission norms BS-IV (equivalent to Euro 4) and BS-VI (equivalent to Euro 6). Field validation was also performed between the modelled data from AERMOD and observed data from AE-33 using statistical parameters.

5.6.2 Data preparation for modelling

5.6.2.1 Traffic characteristics

Variation in the daily vehicular count was observed at two geographical locations (L1 and L2), suggesting that varying emission rates should be used instead of static values. The average class-wise traffic contribution at L1 and L2 locations is shown in Fig. 5.13a-b. The L2 location had the highest daily-average traffic volume, much higher than L1 (Fig. 5.14a-b). However, during weekend days at the L1, more traffic was seen.

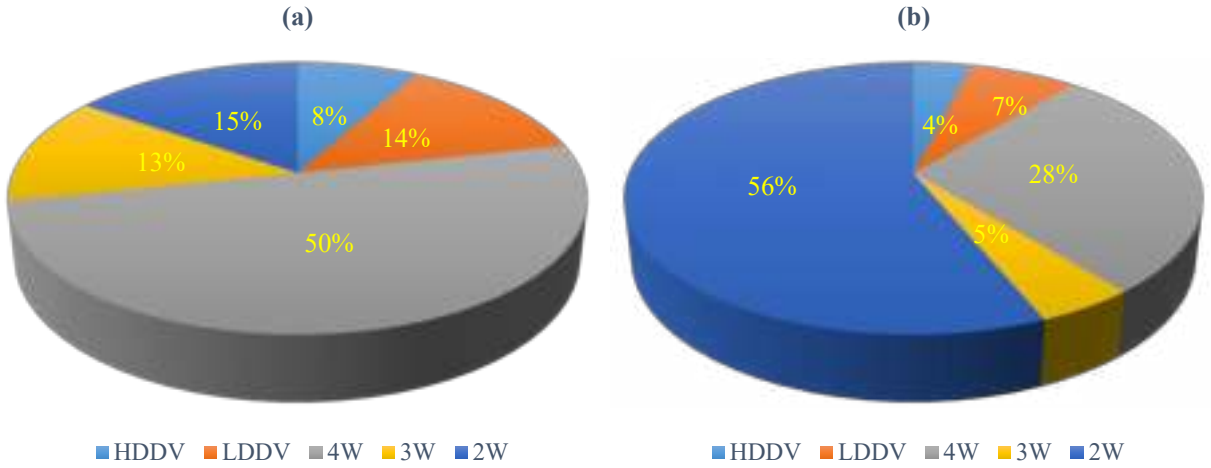

Fig. 5.13 Class-wise proportion of on-road vehicles at L1 (a) and L2 (b) locations.

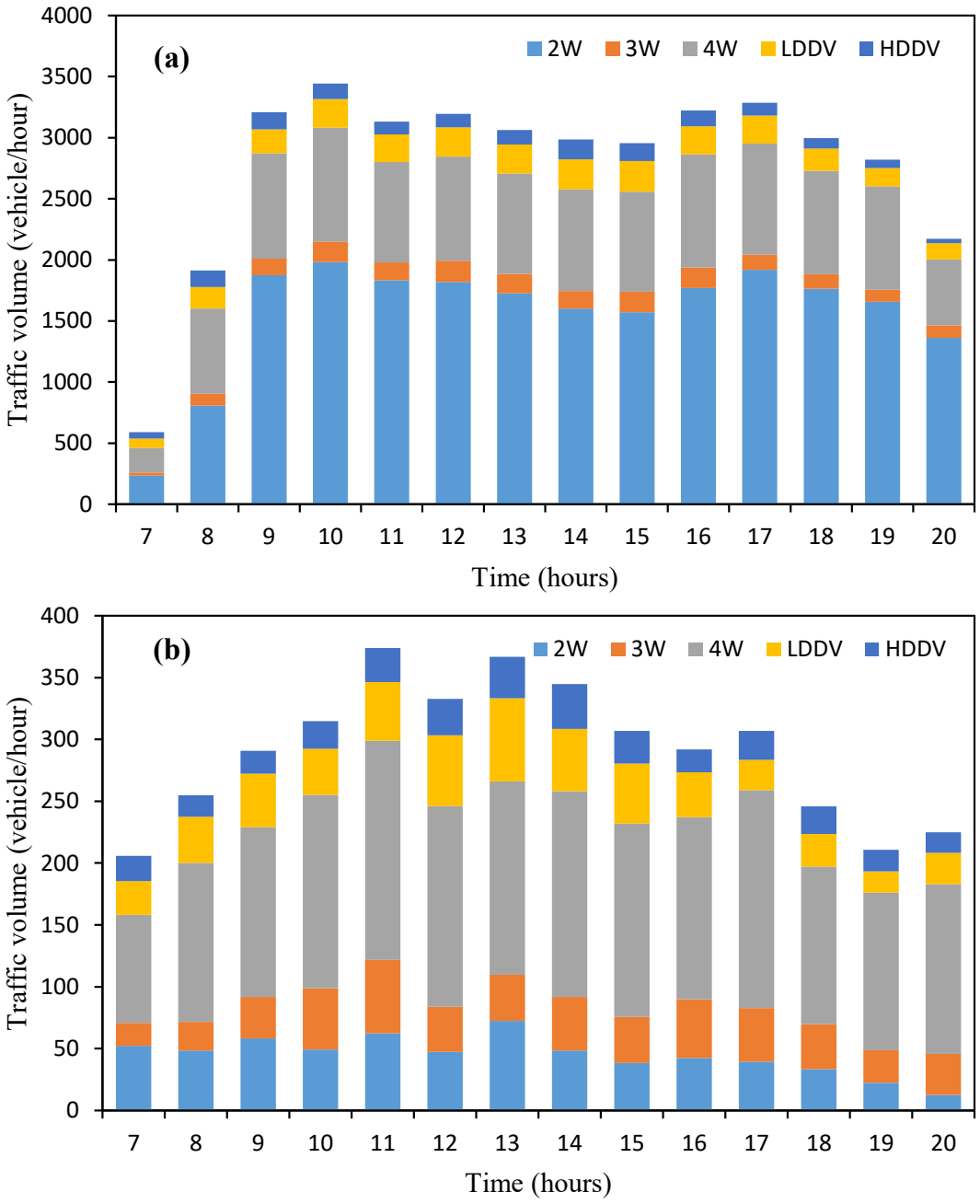

Fig. 5.14 Hourly traffic volume at (a) L1 and (b) L2 for the winter season.

5.6.2.2 *Traffic derived Black Carbon vs. ambient $PM_{2.5}$*

Fig. 5.15a presents the diurnal variation of the observed BC_{FF} concentration estimated by the Aethalometer model using an improved method. The daily mean observed BC_{FF} mass concentration ranged from 3.11 to 16.29 $\mu g\ m^{-3}$ (mean: 7.09 ± 2.62 $\mu g\ m^{-3}$). BC_{FF} concentration was peaked during morning rush hour (09:00 LST), and the lowest was observed in the late afternoon (15:00 LST). It might be attributed to the local emissions and hilly topography. Fig. 5.15b displays the daily diurnal variation of $PM_{2.5}$ and the fraction of fossil fuel associated BC in $PM_{2.5}$ during the study period. The weighted fraction of BC_{FF} in $PM_{2.5}$ varied from 0.06 to 0.20 (maxima). It should be noted that the daily (24 hr) mean BC_{FF} and $PM_{2.5}$ mass concentrations were used to estimate the fraction of BC_{FF} in $PM_{2.5}$.

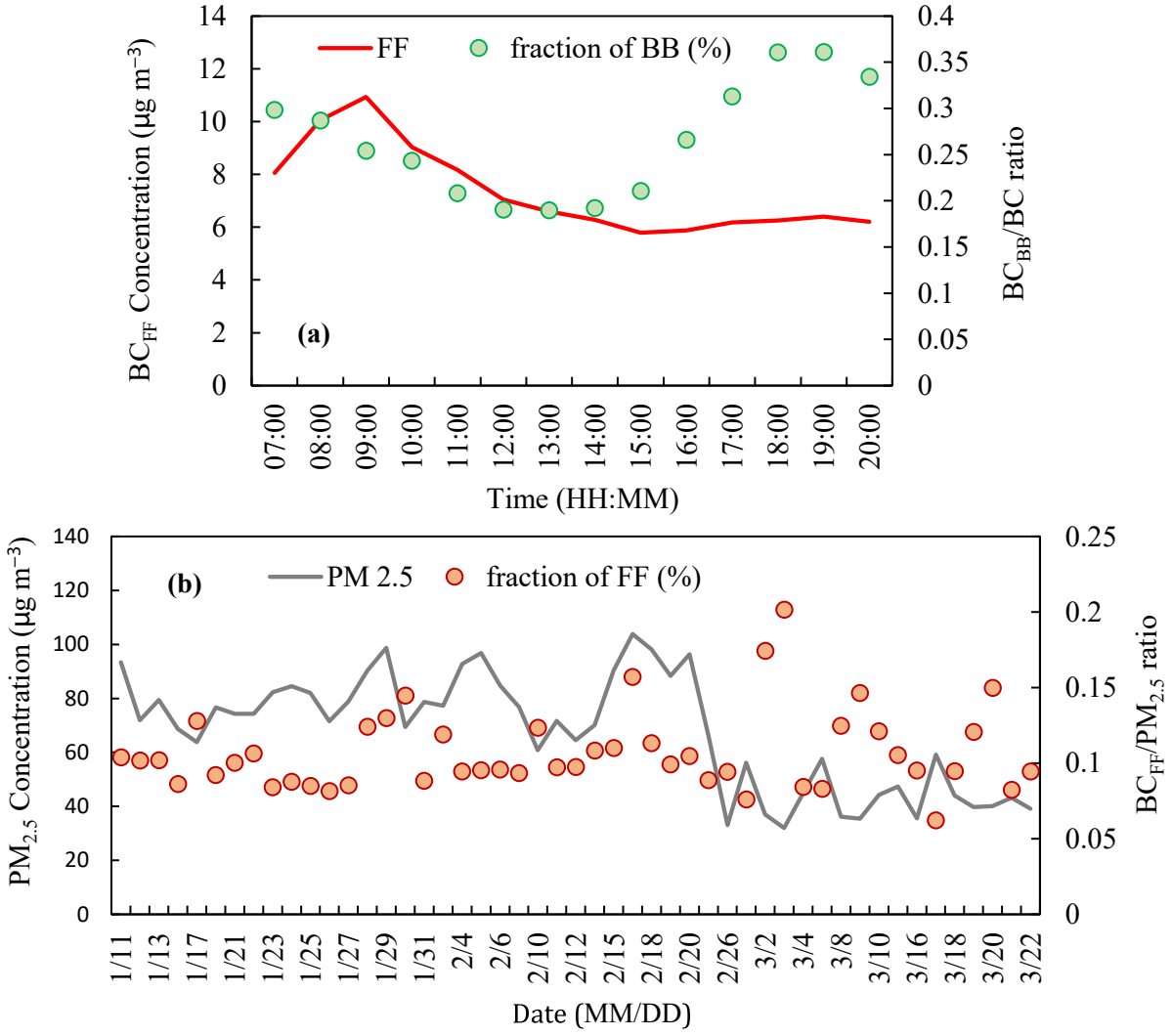

Fig. 5.15 Diurnal variation of the (a) BC_{FF} mass concentration and the fraction of biomass burning in total Black Carbon, and (b) $PM_{2.5}$ concentrations and the fraction of fossil fuel associated Black Carbon in $PM_{2.5}$ for the winter season.

5.6.2.3 Wind flow pattern

Fig. 5.16 shows the wind rose plots for the monitored days. The weather stations denoted as WS1 and WS2 were located within 2 km and 7 km. As observed, the prevailing wind at WS1 and WS2 was from the southeast and east direction, respectively. However, the WRF modelled wind rose diagram shows the south and east direction. A calm condition is the state of meteorology when wind speed is below a threshold limit of 0.5 m s^{-1} (Jeong et al., 2013). The calm conditions were observed as about 80%, 18%, and 7% at WS1, WS2, and for WRF modelled data, respectively, during the winter season. The wind flow pattern helps in the lateral dispersion of pollutants. At WS1, it is mostly under calm conditions. It is expected that the distribution of pollutants will be lower. Fig. 5.17 shows the variation in temperature recorded near the study location (WS1) and processed by the WRF model.

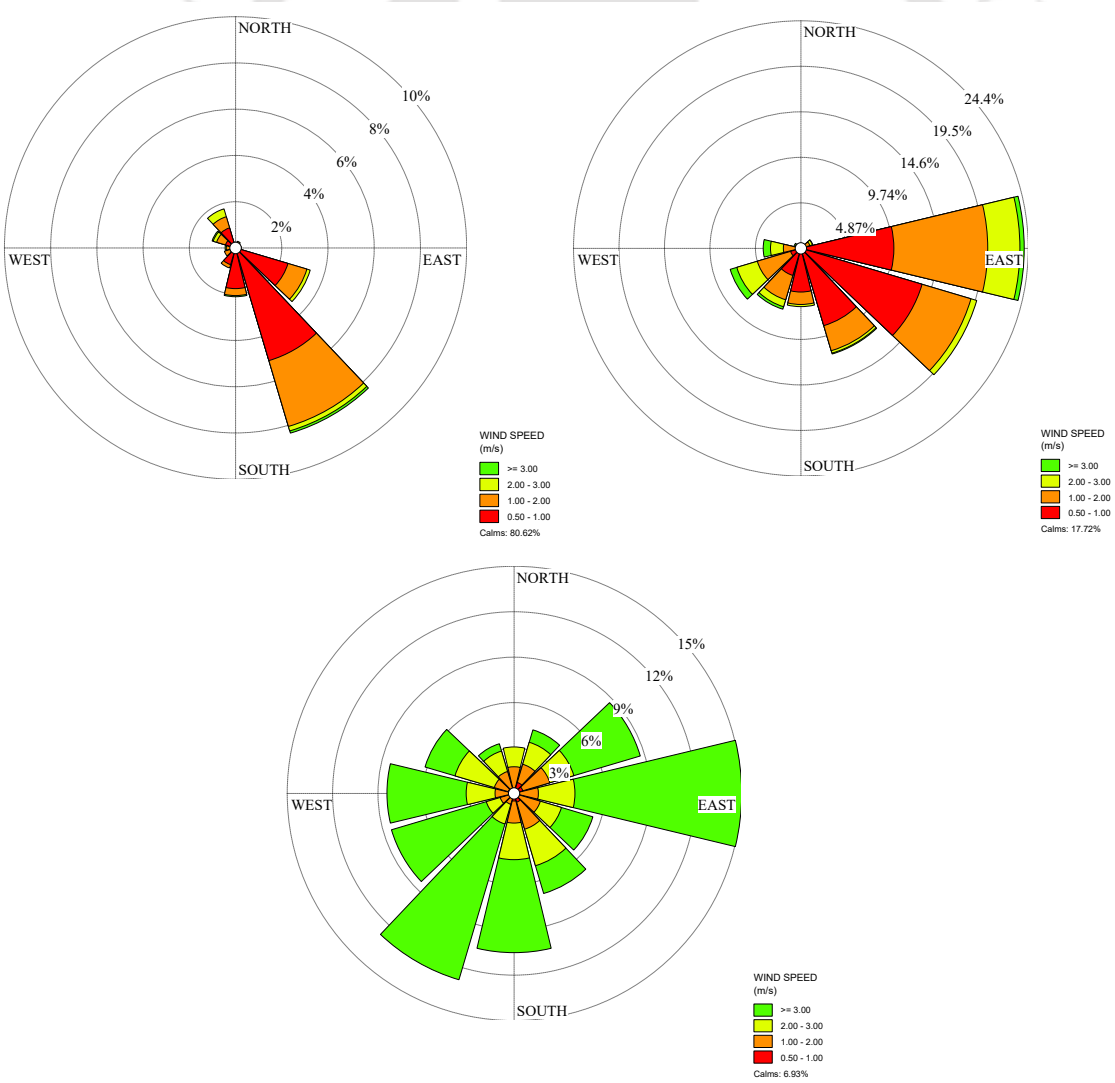

Fig. 5.16 Wind roses based on the measurements at IIT Guwahati, PCB Assam, and the WRF-modelled wind field for the winter period.

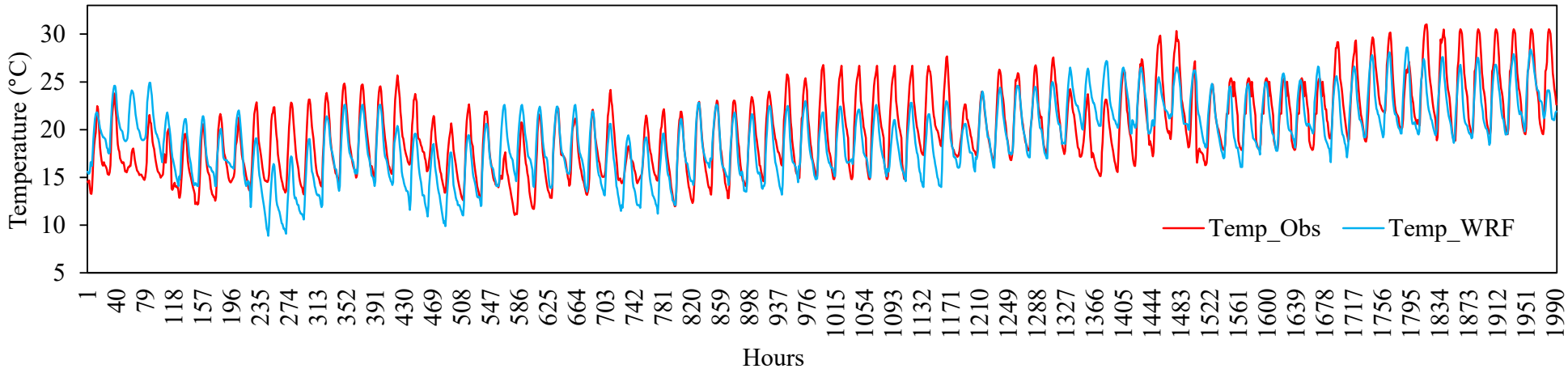

Fig. 5.17 Variation in temperature recorded near monitoring location and WRF processed records.

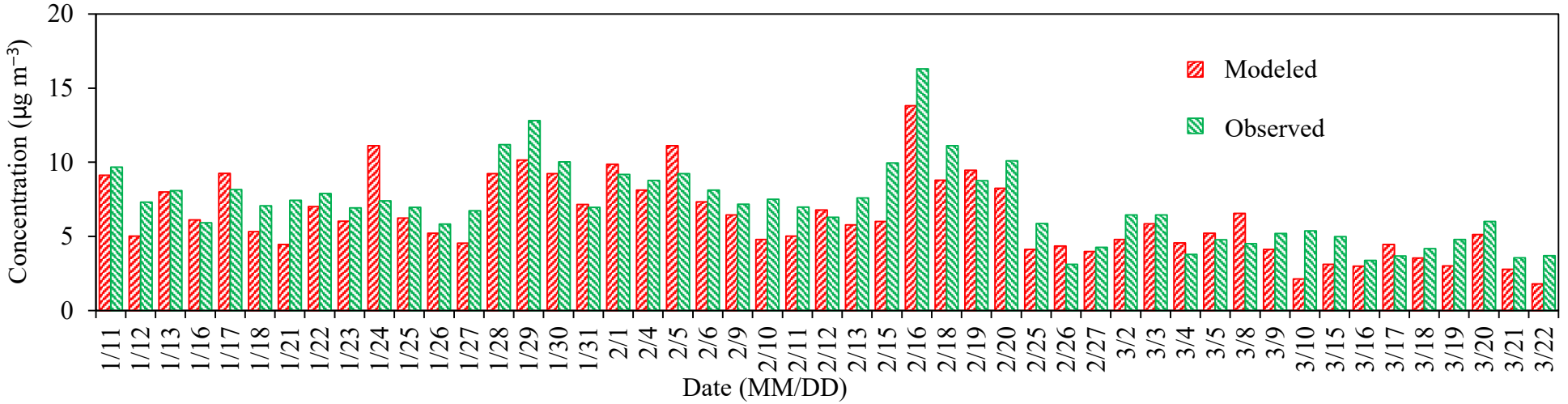

Fig. 5.18 The comparison of day to day observed BC_{FF} concentrations by Aethalometer and modelled by AERMOD at location L1.

5.6.3 Comparison of modelled and observed traffic-derived Black Carbon concentrations

Fig. 5.18 compares the observed and the modelled concentrations at the L1 location during the study period. It can be observed that the modelled BC_{FF} concentrations by AERMOD are less than the observed ambient BC_{FF} concentrations obtained from the Aethalometer model. The AERMOD model underestimated the BC_{FF} concentrations by ~12% and better simulated the higher values. For modelling purposes, the vehicular activity in the proximity is only considered. However, other combustion sources might influence the observations at the monitoring station. The modelled average BC_{FF} concentration in winter was 6.27 ± 2.61 $\mu g\ m^{-3}$, and the average observed BC_{FF} concentration was 7.09 ± 2.62 $\mu g\ m^{-3}$. The R^2 value was 0.70 (Fig. 5.19).

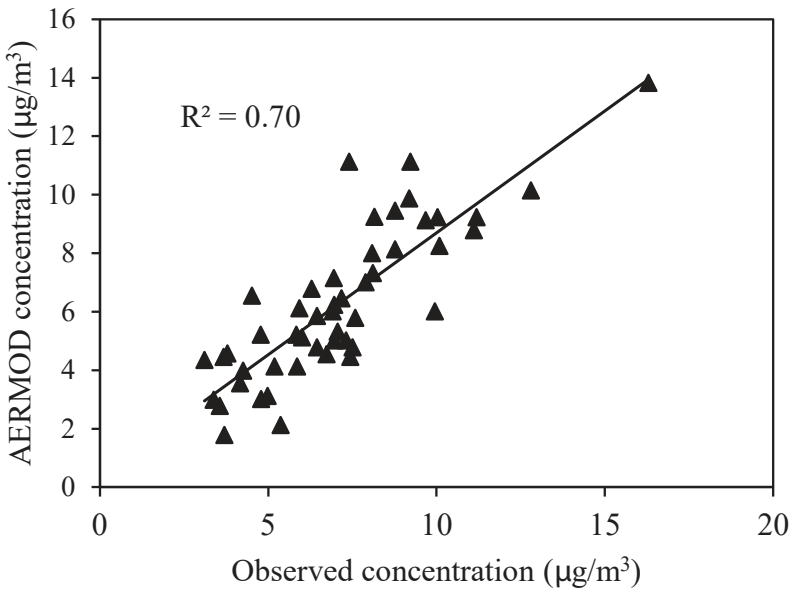

Fig. 5.19 Correlation between AERMOD modelled and Aethalometer observed BC_{FF} concentrations.

5.6.4 Performance evaluation of model

The performance of the AERMOD model was quantitatively validated by comparing it with the daily observed BC_{FF} concentrations using statistical parameters (Table 3.4). We observed good overall agreement between the different methods. It can be observed that the model satisfies the statistical requirements (FB = 0.1227, NMSE = 0.0642, and GMB = 1.1584, GV=1.0937, R = 0.828, FAC2 = 1.5022). The winter model (targeted only winter season) produced significant prediction accuracy $R^2_{CV} = 0.6119$. Michanowicz et al. (2016) found the higher AERMOD model prediction accuracies by using cross-validated in summer (0.65) in comparison to winter (0.52) for $PM_{2.5}$ concentrations. The index of agreement value was 0.8873, which is within the range of recommended parameter value.

6

Impacts and Mitigations

Incidentally due to the COVID-19 lockdown imposed from 24th March, the measurements at Kamakhya hills were discontinued and continued at IIT Guwahati till May 2020. The BC concentration data have been analyzed separately for this period and all those necessary optical properties have also been studied. The lockdown period has given the opportunity to compare the BC levels before and during the lockdown in absence of anthropogenic activities in particular vehicular emissions. This analysis is valuable and would serve as base-study in the region on the source apportionment and optical properties. Given the significant biomass burning in particular in the winter season, the results have been analyzed to see how total or partial reduction of fossil fuel consumption has influenced the trend of BC at 880 nm.

6.1 Impacts of COVID-19 lockdown on Black Carbon

The time-based and daily variations in the BC_{880} mass concentrations are presented in Fig. 6.1 (a) and Fig. 6.1 (b-c), respectively. The BC_{880} concentration ranged from 1.57 to 15.60 $\mu g\ m^{-3}$, with a mean concentration of 5.75 ± 4.24 $\mu g\ m^{-3}$. The maximum concentration was in the Pre-LD and the minimum in LD4. The average BC_{880} concentrations during Pre-LD, LD1, LD2, LD3, LD4, and Post-LD were 9.29, 4.70, 3.41, 3.69, 2.94, and 6.56 $\mu g\ m^{-3}$, individually. The BC_{880} concentration during the Pre-LD period was comparable to the values reported at Delhi (Goel et al., 2021). However, during LD1, LD2, LD3, LD4, and Post-LD, the BC_{880} concentration reduced by ∼49%, ∼63%, ∼60%, ∼68%, and ∼29%, respectively. The anthropogenic activities such as public transportation and essential industries were relaxed in succeeding lockdowns (stage-wise). The stage-wise easing implemented in different lockdowns dominated the BC_{880} concentration from fossil fuel-associated emissions. Though,

after LD3, the BC_{880} concentrations declined due to rain events and the abundant WS (Fig. A.4). The rainy and windy May and June decreased the BC_{880} and PM concentrations. BC_{880} concentrations evening and morning peaks also significantly dropped (62% and 75%) to low (nearly 2 $\mu g\ m^{-3}$) during the LD period. After LD4, the evening and morning peaks again started recurring due to relaxation given in anthropogenic activities. However, in the Pre-LD and Post-LD periods, the strength of both evening and morning peaks was high up to ~14 $\mu g\ m^{-3}$ because of heavy vehicular activities and emissions.

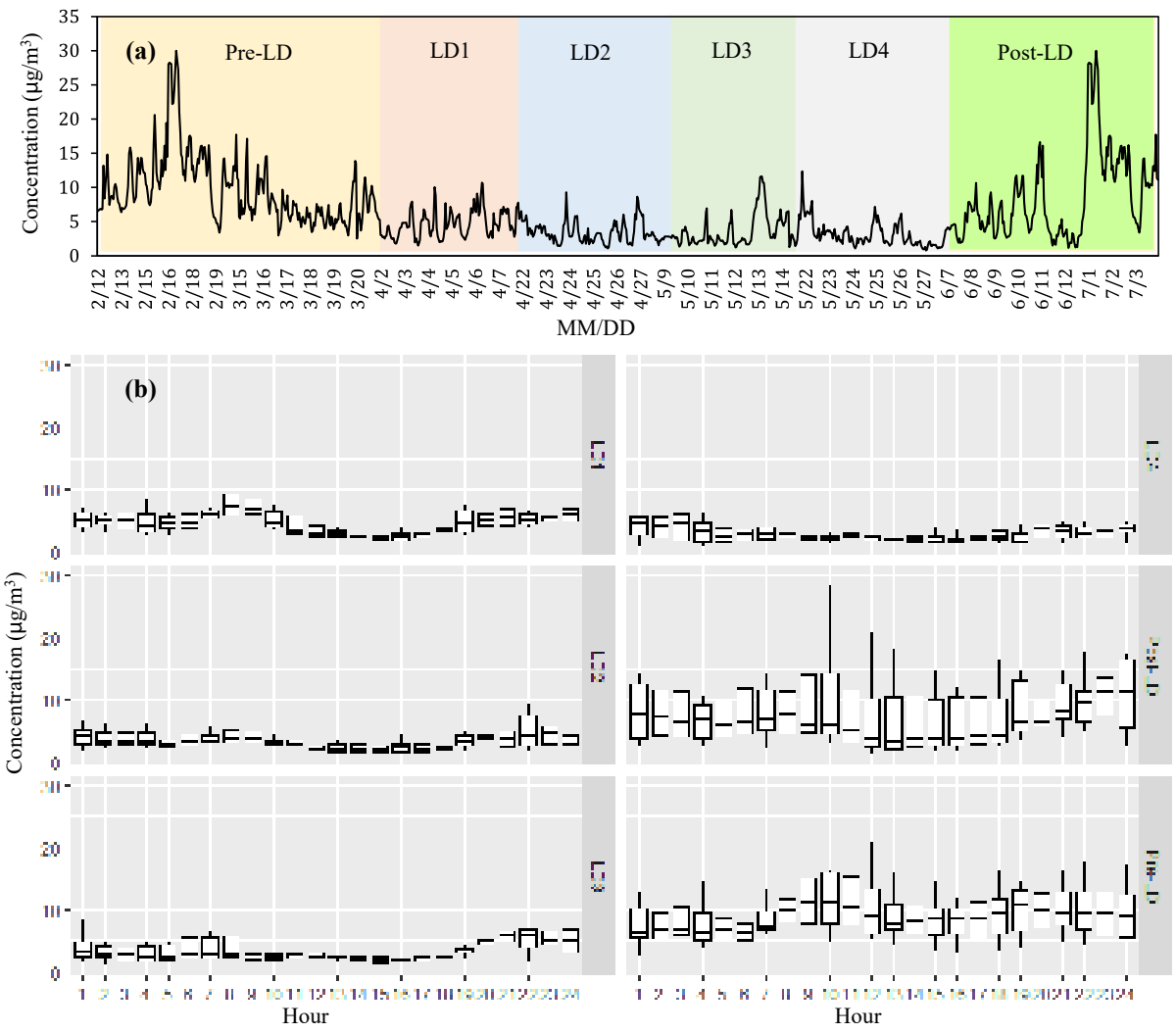

Fig. 6.1 Daily-averaged hourly BC_{880} mass concentration - each color represents different phases of lockdown (a) and Box plot of the diurnal variation of BC_{880} mass concentration (b) during the study period.

$AAE_{370-880}$ values were 1.01-1.66 (mean: 1.25 ± 0.08) (Fig. 6.2a), which is lesser than the AAE over Delhi during lockdown (1.32 ± 0.16) (Goel et al., 2021). The average $AAE_{370-880}$ during Pre-LD, LD1, LD2, LD3, LD4, and Post-LD were 1.19, 1.38, 1.33, 1.26, 1.21, and 1.20, respectively. The higher $AAE_{370-880}$ throughout LD1, LD2, and LD3 show the notable contributions from domestic cooking and fire events, and small $AAE_{370-880}$ during Pre-LD, LD4, and Post-LD indicate the most contribution from fossil fuel burning causes. The $AAE_{470-950}$ ranged from 1.05 to 1.59 (mean: 1.28 ± 0.06) (Fig. 6.2b). The average $AAE_{470-950}$ values during Pre-LD, LD1, LD2, LD3, LD4, and Post-LD were 1.23, 1.38, 1.33, 1.28, 1.26, and 1.23.

The segregation of two sources was done via 370-880 nm pair and estimated AAE_{FF} and AAE_{BB} of 1 and 1.7, respectively. Fig. 6.3a and Fig. 6.3b show the results. If AAE_{FF} as 1.0 and AAE_{BB} as 2.0 were applied, then fossil fuel and biomass burning fraction in BC_{880} in the six distinct phases of lockdowns are showed in Fig. A.5. The daily mean BC_{FF_880} concentration was wide-ranging from 1.21 to 11.30 $\mu g\ m^{-3}$, with a mean concentration of 4.13 ± 2.65 $\mu g\ m^{-3}$. The average BC_{FF_880} mass concentrations throughout Pre-LD, LD1, LD2, LD3, LD4, Post-LD were 7.28, 2.39, 1.94, 2.37, 2.14, 5.03 $\mu g\ m^{-3}$, respectively. The BC_{FF_880} mass concentration was maximum during Pre-LD and Post-LD. There were no constraints on industrial, vehicular, or additional anthropogenic activities. The BC_{FF_880} was reduced to 67% in LD1 and 74% in LD2. During the lockdowns, the movement of pooled vehicles was restricted except those for essential services such as doctors, police, and other essential commodities. The daily averaged BC_{BB_880} concentration wide-ranging from 0.37 to 4.30 $\mu g\ m^{-3}$, with a mean concentration of 1.63 ± 0.82 $\mu g\ m^{-3}$. The average BC_{BB_880} concentrations during Pre-LD, LD1, LD2, LD3, LD4, Post-LD were 2.00, 2.32, 1.47, 1.33, 0.80, and 1.53, respectively. The BC_{BB_880} concentration was great during LD1 and LD2 due to the forest fire events in the neighboring region. During LD4, a sudden decrease in BC_{BB_880} concentrations could be attributed to rain events and an increased proportion of vehicular emission, change in WD, and high wind speed. The influence of biomass and fossil fuel burning on the overall BC_{880} during Pre-LD, LD1, LD2, LD3, LD4, and post-LD are shown in Fig. 6.3b. The fraction of FF was high during Pre-LD, LD4, and Post-LD, i.e., 78%, 74%, and 76%, respectively.

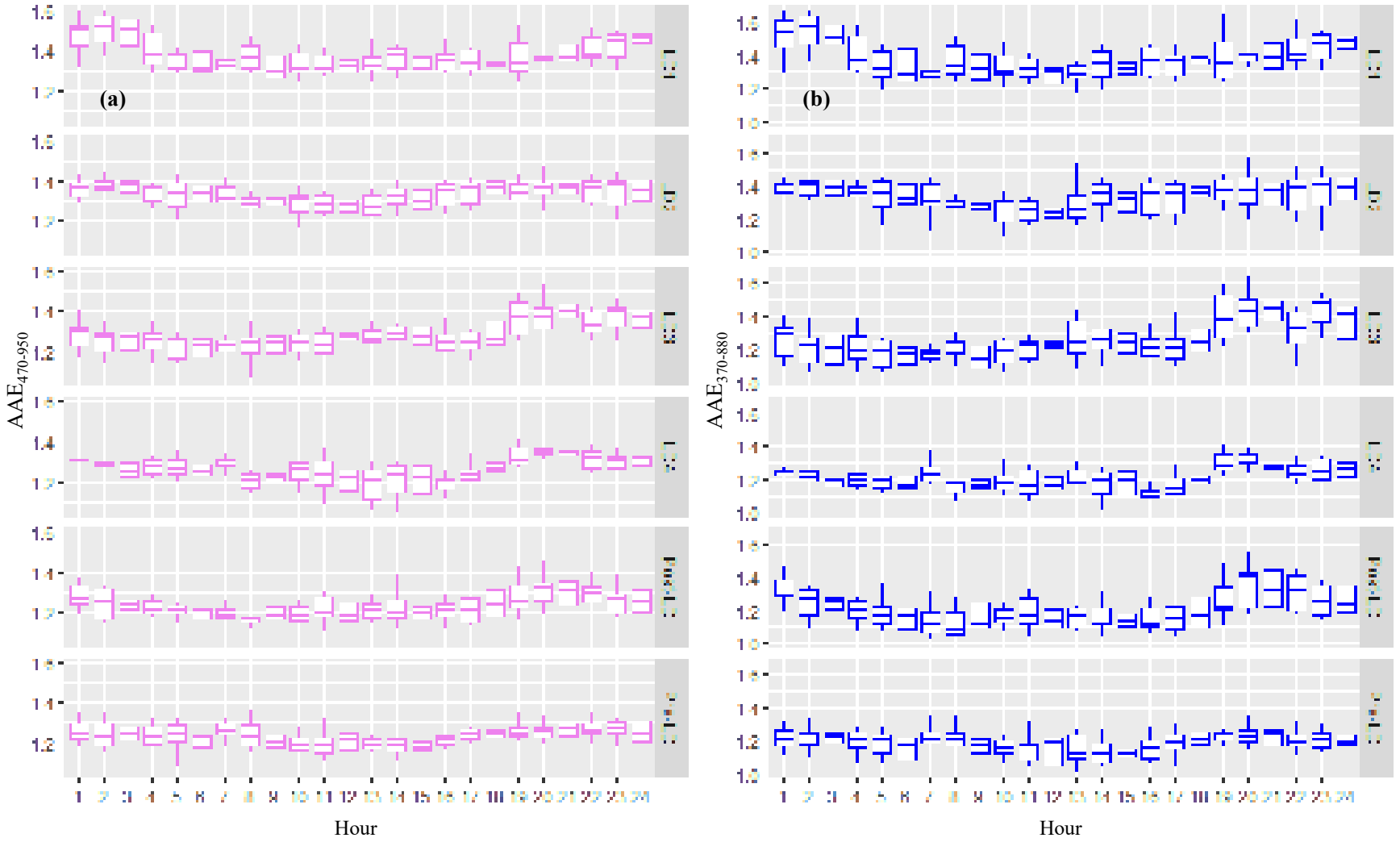

Fig. 6.2 Diurnal variation of $AAE_{470\text{-}950}$ (left), and $AAE_{370\text{-}880}$ (right).

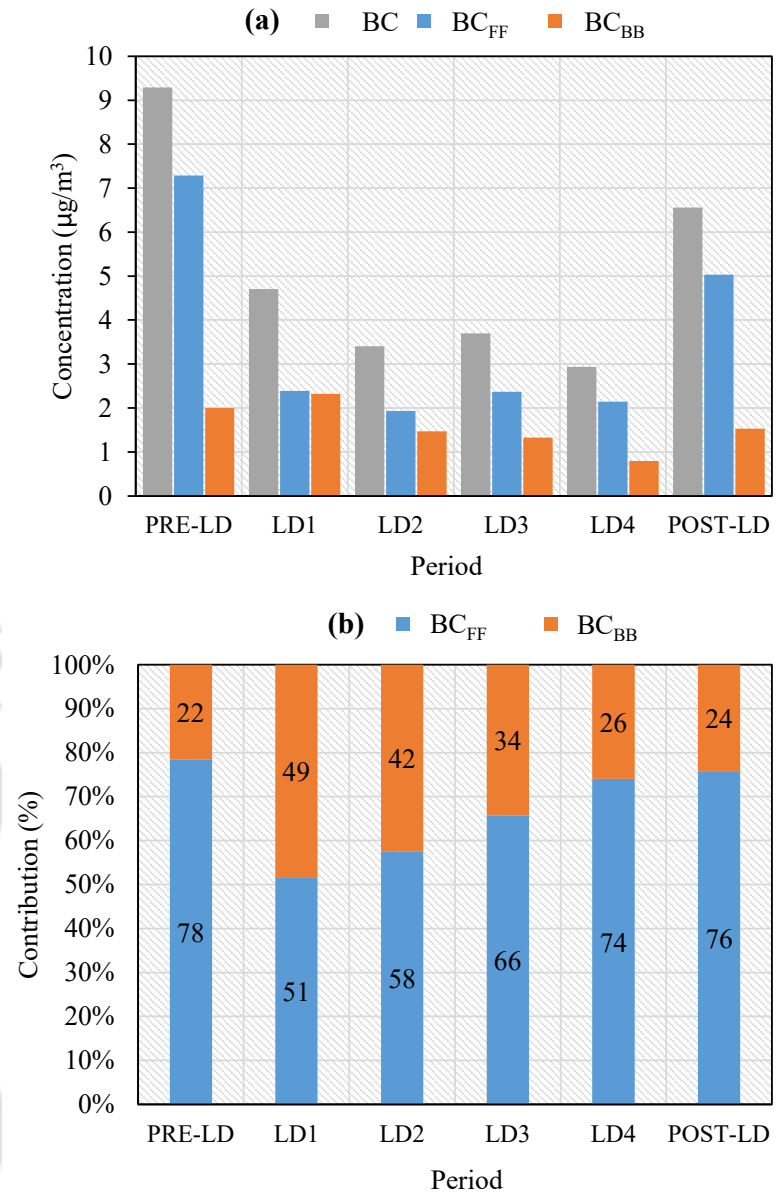

Fig. 6.3 (a) Concentration of BC_{880}, BC_{FF_880}, and BC_{BB_880}, and (b) contribution of the two sources to the total BC_{880} throughout lockdowns.

The large fraction of FF during Pre-LD is due to no limitation on anthropogenic activities such as industrial, vehicular, railway, etc. In Post-LD, the fraction of FF was similar to Pre-LD due to the easing given during this period. Diurnal variation in BC_{FF_880} and BC_{BB_880} concentrations are shown in Fig. 6.4a and Fig. 6.4b. High BC_{FF_880} mass concentration (12-18 $\mu g\ m^{-3}$) was detected during the morning rush hour (9:00-10:00 LST) during the Pre-LD period. In LD1 to LD4, morning and evening peaks (3-6 $\mu g\ m^{-3}$) were also witnessed, which could be due to the hospitals, Narayana Super Specialty and GNRC, located within a 1 km radius.

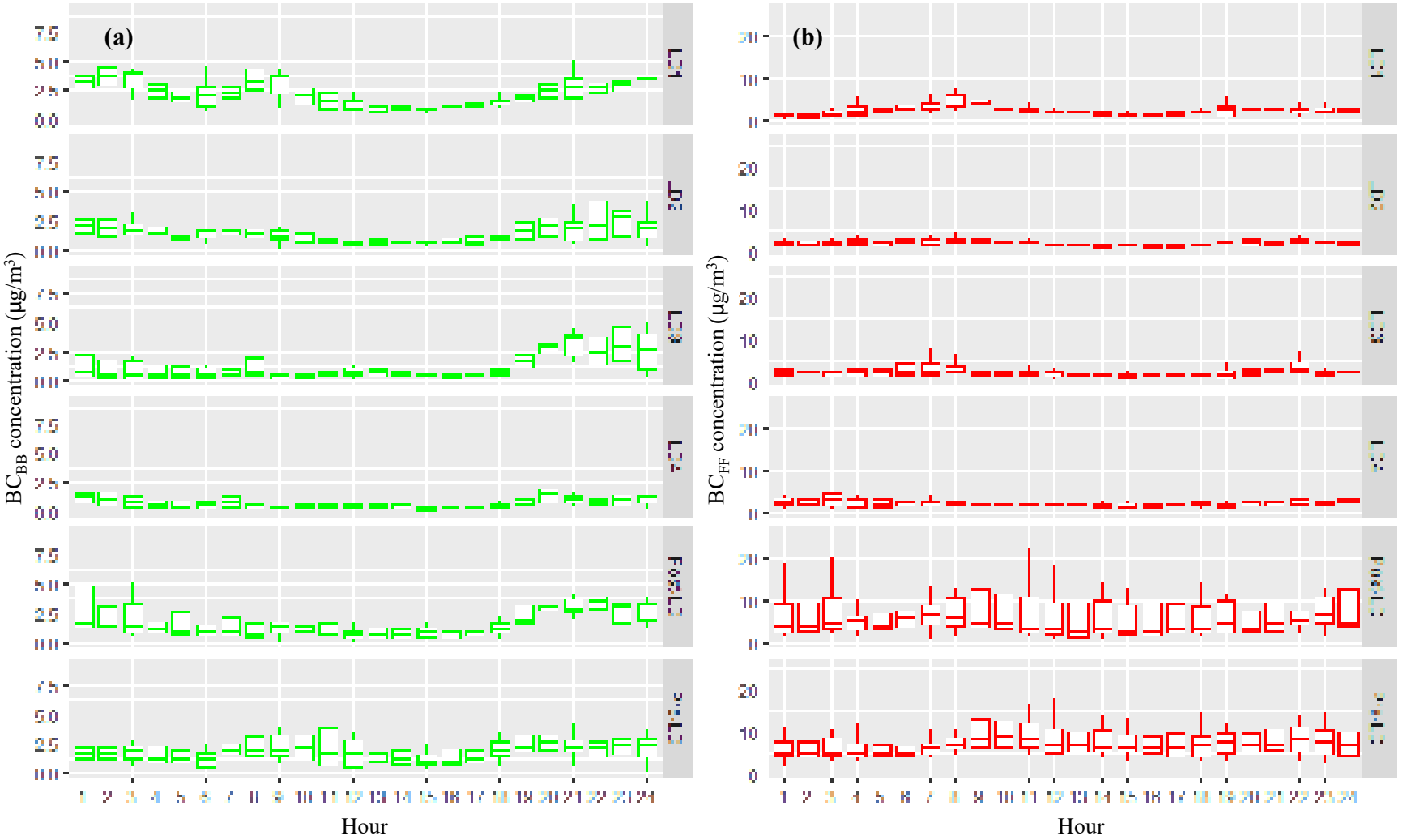

Fig. 6.4 Diurnal variation of BC_{BB_880} (left), and BC_{FF_880} (right).

In Post-LD, the Indian railway was not functioning, which subsequently directed to the growth of unattended vehicles. Moreover, Being the gateway to Northeast India, every vehicle passes through Guwahati city to other regions. From LD1 to Post-LD, an increasing FF fraction was observed due to easing in consecutive lockdown and unlock. The fire events might influence BB fraction, which was confirmed by the MODIS satellite retrieved fire data. In Northeast India, forest fires are significant biomass burning sources, as revealed in Fig. A.6. Though, a distinct drift was observed in the fraction of BB, which was highest during LD1 and lowest in Post-LD. The fraction of BB was large during LD1 and LD2 due to decreased vehicular emission in LD1 and increased fire events during LD2.

Variation in radiation effect during lockdowns is shown in Fig. 6.5. The average b_{abs} (370 nm) was 210.28 ± 88.25 Mm^{-1}, with 122.63 ± 28.39 Mm^{-1}, 85.60 ± 17.12 Mm^{-1}, 88.72 ± 39.23 Mm^{-1}, 66.57 ± 23.78 Mm^{-1}, 184.88 ± 111.73 Mm^{-1} Pre-LD, at LD1, at LD2, at LD3, at LD4, and Post-LD, separately (Table 6.1). The b_{abs_370} was higher than in Chongqing, China (113 ± 31.4 Mm^{-1}) during the COVID-19 epidemic (Chen et al., 2020). The average b_{abs} (at 880 nm) was 75.40 ± 31.98 Mm^{-1}, 36.54 ± 7.41 Mm^{-1}, 26.46 ± 4.34 Mm^{-1}, 28.70 ± 11.65 Mm^{-1}, 22.81 ± 7.26 Mm^{-1}, and 65.64 ± 41.60 Mm^{-1} during Pre-LD, at LD1, at LD2, at LD3, at LD4 and at Post-LD, respectively (Table 6.1). Also, lockdown actions reduced b_{abs_880} and b_{abs_370} considerably to 72% and 69%, respectively, till LD4. Equally, BC and B_rC were the effective sunlight absorber at several wavelengths, while BC was dominant from 370 to 880 nm. The average b_{abs_BrC} (370 nm) was 30.94 ± 15.05 Mm^{-1}, 35.72 ± 12.06 Mm^{-1}, 22.67 ± 7.09 Mm^{-1}, 20.45 ± 11.90 Mm^{-1}, 12.30 ± 6.80 Mm^{-1}, 28.76 ± 15.67 Mm^{-1}, 26.15 ± 14.04 Mm^{-1}, respectively during different phases (Table 6.1). The attribution to B_rC and BC at various wavelengths amongst 370 nm and 880 nm is observed in figure 10. B_rC accounted for ∼15% of the overall b_{abs} at short wavelength (370 nm) earlier LD1, increased up to ∼30% during consecutive lockdowns, and then decreased to 16% during Post-LD. The portion of $b_{abs\_BrC\_370}$ was considerably lower than in Chongqing (during lockdown) and Guangzhou (in winter) in China (Qin et al., 2018; Chen et al., 2020).

The effect of the lockdowns and their related levels of BC has been assessed to conclude the link between the concentration of BC and emission sources. Therefore, various phases of lockdowns have been selected purposively. This analysis revealed a substantial reduction in BC_{BB_880}, BC_{FF_880}, total BC_{880} over BRV, and significant changes in aerosol absorption coefficients due to the proportion of Black and Brown Carbons. And therefore, the imposing lockdown helped lessen coronavirus spread and improved the region's air quality significantly. The results may be helpful as baseline data to study the impacts of sources on the contribution to atmospheric BC and mitigations strategies.

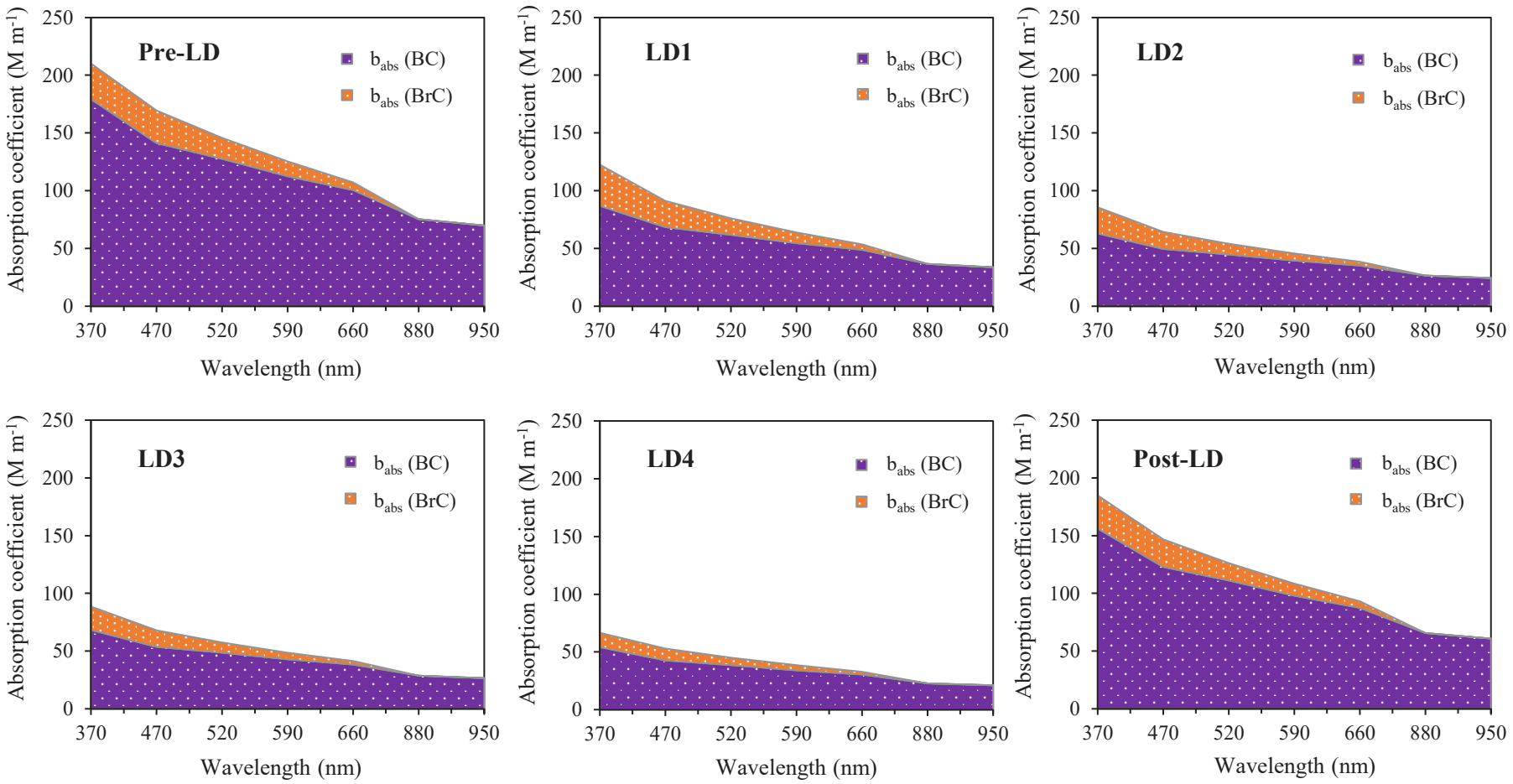

Fig. 6.5 Radiation effect of Black Carbon and Brown Carbon for the 370-950 nm in the different lockdowns.

Table 6.1 Summary of the parameters during COVID-19 lockdown. The values indicate the daily-averaged mean value ± standard deviation.

Parameters	Pre-LD	LD1	LD2	LD3	LD4	Post-LD	Overall
BC_{880} ($\mu g\ m^{-3}$)	9.29 ± 4.11	4.70 ± 0.95	3.41 ± 0.56	3.69 ± 1.50	2.94 ± 0.93	6.56 ± 5.35	5.75 ± 4.24
BC_{FF_880} ($\mu g\ m^{-3}$)	7.28 ± 3.41	2.39 ± 0.54	1.94 ± 0.21	2.37 ± 0.79	2.14 ± 0.54	5.03 ± 4.59	4.13 ± 2.65
BC_{BB_880} ($\mu g\ m^{-3}$)	2.00 ± 0.97	2.32 ± 0.78	1.47 ± 0.46	1.33 ± 0.77	0.80 ± 0.44	1.53 ± 1.01	1.63 ± 0.82
Fraction of FF (%)	78 ± 10	51 ± 18	58 ± 15	66 ± 18	74 ± 11	76 ± 15	70 ± 12
Fraction of BB (%)	22 ± 6	49 ± 11	42 ± 9	34 ± 11	26 ± 7	24 ± 9	30 ± 12
b_{abs_370} (Mm^{-1})	210.28 ± 88.25	122.63 ± 28.39	85.60 ± 17.12	88.72 ± 39.23	66.56 ± 23.78	184.88 ± 111.73	141.52 ± 88.74
b_{abs_880} (Mm^{-1})	75.40 ± 31.98	36.54 ± 7.41	26.46 ± 4.34	28.70 ± 11.65	22.81 ± 7.26	65.64 ± 41.60	48.51 ± 32.96
$b_{abs\_370\_BC}$ (Mm^{-1})	179.33 ± 76.07	86.92 ± 17.64	62.94 ± 10.32	68.28 ± 27.71	54.27 ± 17.27	156.13 ± 98.94	115.37 ± 78.41
$b_{abs\_370\_BrC}$ (Mm^{-1})	30.94 ± 15.05	35.72 ± 12.06	22.67 ± 7.09	20.45 ± 11.90	12.30 ± 6.80	28.76 ± 15.67	26.15 ± 14.04
$AAE_{370\text{-}880}$	1.19 ± 0.05	1.38 ± 0.06	1.33 ± 0.05	1.26 ± 0.07	1.21 ± 0.03	1.20 ± 0.05	1.25 ± 0.08
$AAE_{470\text{-}950}$	1.23 ± 0.03	1.38 ± 0.04	1.33 ± 0.03	1.28 ± 0.04	1.26 ± 0.02	1.23 ± 0.02	1.28 ± 0.06
T (°C)	20.57 ± 1.03	21.86 ± 1.64	23.59 ± 0.88	22.80 ± 1.94	25.02 ± 1.17	26.94 ± 1.44	23.31 ± 2.66
RH (%)	81.35 ± 6.17	77.87 ± 7.03	75.84 ± 4.00	82.19 ± 16.20	85.83 ± 2.28	80.34 ± 6.20	80.66 ± 7.92
WS (m/s)	0.99 ± 0.36	1.91 ± 1.21	2.38 ± 0.61	2.11 ± 0.63	1.79 ± 0.25	1.62 ± 0.31	1.69 ± 0.77
WD (0-360°)	190.60 ± 58.58	141.41 ± 17.34	134.32 ± 27.41	139.65 ± 45.07	108.92 ± 54.85	65.76 ± 10.01	142.37 ± 57.07
P (mbar)	757.73 ± 1.21	755.11 ± 0.59	755.88 ± 1.06	754.53 ± 1.20	754.51 ± 1.33	752.18 ± 0.58	755.17 ± 2.18
SR ($W\ m^{-2}$)*	120.45 ± 34.99	160.00 ± 14.74	149.21 ± 28.83	144.54 ± 44.68	173.78 ± 36.82	176.52 ± 52.56	151.09 ± 42.24

*seven sunshine hours averaged value.

6.2 Impact of hilly terrain

The winter averaged BC_{FF} contour is displayed in Fig. 6.6. The maximum BC_{FF} concentration for the winter period and the ninth hour was 18.5 $\mu g\ m^{-3}$ and 30.8 $\mu g\ m^{-3}$. Each contour comprises all receptors under the similar BC_{FF}. Consequently, from the contours different BC_{FF} dispersion distances can be determined in different directions. For BC_{FF} contours, very low BC_{FF} concentration limits (as small as 0.2 $\mu g\ m^{-3}$) were selected to plot BC_{FF} dispersion. Because average winter BC_{FF} above 0.9 $\mu g\ m^{-3}$ presented very short dispersion distances (<100 m) and even BC_{FF} of 0.2 $\mu g\ m^{-3}$ had an extreme spread of ~300 m. The farthest BC_{FF} dispersion occurred in the north, while it was the shortest in the east. This may be due to wind mostly blowing from the southwest, and the terrain in the west hinders the dispersion of BC_{FF}. The winter wind rose demonstrates that the main winds in the BRV region are from SE, and the wind speed is typically less than 1.5 m s^{-1}. Hence, BC_{FF} is getting accumulated in this region. While comparing the two traffic monitoring locations, the impact areas are evidently unlike, with the highest spreading influence area anticipated for the L2 location tailed by the L1 location primarily due to the difference in emission rates. Considering BC_{FF} of 0.2 $\mu g\ m^{-3}$, the maximum dispersal is up to 120 m for L1 and 50 m for L2 locations. As numerous factors affect BC_{FF} dispersal in the ambient environment, terrain coupled with meteorology produced reliable outcomes. The significantly higher emission rate and geographical region for the L2 site may be the primary purpose of clarifying its considerably greater impact region. The purpose of including two distinct geographical locations was to integrate considerable variability in aerosol BC sources that add to individual exposure in the BRV region.

The dispersion modelling using a Gaussian model, AERMOD revealed that the terrain facilitates the trapping of ambient BC concentrations, and their effects are limited to very few meters as per terrain elevations. Hilly terrain obstructs the winds and creates a vacuum on the other side of the hills, promoting BC accumulation causing high BC_{FF} concentrations. This accumulation of pollutants may increase personal exposure for those living in the BRV region. The variation in the spatial distribution was less on foggy days. The evaluation of AERMOD with the observed data demonstrated its predictive ability over complex terrain.

Above all, the WRF modelled-wind field delivered poorer quality dispersal approximations than using atmospheric observations from the locations positioned at 2 km ahead of the emission sources.

6.3 Emission reduction due to Bharat Stage norms: BS-IV and BS-VI

Two hypothetical scenarios were tested following BS-IV and BS-VI emission standards with all vehicles. Fig. 6.7a displays the application of the AERMOD model for the evaluation of BS-IV and BS-VI implementation. The results showed apparent reductions in BC_{FF} concentrations due to improved emission factors. It also shows the variation in emission rates according to the traffic volume and vehicle category at two locations, L1 and L2 (Fig. 6.7b-c). The decrease in the BC_{FF} concentrations for BS-IV and BS-VI were 35% and 75%, respectively.

Further, the vehicle-category-wise contributions to the BC_{FF} concentrations were estimated. It was found that 4W and 2W gasoline vehicles were the top contributors to the ambient BC_{FF} concentration despite significantly lower emission factors than diesel vehicles. The collective effect of large 2W and 4W vehicles was the significant share in ambient BC_{FF} concentration. The higher emission rates for HDDV vehicles account for their almost equal share compared to LDDV and 3W categories. The diesel-driven vehicles (3W, LDDV, and HDDV), with less traffic volume (than gasoline vehicles) and high emission factors, impacted BC_{FF} air quality. Therefore, the adoption of the emission norms by diesel vehicles may fetch immediate environmental benefits. Implementing the recommended BS-VI emission criteria will fundamentally bring Indian motor automobile guidelines into an alliance with European Union (EU) regulations for LDDV, 2W, and commercial vehicles, for example, buses and heavy-duty trucks. Four and two-wheelers had a high impact due to the high share in the traffic fleet, while 3W, LDDV, and HDDV had a high impact due to higher emissions rates. The various scenarios recreated using AERMOD model will help to make innovative and strategic mitigation policies for increasing traffic emissions and thereby helping to curb the BC emission eventually.

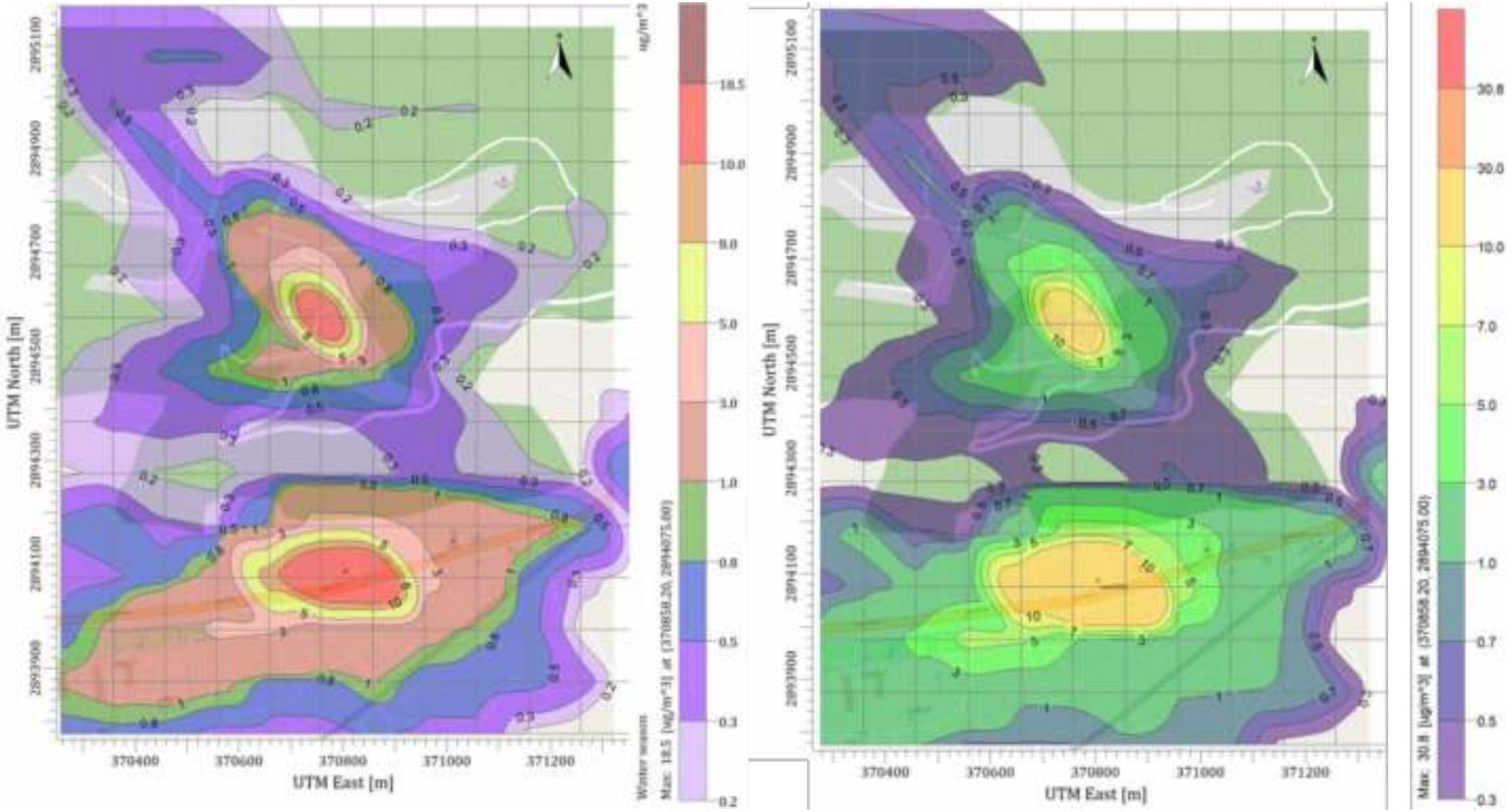

Fig. 6.6 Contour plots of Black Carbon mass concentration using AERMOD model (left) for the whole period and (right) for the 9th highest hour.

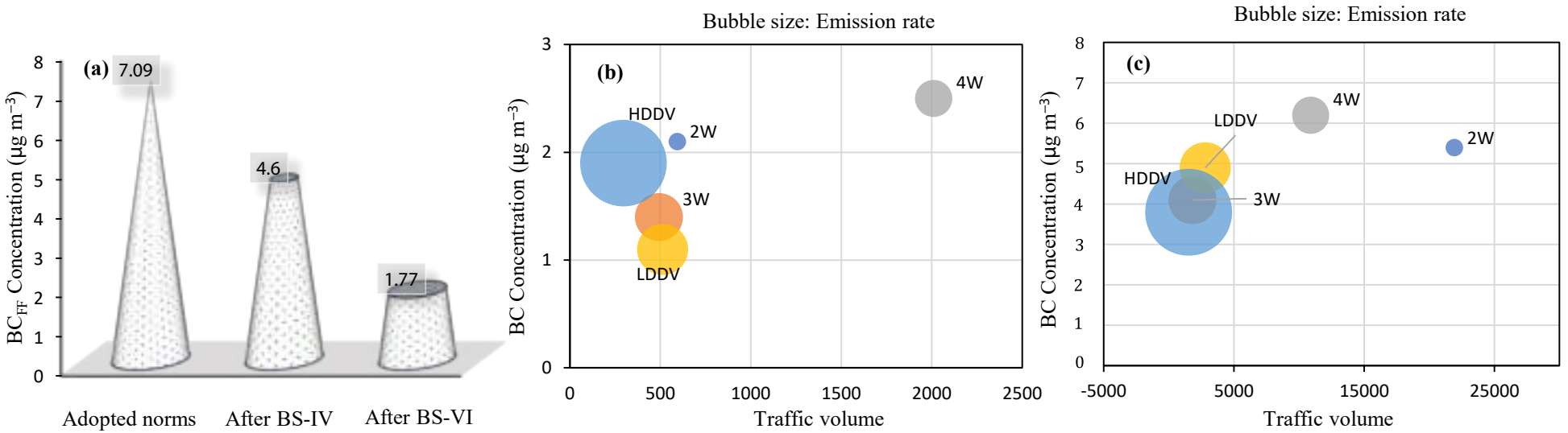

Fig. 6.7 (a) Evaluation of BS-IV and BS-VI standards implementation, Bubble plot showing class variations in emission rate, volume, and related BC_{FF} emission at (b) L1 and (c) L2 locations, respectively.

6.4 Mitigation measures

Reducing emissions from the transportation sector is a challenge as most sources are privately owned and not currently subject to any particular emission legislation. The Indian government has proposed the new emission norms in 2020. However, the vehicles plying on the roads of Guwahati are from various emission standards like BS-II, BS-III, and BS-IV in mixed proportion. Reducing emissions will be a relatively long-term process. It should involve changes in the performance and efficiency of future vehicles. The removal or up-gradation of older vehicles might help improve the situation. It can also be solved by installing the particle filters at the tailpipe of the heavy-duty diesel vehicles of older vehicles. Moreover, two-wheelers emit less pollution, but these are present in large numbers. It should not be ignored.

Thoroughly implementing the BS-VI standard can drastically reduce BC emissions from vehicular emissions. Promoting public transport that runs on electricity can decrease private vehciles (LMV) and two-wheelers. Moreover, promoting bicycles for short-distance commuting can be helpful. Implementing this will increase the cost of making pedestrian and bicycle lanes, but compared to positive outcomes, it is good. Another significant contributor to BC emissions is the open burning of biomass. The uncontrolled open burning of softwood, hardwood, papers, agricultural waste, etc., for cooking and heating purposes, especially in winter, is common in rural and suburban areas. Moreover, municipal solid waste containing a variety of rubbish (for e.g., plastic, water bottles, papers, and clothes) are burned by locals, which may lead to the increase in BC concentrations as a fugitive source. It can be reduced by public awareness and implementing alternatives.

6.5 Summary

In this study, the dispersion of traffic-derived BC emissions has been estimated using the AERMOD model and validated with the apportioned BC_{FF} concentrations by the Aethalometer model. On-site meteorological data produce more reliable dispersion calculations than WRF modelled data. Low wind with hill fog facilitated the rise of Black Carbon concentration in the hilly terrain. This study assumes that the differences between projected concentrations using AERMOD and experimental concentrations of BC are primarily due to undefined BC emissions. The technique presented can be used to evaluate the emission inventory containing both local and regional inventory. Modelled BC concentrations agreed with those estimated by the two-component mixing model. It indicates the modelled BC concentrations were reliable to evaluate the effect of the new emission standard proposed by the Indian government. The class-specific modelling revealed that the 4W and 2W categories were significant contributors due to their large proportion. The other HDDV, 3W, and LDDV vehicles also contributed to the BC concentrations due to their high emission rates. Therefore, it can be inferred that all the vehicular category significantly impacts BC in this region.

Further, the model was applied to investigate the reduction in BC concentrations for BS-IV and BS-VI emission standards over the adopted scenario. Results showed that implementing BS-VI would result in a much more drastic decrease in BC concentrations. It showed the need for the implementation of such stringent emission norms. Lastly, mitigation measures are suggested according to the results of this study and the current standards regulated by the Indian government.

In the present study, the AERMOD model was utilized for inverse modelling to conclude the BC_{FF} radiation strength and the effect of complex terrain on its dispersion for a region of Guwahati, India. The aim was to study source-meteorology-terrain interactions and their combined effects on BC dispersion using the AERMOD model. The impact of traffic on air quality was studied. This study was directed to validate if their concentrations at setback distances determined from the AERMOD model are impacting human health during long-term and short-term exposure. It is noteworthy that there are no regulations or rules on ambient air quality to control the BC concentration. WHO recommended BC concentration

limits of 20 $\mu g\ m^{-3}$ for annual BC. In the following discussion, all possible directions were considered. The aim was to quantify the winter influence and relate winter average BC_{FF} contours with dispersion happening frequency contours.

7

Findings and Conclusions

7.1 General summary

This study focused on the site-specific spectral properties obtained from the direct measurements of Black Carbon concentrations during winter in Guwahati to estimate primary and secondary components of Brown Carbons, light absorption, and source contributions. Source contributions of BC improved with site-specific Angstrom Absorption Exponent. BC concentrations were high during nighttime than daytime, with more influence (70%) from FF (diesel driven buses) in the morning hours and 30% contribution from BB in the evening and morning hours associated with the domestic biofuel for heating and cooking and open burning. Healy et al. (2017) reported the uncertainty in estimating BC and its fraction up to 30-35% by AE-33 Aethalometer. However, it would be much less in the present work due to site-specific properties. In addition, it was evident from the results that besides vehicular emissions, rampant burning of biomass (waste material and dry leaves and wood) for heating and cooking purposes contribute to Black and Brown Carbons significantly. The time-based characteristics of B_rC absorption were estimated using the field measurements and the B_rC_{sec} contribution to the total absorption using the empirical model. B_rC is the significant constituent of carbonaceous aerosols with significant radiation effects. For the first time, the AERMOD model was employed to study the dispersion of fossil-fuel-originated Black Carbon over hilly terrain. The novelty of this study is the development of the complete profile of light-absorbing carbonaceous aerosols, improved source apportionment using site-specific spectral properties, and the FF and BB contributions to BC, which are essential to developing appropriate policies for BC reduction.

The BC mass concentration at Guwahati from Jan-March 2020 has been investigated using an Aethalometer (AE-33) at the background site with the highest terrain suburban regions. The results revealed that controlled combustion of fossil fuel has higher annual contributions (ranging from 47-81%) than open burning of biomass (ranging from 19-53%) to the total mass concentration of BC at all sites. In comparison, the highest seasonal biomass contribution (30%) was observed in the winter at a background site surrounded by hills and valleys. The relative contribution of fossil fuel-associated BC (BC_{FF}) to the total BC was higher in the pre-monsoon. In contrast, biomass originated BC (BC_{BB}) was found to be contributing more in the winter season. The diurnal variation of BC_{FF} was observed to be cooperatively higher at the street canyon site during traffic rush hours, while BC_{BB} showed the highest contribution during late night and gradually decreased overnight and throughout the day. The sampling sites with more significant vehicular activities showed a strong seasonal dependence with BC concentrations due to the vicinity's fuel composition and combustion processes. The significant decrease in the values recorded during the COVID-19 lockdown period has been the result of no anthropogenic activities and not the effect of seasonal transformation. And therefore, the imposing lockdown helped lessen coronavirus spread and improved the region's air quality significantly.

The humid and calm windy meteorological conditions during January resulted in the highest $PM_{2.5}/PM_{10}$ indicating the decreased emissions of coarse particles from the Brahmaputra river valley (BRV), while the lowest $PM_{2.5}/PM_{10}$ (in March) showing the increased emissions of coarse particles from the arid BRV and long-range transport dust from north-western India. In contrast, the low $BC/PM_{2.5}$ in high pollution days indicates the dominance of biomass burring, while high $BC/PM_{2.5}$ in low pollution days suggests the dominance of vehicular emissions in BRV region, which are in agreement with the BC sources identified by the two component mixing model (AE33). The modelling results revealed that implementing the new emission norms (BS-VI) can drastically reduce this region's BC emissions from older vehicles. The findings of this study have implications in future policy making and implementation of strict regulations aiming to improve deteriorating air quality in the hilly regions of Guwahati.

7.2 General conclusions

1. The reapportionment of Black carbon from two sources were improved using site-specific spectral properties.
2. The results of this study can be generalized in the region of northeast India or a similar environment.
3. Hilly terrain facilitates the trapping of aerosols at lower altitudes and blocks the lateral diversion of the low-level wind flow.

7.3 Key findings

1. Fossil-fuel combustion contributed up to 90% to total Black Carbon, while biomass contributed up to 50% during COVID-19 lockdown.
2. The absorption of B_rC_{sec} at 370 nm was about 41-50% of the total B_rC absorption during winter, indicating the dominant role of secondary sources.
3. Black Carbon concentration decreased up to 68% during the different phases of lockdown. BC associated with fossil fuel was 51-78%, and biomass burning was 22-49%. The fraction of fossil fuel and biomass burning in the whole of BC fell to 0.73 and 0.65 during the lockdowns. Air quality improved by about 47-58% on the 4^{th} and 7^{th} day of lockdown.
4. The aerosol absorption coefficient declined by 69%, and AAE was reduced by 64% during lockdowns.
5. Source apportionment based on the site-specific properties (AAE) improved the contribution of two different sources (FF-70% and BB-30%) than the default Aethalometer model constants.
6. The COVID-19 lockdown reduced the Black Carbon concentrations to a significant level (up to 1.57 $\mu g\ m^{-3}$).
7. Primary and secondary Brown Carbon plays a significant role at shorter wavelengths (370-660 nm) and contributes to total aerosol light absorption.
8. Traffic volume study shows the vehicular category (HDDV and 4W) plays a vital role

in Black Carbon emissions.

9. Traffic-derived Black Carbon was found to be accumulated (7 μg m^{-3}) at some locations (150 m) due to the region's small and steep-sloped hilly topography.
10. Black Carbon concentrations were reduced (75%) by implementing the Bharat Stage (specially BS-VI) emission norms.
11. The health risk approximation of Black Carbon is projected to be about 25 passively smoked cigarette per day in winter.

7.4 Specific conclusion

1. Biomass emission produces secondary B_rC, and secondary sources contribute to the $b_{abs\_B_rC}$ during winter nighttime.
2. Black Carbon absorption coefficient was related to residential biomass-burning during winter nighttime.
3. Traffic is a dominant source of Black Carbon emissions than biomass burning in the study region.
4. Low wind with hill fog facilitated the rise of Black Carbon concentration in the complex terrain.
5. Modelled Black Carbon concentrations agreed with those estimated by the two-component mixing model.
6. On-site meteorological data produce more reliable dispersion calculations than WRF modelled data.
7. The Black Carbon from fossil fuel combustion for BS-IV decreased by 35% and 75% for BS-VI emission norms.
8. Major anions (e.g., NO_3^- and SO_4^{2-}) maximizes during the initial days of winter due to fossil fuel combustion and biomass burning.
9. The daily mean $PM_{2.5}$ and PM_{10} concentration levels during winter were more than twice as high as those recommended by WHO.

7.5 Limitations

1. This study was mainly focused on the winter and pre-monsoon season when air quality is expected to be highly poor. The optical properties also may vary in different seasons.
2. The measurement locations were limited to two.
3. Other components of carbonaceous aerosols were not investigated due to lack of the instruments.

7.6 Future scope

1. The used techniques may be applied to apportion the Black Carbon sources in different seasons and optical properties of different seasons could be inter-compared.
2. Emission inventory may be developed to incorporate the biomass burning emissions in dispersion modelling.
3. The modelling exercise may be performed by including the night-time datasets.
4. The domain of the modelling may be increased to analyze and verify the dispersion of air pollutants.

Appendix

For about 6% of the cases, $AAE_{370\text{-}880}$ was more than 1.5, marking a significant contribution from biomass or biofuel burning (Reddy and Venkataraman, 2002). However, the fraction (for 470-950 nm) $AAE_{470\text{-}950} > 1.5$ was found to be much lower (1.3%), indicating lesser impacts of BB as the wavelength increased. Hence, the pair of 370-880 nm band was selected to evaluate the influence of FF and BB on the whole BC. The best AAE values were chosen for FF and BB emissions by studying a frequency distribution graph fitted with a standard curve of hourly-average $AAE_{370\text{-}880}$ values observed at the site, as shown in Fig. A.1a.

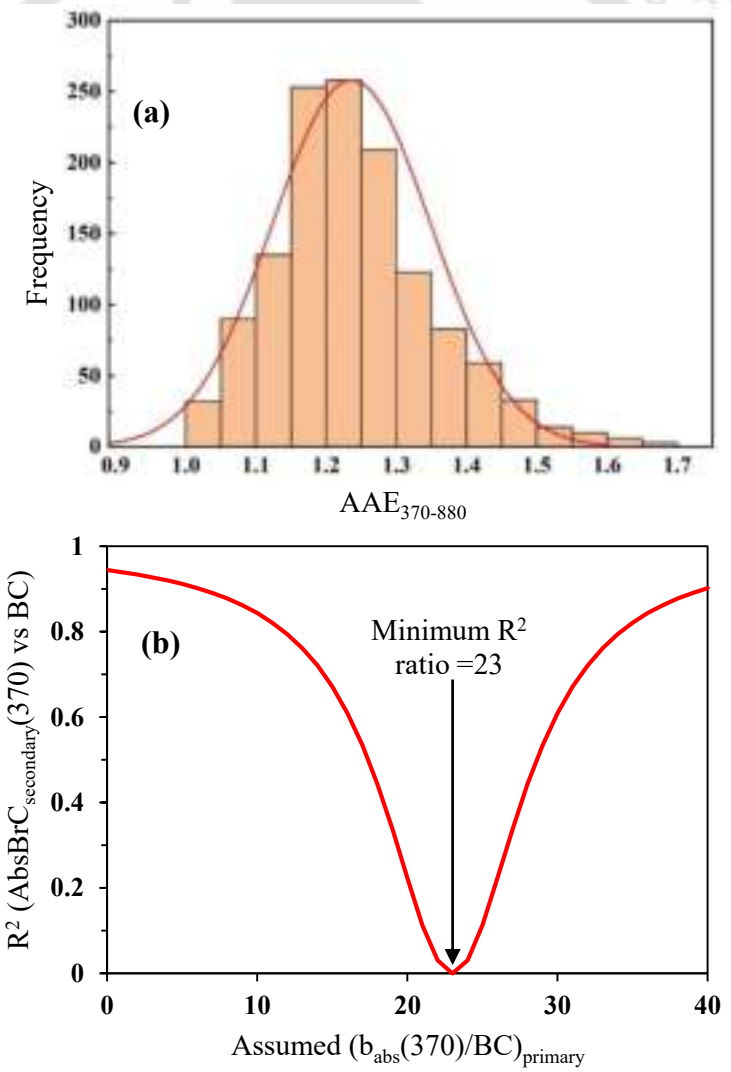

Fig. A.1 Selection of the best (a) $AAE_{370\text{-}880}$ values for FF and BB contribution to total BC and (b) primary emission ratio for light absorption at 370 nm and BC $(b_{abs\_370}/BC)_{pri}$ during winter.

Fig. A.2 shows the wind rose diagram for each monitored months during winter season. As observed, the prevailing wind was from the East-South-East direction during entire winter period.

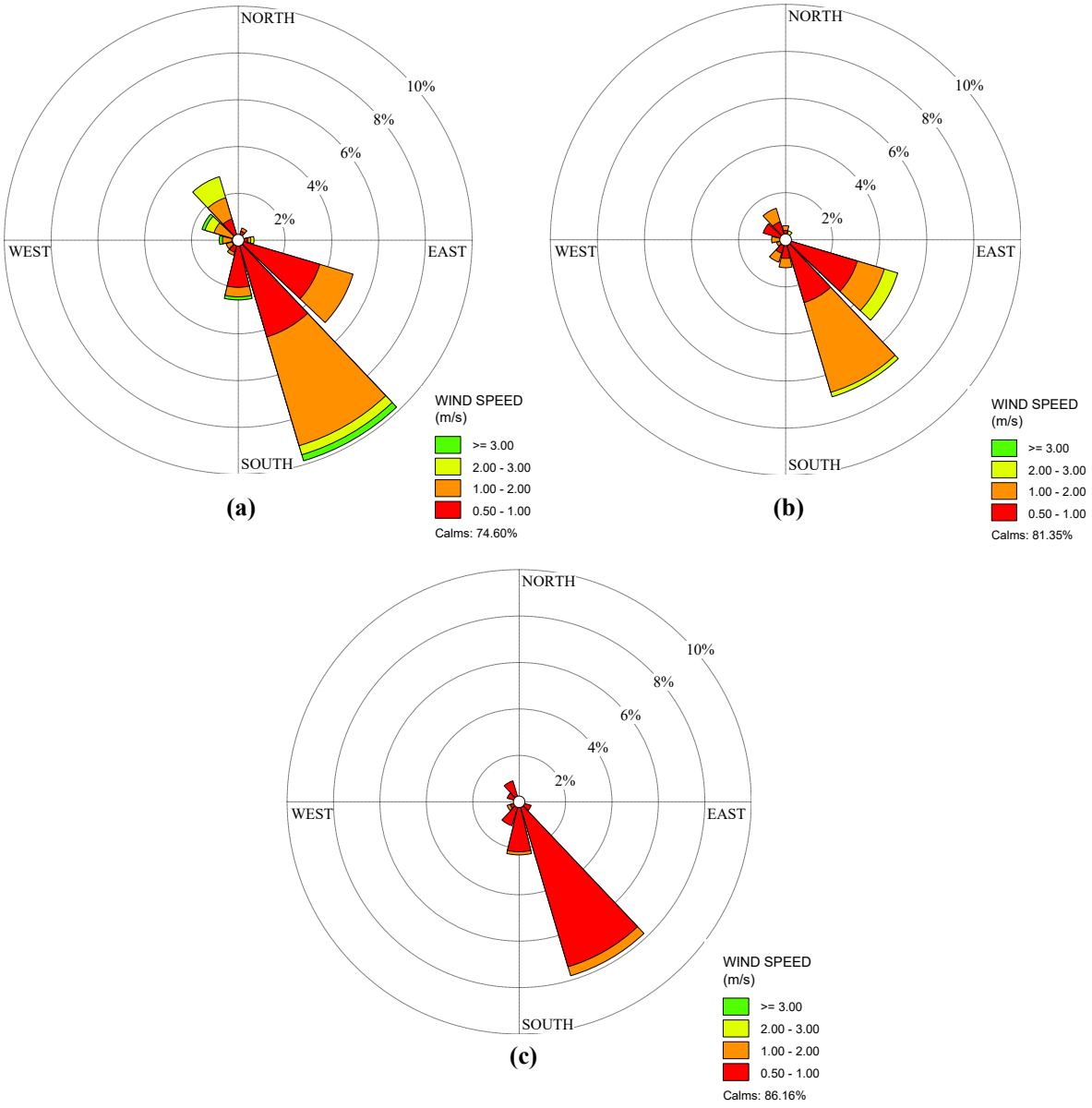

Fig. A.2 Wind rose plots for each month of winter.

A calm condition is regarded as the state of meteorology when wind speed is below a threshold limit which is generally taken as 0.5 m s^{-1} (Jeong et al., 2013). During the winter season, the conditions was calm. The calm conditions was observed for about 74 to 86%. Most of the wind speed was below 0.5 m s^{-1}.

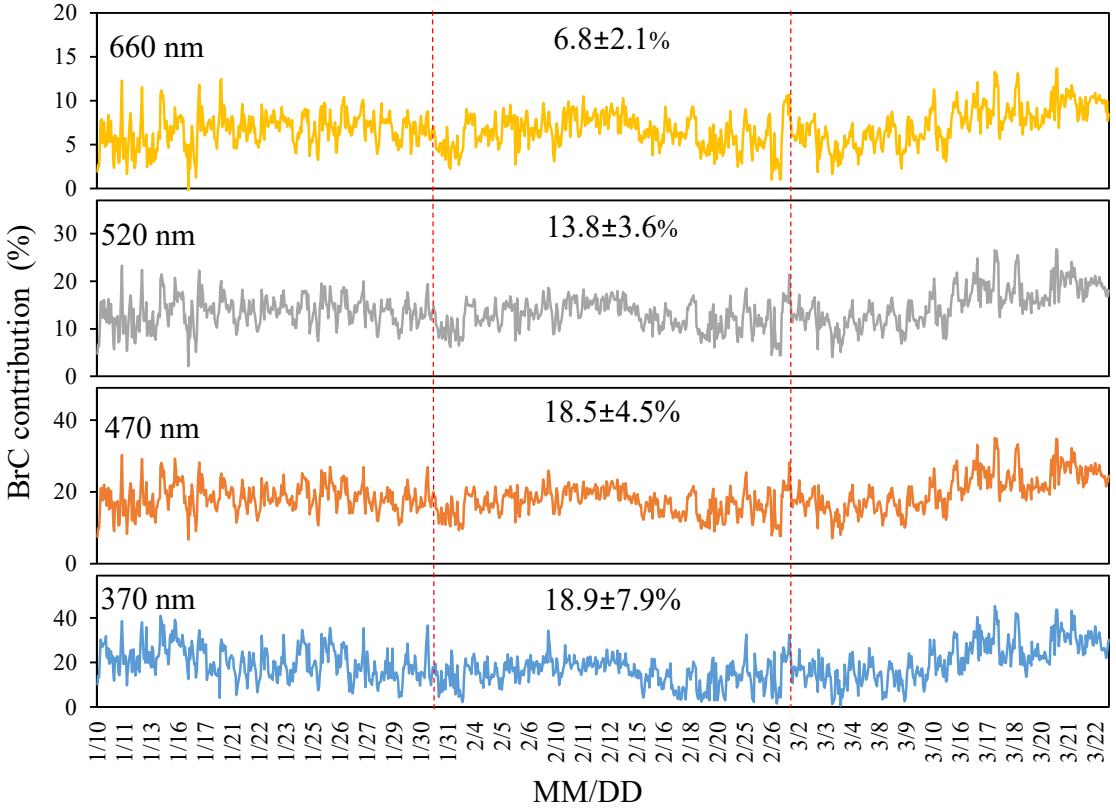

Fig. A.3 Hourly time series of the Brown Carbon contribution to aerosol light absorption at different wavelengths during winter.

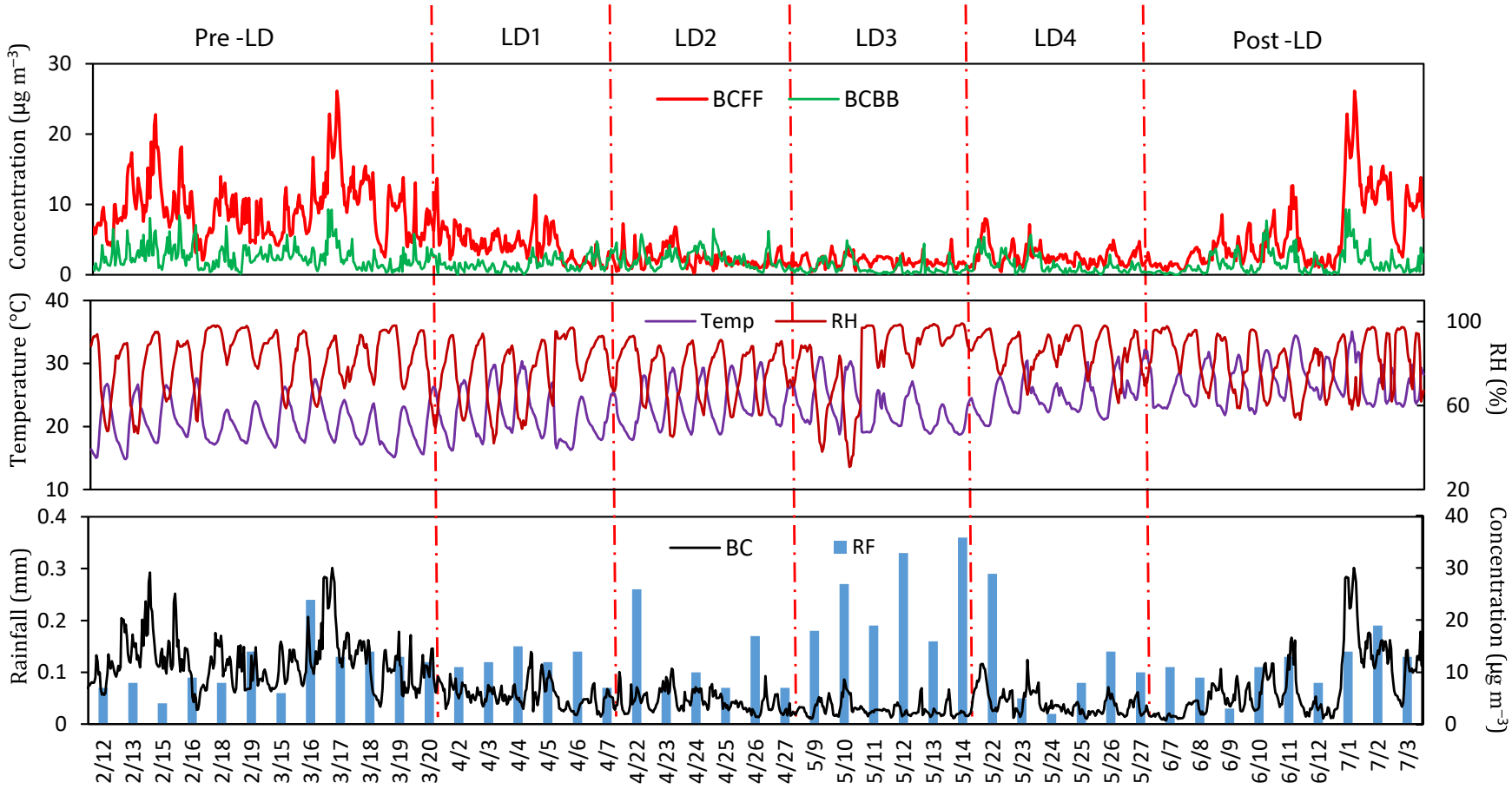

Fig. A.4 Temporal variations in Black Carbon mass concentration with the rainfall, temperature, and relative humidity during COVID-19 period. Rainfall denotes the daily averaged values.

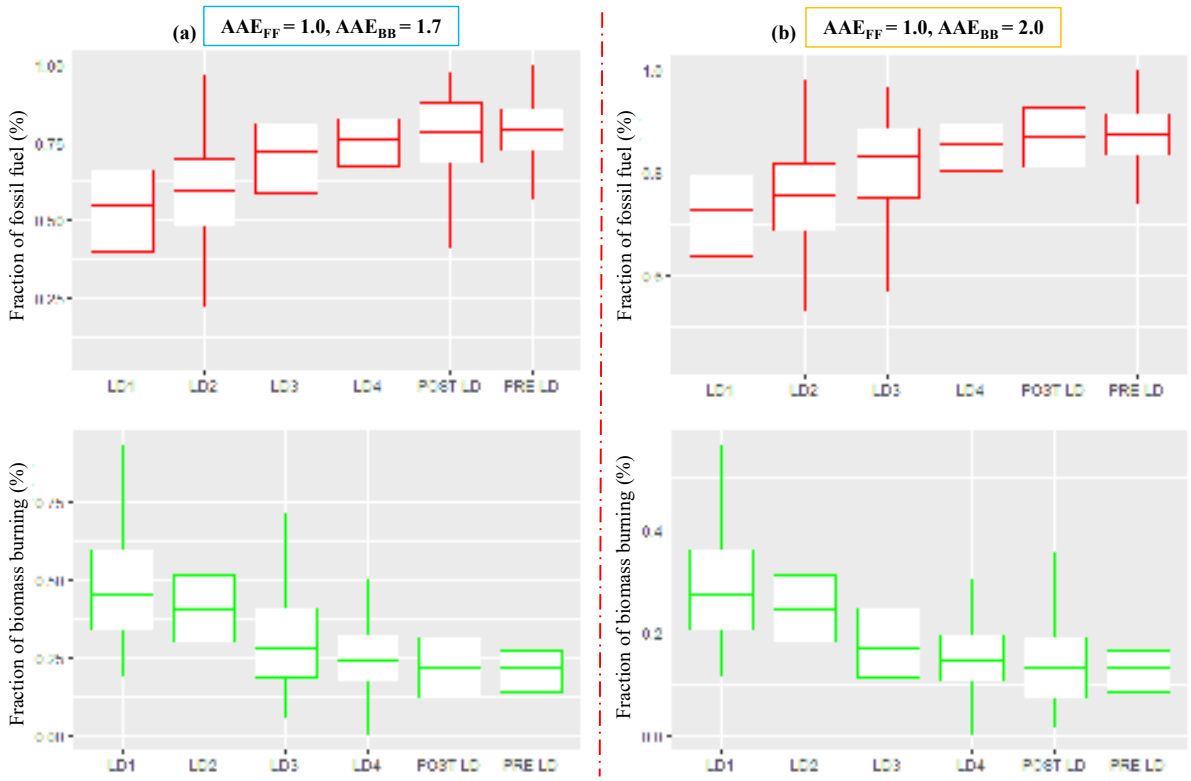

Fig. A.5 Source apportionment of fossil fuel and biomass burning in total BC_{880} using (a) revised and (b) default Aethalometer (AE33) model during COVID-19 period.

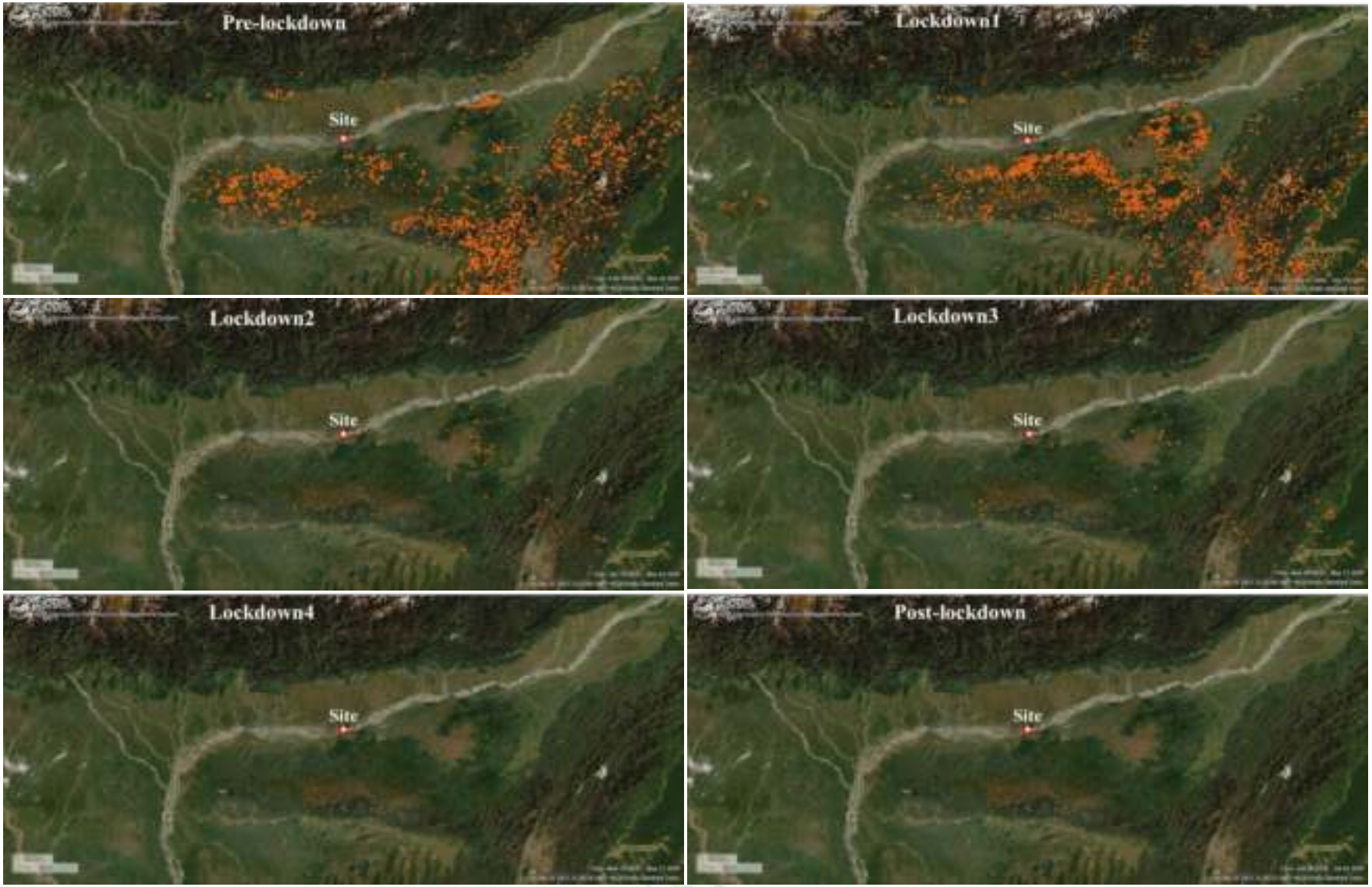

Fig. A.6 Fire maps during various phases of COVID-19 lockdown.

References

Al-Jeelani, H. A. (2013). The Impact of Traffic Emission on Air Quality in an Urban Environment. *Journal of Environmental Protection*, 4(2):205–217.

Ambade, B., Sankar, T. K., Panicker, A. S., Gautam, A. S., and Gautam, S. (2021). Characterization, seasonal variation, source apportionment and health risk assessment of black carbon over an urban region of East India. *Urban Climate*, 38(May):100896.

Andreae, M. O. and Gelencsér, A. (2006). Black carbon or brown carbon? the nature of light-absorbing carbonaceous aerosols. *Atmospheric Chemistry and Physics*, 6(10):3131–3148.

Andreae, M. O. and Metlet, P. (2001). Emission of trace gases and aerosols from biomass burning. *Global Biogeochemical Cycles*, 15(4):955–966.

ARAI (2008). Air Qaulity Moniotring Project: Indian Clean Air Programme (ICAP) as a part of Ambient Air Quality Monitoring and Emission Source Apportionment Studies. Technical report, ARAI.

ARAI (2017). The Automotive Research Association of India on behalf of Automotive Industry Standards Committee (AISC): Indian Emission Regulations. Technical report, ARAI.

Awasthi, A., Agarwal, R., Mittal, S. K., Singh, N., Singh, K., and Gupta, P. K. (2011). Study of size and mass distribution of particulate matter due to crop residue burning with seasonal variation in rural area of Punjab, India. *Journal of Environmental Monitoring*, 13(4):1073–1081.

Babu, S. S., Chaubey, J. P., Krishna Moorthy, K., Gogoi, M. M., Kompalli, S. K., Sreekanth, V., Bagare, S. P., Bhatt, B. C., Gaur, V. K., Prabhu, T. P., and Singh, N. S. (2011). High altitude (˜4520 m amsl) measurements of black carbon aerosols over western trans-Himalayas: Seasonal heterogeneity and source apportionment. *Journal of Geophysical Research Atmospheres*, 116(24):1–15.

Balakrishnaiah, G., Raghavendra Kumar, K., Suresh Kumar Reddy, B., Swamulu, C., Rama Gopal, K., Reddy, R. R., Reddy, L. S., Nazeer Ahammed, Y., Narasimhulu, K., Krishnamoorthy, K., and Suresh Babu, S. (2011). Anthropogenic impact on the temporal variations of black carbon and surface aerosol mass concentrations at a tropical semi-arid station in southeastern region of India. *Journal of Asian Earth Sciences*, 42(6):1297–1308.

Barman, N. and Gokhale, S. (2019). Urban black carbon - source apportionment, emissions and long-range transport over the Brahmaputra River Valley. *Science of the Total Environment*, 693:133577.

Begam, G. R., Vachaspati, C. V., Ahammed, Y. N., Kumar, K. R., Babu, S. S., and Reddy, R. R. (2016). Measurement and analysis of black carbon aerosols over a tropical semi-arid station in Kadapa, India. *Atmospheric Research*, 171:77–91.

Behera, S. N. and Sharma, M. (2010). Reconstructing primary and secondary components of PM2.5 composition for an Urban Atmosphere. *Aerosol Science and Technology*, 44(11):983–992.

Bond, T. C. and Bergstrom, R. W. (2006). Light absorption by carbonaceous particles: An investigative review. *Aerosol Science and Technology*, 40(1):27–67.

Bond, T. C., Bhardwaj, E., Dong, R., Jogani, R., Jung, S., Roden, C., Streets, D. G., and Trautmann, N. M. (2007). Historical emissions of black and organic carbon aerosol from energy-related combustion, 1850-2000. *Global Biogeochemical Cycles*, 21(2):1–16.

Bond, T. C., Doherty, S. J., Fahey, D. W., Forster, P. M., Berntsen, T., Deangelo, B. J., Flanner, M. G., Ghan, S., Kärcher, B., Koch, D., Kinne, S., Kondo, Y., Quinn, P. K., Sarofim, M. C., Schultz, M. G., Schulz, M., Venkataraman, C., Zhang, H., Zhang, S., Bellouin, N., Guttikunda, S. K., Hopke, P. K., Jacobson, M. Z., Kaiser, J. W., Klimont, Z., Lohmann, U., Schwarz, J. P., Shindell, D., Storelvmo, T., Warren, S. G., and Zender, C. S. (2013). Bounding the role of black carbon in the climate system: A scientific assessment. *Journal of Geophysical Research Atmospheres*, 118(11):5380–5552.

Bond, T. C., Streets, D. G., Yarber, K. F., Nelson, S. M., Woo, J.-h., and Klimont, Z. (2004). A technology-based global inventory of black and organic carbon emissions from combustion. *Journal of Geophysical Research*, 109:1–43.

Bond, T. C. and Sun, K. (2005). Can reducing black carbon emissions counteract global warming? *Environmental Science and Technology*, 39(16):5921–5926.

Bond, T. C., Zarzycki, C., Flanner, M. G., and Koch, D. M. (2011). Quantifying immediate radiative forcing by black carbon and organic matter with the Specific Forcing Pulse. *Atmospheric Chemistry and Physics*, 11(4):1505–1525.

Buseck, P. R., Adachi, K., Gelencsér, a., Tompa, É., and Pósfai, M. (2012). Are black carbon and soot the same? *Atmospheric Chemistry and Physics Discussions*, 12(9):24821–24846.

Cao, J., Tie, X., Xu, B., Zhao, Z., Zhu, C., Li, G., and Liu, S. (2010). Measuring and modeling black carbon (BC) contamination in the SE Tibetan Plateau. *Journal of Atmospheric Chemistry*, 67(1):45–60.

Cape, J. N., Coyle, M., and Dumitrean, P. (2012). The atmospheric lifetime of black carbon. *Atmospheric Environment*, 59:256–263.

Chakrabarty, R. K., Garro, M. A., Wilcox, E. M., and Moosmller, H. (2012). Strong radiative heating due to wintertime black carbon aerosols in the Brahmaputra River Valley. *Geophysical Research Letters*, 39(9):1–5.

Chang, J. C. and Hanna, S. R. (2004). Air quality model performance evaluation. *Meteorology and Atmospheric Physics*, 87(1):167–196.

Chaudhury, A. S., Nikhil, V. A., and Gokhale, S. (2022). Black carbon in different climatic seasons of the Brahmaputra River Valley of Northeast India Field measurements at two different heights and analysis. *Atmospheric Pollution Research*, 13(3):101327.

Chauhan, A. and Singh, R. P. (2020). Decline in PM2.5 concentrations over major cities around the world associated with COVID-19. *Environmental Research*, 187(April):109634.

Chen, D., Liao, H., Yang, Y., Chen, L., Zhao, D., and Ding, D. (2022). Simulated impacts of vertical

distributions of black carbon aerosol on meteorology and PM2.5 concentrations in Beijing during severe haze events. *Atmospheric Chemistry and Physics*, 22(3):1825–1844.

Chen, Y., Zhang, S., Peng, C., Shi, G., Tian, M., Huang, R. J., Guo, D., Wang, H., Yao, X., and Yang, F. (2020). Impact of the COVID-19 pandemic and control measures on air quality and aerosol light absorption in Southwestern China. *Science of the Total Environment*, 749:141419.

Chowdhuri, I., Pal, S. C., Saha, A., Chakrabortty, R., Ghosh, M., and Roy, P. (2020). Significant decrease of lightning activities during COVID-19 lockdown period over Kolkata megacity in India. *Science of the Total Environment*, 747:141321.

CPCB (2011). Guidelines for the Measurement of Ambient Air Pollutants Volume-CENTRAL POLLUTION CONTROL BOARD Guidelines for Manual Sampling & Analyses. Technical report, CPCB.

Cui, S., Xian, J., Shen, F., Zhang, L., Deng, B., Zhang, Y., and Ge, X. (2021). One-year real-time measurement of black carbon in the rural area of qingdao, northeastern china: Seasonal variations, meteorological effects, and the covid-19 case analysis. *Atmosphere*, 12(3).

Das, M., Maiti, S. K., and Mukhopadhyay, U. (2006). Distribution of PM2.5 and PM10-2.5 in PM10 fraction in ambient air due to vehicular pollution in Kolkata megacity. *Environmental Monitoring and Assessment*, 122:111–123.

Deng, J., Guo, H., Zhang, H., Zhu, J., Wang, X., and Fu, P. (2020). Source apportionment of black carbon aerosols from light absorption observation and source-oriented modeling: An implication in a coastal city in China. *Atmospheric Chemistry and Physics*, 20(22):14419–14435.

Diapouli, E., Kalogridis, A. C., Markantonaki, C., Vratolis, S., Fetfatzis, P., Colombi, C., and Eleftheriadis, K. (2017). Annual variability of black carbon concentrations originating from biomass and fossil fuel combustion for the suburban aerosol in Athens, Greece. *Atmosphere*, 8(12):234.

Draxler, R. and Rolph, G. (2016). HYSPLIT (HYbrid Single-particle Lagrangian Integrated Trajectory) Model Access via NOAA ARL READY. NOAA Air Resources Laboratory, Silver Spring, MD Website. *HYSPLIT*.

Drinovec, L., Močnik, G., Zotter, P., Prévôt, A. S., Ruckstuhl, C., Coz, E., Rupakheti, M., Sciare, J., Müller, T., Wiedensohler, A., and Hansen, A. D. (2015). The "dual-spot" Aethalometer: An improved measurement of aerosol black carbon with real-time loading compensation. *Atmospheric Measurement Techniques*, 8(5):1965–1979.

Dumka, U. C., Kaskaoutis, D. G., Devara, P. C., Kumar, R., Kumar, S., Tiwari, S., Gerasopoulos, E., and Mihalopoulos, N. (2019). Year-long variability of the fossil fuel and wood burning black carbon components at a rural site in southern Delhi outskirts. *Atmospheric Research*, 216(June 2018):11–25.

Dumka, U. C., Kaskaoutis, D. G., Tiwari, S., Safai, P. D., Attri, S. D., Soni, V. K., Singh, N., and Mihalopoulos, N. (2018). Assessment of biomass burning and fossil fuel contribution to black carbon concentrations in Delhi during winter. *Atmospheric Environment*, 194(August):93–109.

Economic survey of Assam (2017). Transportation and development department Government of Assam 2018. Technical report, Economic survey of Assam.

Economic Survey of India (2015). Ministry of Finance, Department of Economic Affairs Economic Division New Delhi. Technical report, Economic survey of India.

Evans, M., Kholod, N., Kuklinski, T., Denysenko, A., Smith, S. J., Staniszewski, A., Min, W., Liu, L., and Bond, T. C. (2017). Black carbon emissions in Russia : A critical review. *Atmospheric Environment*, 163:9–21.

Fröhlich, E., Mercuri, A., Wu, S., and Salar-Behzadi, S. (2016). Measurements of deposition, lung surface area and lung fluid for simulation of inhaled compounds. *Frontiers in Pharmacology*, 7(JUN):1–10.

Fuller, K. A. and Kreidenweis, S. M. (1999). Effects of mixing on extinction by carbonaceous particles mass range from under and the intermediate value cases , and we suggest may often be less although variations in optical constants and , calculations indicate that for realistic dry particle popula. *Journal of Geophysical Research*, 104(D13):15941–15954.

Ganguly, D., Jayaraman, A., Rajesh, T. A., and Gadhavi, H. (2006). Wintertime aerosol properties during foggy and nonfoggy days over urban center Delhi and their implications for shortwave radiative forcing. *Journal of Geophysical Research Atmospheres*, 111(15):1–15.

Global Adults Tobacco Survey (2019). A fact sheet provided by the Ministry of Health and Family Welfare, Government of India. Technical report, Global Adults Tobacco Survey.

Goel, V., Hazarika, N., Kumar, M., Singh, V., Thamban, N. M., and Tripathi, S. N. (2021). Variations in Black Carbon concentration and sources during COVID-19 lockdown in Delhi. *Chemosphere*, 270:129435.

Gogoi, M. M., Suresh Babu, S., Arun, B. S., Moorthy, K. K., Ajay, A., Ajay, P., Suryavanshi, A., Borgohain, A., Guha, A., Shaikh, A., Pathak, B., Gharai, B., Ramasamy, B., Balakrishnaiah, G., Menon, H. B., Kuniyal, J. C., Krishnan, J., Gopal, K. R., Maheswari, M., Naja, M., Kaur, P., Bhuyan, P. K., Gupta, P., Singh, P., Srivastava, P., Singh, R. S., Kumar, R., Rastogi, S., Kundu, S. S., Kompalli, S. K., Panda, S., Rao, T. C., Das, T., and Kant, Y. (2021). Response of ambient BC concentration across the Indian region to the nation-wide lockdown: results from the ARFINET measurements of ISRO-GBP. *Cuirrent Science*, 120(2).

Gokhale, S. and Raokhande, N. (2008). Performance evaluation of air quality models for predicting PM10 and PM2.5 concentrations at urban traffic intersection during winter period. *Science of the Total Environment*, 394(1):9–24.

Goldreich, Y., Druyan, L., and Berger, H. (1986). The interaction of valley/mountain winds with A diurnally veering sea/land breeze. *Journal of Climatology*, 6(5):551–561.

Graber, E. R. and Rudich, Y. (2006). Atmospheric Chemistry and Physics Atmospheric HULIS: How humic-like are they? A comprehensive and critical review. *Atmos. Chem. Phys*, 6:729–753.

Gustafsson, Ö., Kruså, M., Zencak, Z., Sheesley, R. J., Granat, L., Engström, E., Praveen, P. S., Rao, P. S.,

Leck, C., and Rodhe, H. (2009). Brown clouds over South Asia: Biomass or fossil fuel combustion? *Science*, 323(5913):495–498.

Hammes, K., Smernik, R. J., Skjemstad, J. O., and Schmidt, M. W. (2008). Characterisation and evaluation of reference materials for black carbon analysis using elemental composition, colour, BET surface area and 13C NMR spectroscopy. *Applied Geochemistry*, 23(8):2113–2122.

Han, F., Kota, S. H., Wang, Y., and Zhang, H. (2017). Source apportionment of PM2.5 in Baton Rouge, Louisiana during 20092014. *Science of the Total Environment*, 586:115–126.

Hanna, S. R. (1988). Air quality model evaluation and uncertainty. *Journal of the Air Pollution Control Association*, 38(4):406–412.

Hanna, S. R. (1993). Uncertainties in Air Quality Model Predictions. In: Kaplan, H., Dinar, N., Lacser, A., Alexander, Y. (eds). *Transport and Diffusion in Turbulent Fields*, pages 3–20.

Healy, R. M., Sofowote, U., Su, Y., Debosz, J., Noble, M., Jeong, C., Wang, J. M., Hilker, N., Evans, G. J., Doerksen, G., Jones, K., and Munoz, A. (2017). Ambient measurements and source apportionment of fossil fuel and biomass burning black carbon in Ontario. *Atmospheric Environment journal*, 161:37–37.

Helin, A., Niemi, J. V., Virkkula, A., Pirjola, L., Teinilä, K., Backman, J., Aurela, M., Saarikoski, S., Rönkkö, T., Asmi, E., and Timonen, H. (2018). Characteristics and source apportionment of black carbon in the Helsinki metropolitan area, Finland. *Atmospheric Environment*, 190(July):87–98.

Huang, R. J., Wang, Y., Cao, J., Lin, C., Duan, J., Chen, Q., Li, Y., Gu, Y., Yan, J., Xu, W., Fröhlich, R., Canonaco, F., Bozzetti, C., Ovadnevaite, J., Ceburnis, D., Canagaratna, M. R., Jayne, J., Worsnop, D. R., El-Haddad, I., Prevot, A. S., and O'Dowd, C. D. (2019). Primary emissions versus secondary formation of fine particulate matter in the most polluted city (Shijiazhuang) in North China. *Atmospheric Chemistry and Physics*, 19(4):2283–2298.

Hnová, I., Brabec, M., Malý, M., Dumitrescu, A., and Geletič, J. (2021). Terrain and its effects on fog occurrence. *Science of the Total Environment*, 768:144359.

IARC (2014). Diesel and gasoline engine exhausts and some nitroarenes. *International Agency for Research on Cancer*, page 105.

INCCA (2011). Black Carbon Research Initiative National Carbonaceous Aerosols Programme (NCAP) science Plan. Indian Network for Climate Change Assessment. Ministry of Environment and Forests, Ministry of Earth Sciences, Ministry of Science and Technology, and Indian. Technical report, INCCA.

Invernizzi, G., Ruprecht, A., Mazza, R., De Marco, C., Močnik, G., Sioutas, C., and Westerdahl, D. (2011). Measurement of black carbon concentration as an indicator of air quality benefits of traffic restriction policies within the ecopass zone in Milan, Italy. *Atmospheric Environment*, 45(21):3522–3527.

IPCC (2007a). Climate Change 2007, Mitigation. B. Metz, O.R. Davidson, P.R. Bosch, R. Dave, L.A. Meyer. Contribution of Working Group III to the Fourth Assessment, Report of the Intergovernmental

Panel on Climate Change, Cambridge University Press, Cambridge, United Ki. Technical report, IPCC.

IPCC (2007b). Climate Change 2007, The Physical Science Basis. S. Solomon, D. Qin, M. Manning, Z. Chen, M. Marquis, K.B. Averyt, M. Tignor, and H.L. Miller, Contribution of Working Group I to the Fourth Assessment. Technical report, IPCC.

Jacobson, M. Z. (2001). Strong radiative heating due to the mixing state of black carbon in atmospheric aerosols. *Nature*, 409(6821):695–697.

Jacobson, M. Z. (2004). Climate response of fossil fuel and biofuel soot, accounting for soot's feedback to snow and sea ice albedo and emissivity. *Journal of Geophysical Research D: Atmospheres*, 109(21):1–15.

Jansen, K. L., Larson, T. V., Koenig, J. Q., Mar, T. F., Fields, C., Stewart, J., and Lippmann, M. (2005). Associations between health effects and particulate matter and black carbon in subjects with respiratory disease. *Environmental Health Perspectives*, 113(12):1741–1746.

Jenkins, G. (2014). A comparison between two types of widely used weather stations. *Weather*, 69(4):105–110.

Jeong, H., Park, M., Hwang, W., Kim, E., and Han, M. (2013). The effect of calm conditions and wind intervals in low wind speed on atmospheric dispersion factors. *Annals of Nuclear Energy*, 55:230–237.

Kasten, F. and Czeplak, G. (1980). SOLAR AND TERRESTRIAL RADIATION DEPENDENT ON THE AMOUNT AND TYPE OF CLOUD. *Solar Energy*, 24:177–189.

Katsanos, D., Bougiatioti, A., Liakakou, E., Kaskaoutis, D. G., Stavroulas, I., Paraskevopoulou, D., Lianou, M., Psiloglou, B. E., Gerasopoulos, E., Pilinis, C., and Mihalopoulos, N. (2019). Optical properties of near-surface urban aerosols and their chemical tracing in a mediterranean city (Athens). *Aerosol and Air Quality Research*, 19(1):49–70.

Kaur, P., Srinivasan, P., Dhar, P., Kumar De, B., and Guha, A. (2020). Study of spectral characteristics of black carbon from biomass burning and source apportionment over Agartala in the northeastern India. *Environmental Science and Pollution Research*, 27(14):16584–16598.

Keller, J. P., Olives, C., Kim, S. Y., Sheppard, L., Sampson, P. D., Szpiro, A. A., Oron, A. P., Lindström, J., Vedal, S., and Kaufman, J. D. (2015). A unified spatiotemporal modeling approach for predicting concentrations of multiple air pollutants in the multi-ethnic study of atherosclerosis and air pollution. *Environmental Health Perspectives*, 123(4):301–309.

Kim, H. C. and Hofmann, E. E. (2005). Evaluation and derivation of cloud-cover algorithms for calculation of surface irradiance in sub-Antarctic and Antarctic environments. *Antarctic Science*, 17(1):135–149.

Kirchstetter, T. W., Novakov, T., and Hobbs, P. V. (2004). Evidence that the spectral dependence of light absorption by aerosols is affected by organic carbon. *Journal of Geophysical Research D: Atmospheres*, 109(21):1–12.

Kondo, Y., Komazaki, Y., Miyazaki, Y., Moteki, N., Takegawa, N., Kodama, D., Deguchi, S., Nogami, M., Fukuda, M., Miyakawa, T., Morino, Y., Koike, M., Sakurai, H., and Ehara, K. (2006). Temporal variations of elemental carbon in Tokyo. *Journal of Geophysical Research Atmospheres*, 111(12):1–17.

Kumar, R. and Joseph, A. E. (2006). Air pollution concentrations of PM2.5, PM10 and NO2 at ambient and Kerbsite and their correlation in Metro City - Mumbai. *Environmental Monitoring and Assessment*, 119(1-3):191–199.

Kumari, P. and Toshniwal, D. (2020). Impact of lockdown measures during COVID-19 on air quality A case study of India. *International Journal of Environmental Health Research*.

Lack, D. A., Moosmüller, H., McMeeking, G. R., Chakrabarty, R. K., and Baumgardner, D. (2014). Characterizing elemental, equivalent black, and refractory black carbon aerosol particles: A review of techniques, their limitations and uncertainties. *Analytical and Bioanalytical Chemistry*, 406(1):99–122.

Lamarque, J., Bond, T. C., Eyring, V., Granier, C., Heil, A., Klimont, Z., Lee, D., Liousse, C., Mieville, A., Insu, C., and Latmos-ipsl, U. M. R. (2010). and Physics Historical (1850 2000) gridded anthropogenic and biomass burning emissions of reactive gases and aerosols : methodology and application. *Atmsopheric Chemistry and Physiscs*, 10:7017–7039.

Laskin, A., Laskin, J., and Nizkorodov, S. A. (2015). Chemistry of Atmospheric Brown Carbon. *Chemical Reviews*, 115(10):4335–4382.

Latha, K. M. and Badarinath, K. V. (2005). Environmental pollution due to black carbon aerosols and its impacts in a tropical urban city. *Journal of Quantitative Spectroscopy and Radiative Transfer*, 92(3):311–319.

Li, S., Zhu, M., Yang, W., Tang, M., Huang, X., Yu, Y., Fang, H., Yu, X., Yu, Q., Fu, X., Song, W., Zhang, Y., Bi, X., and Wang, X. (2018). Filter-based measurement of light absorption by brown carbon in PM2.5 in a megacity in South China. *Science of the Total Environment*, 633:1360–1369.

Liakakou, E., Stavroulas, I., Kaskaoutis, D. G., Grivas, G., Paraskevopoulou, D., Dumka, U. C., Tsagkaraki, M., Bougiatioti, A., Oikonomou, K., Sciare, J., Gerasopoulos, E., and Mihalopoulos, N. (2020). Long-term variability, source apportionment and spectral properties of black carbon at an urban background site in Athens, Greece. *Atmospheric Environment*, 222(November 2019):117137.

Liang, M. S., Keener, T. C., Birch, M. E., Baldauf, R., Neal, J., and Yang, Y. J. (2013). Low-wind and other microclimatic factors in near-road black carbon variability: A case study and assessment implications. *Atmospheric Environment*, 80:204–215.

Lin, W., Dai, J., Liu, R., Zhai, Y., Yue, D., and Hu, Q. (2019). Integrated assessment of health risk and climate effects of black carbon in the Pearl River Delta region, China. *Environmental Research*, 176(May):108522.

Lin, Y., Budisulistiorini, S., Chu, K., Siejack, R., Zhang, H., Riva, M., Zhang, Z., Gold, A., Kautzman, K., and Surratt, J. (2014). bsorbing oligomer formation in secondary organic aerosol from reactive uptake of isoprene epoxydiols. *Environmental science & technology*, 48(20):12012–12021.

Liu, Y., Yan, C., and Zheng, M. (2018). Science of the Total Environment Source apportionment of black carbon during winter in Beijing. *Science of the Total Environment*, 618:531–541.

Lu, Z., Zhang, Q., and Streets, D. G. (2011). Sulfur dioxide and primary carbonaceous aerosol emissions in China and India, 1996-2010. *Atmospheric Chemistry and Physics*, 11(18):9839–9864.

Lyamani, H., Olmo, F. J., Foyo, I., and Alados-Arboledas, L. (2011). Black carbon aerosols over an urban area in south-eastern Spain: Changes detected after the 2008 economic crisis. *Atmospheric Environment*, 45(35):6423–6432.

Magalhaes, S., Baumgartner, J., and Weichenthal, S. (2018). Impacts of exposure to black carbon , elemental carbon , and ultra fi ne particles from indoor and outdoor sources on blood pressure in adults : A review of epidemiological evidence. *Environmental Research*, 161:345–353.

Mahato, S., Pal, S., and Ghosh, K. G. (2020). Effect of lockdown amid COVID-19 pandemic on air quality of the megacity Delhi, India. *Science of the Total Environment*, 730:139086.

Matt, G. E., Quintana, P. J., Hovell, M. F., Bernert, J. T., Song, S., Novianti, N., Juarez, T., Floro, J., Gehrman, C., Garcia, M., and Larson, S. (2004). Households contaminated by environmental tobacco smoke: Sources of infant exposures. *Tobacco Control*, 13(1):29–37.

Michanowicz, D. R., Shmool, J. L., Tunno, B. J., Tripathy, S., Gillooly, S., Kinnee, E., and Clougherty, J. E. (2016). A hybrid land use regression/AERMOD model for predicting intra-urban variation in PM2.5. *Atmospheric Environment*, 131:307–315.

Mousavi, A., Sowlat, M. H., Hasheminassab, S., Polidori, A., and Sioutas, C. (2018). Spatio-temporal trends and source apportionment of fossil fuel and biomass burning black carbon (BC) in the Los Angeles Basin. *Science of the Total Environment*, 640-641:1231–1240.

Myung, C. L. and Park, S. (2012). EXHAUST NANOPARTICLE EMISSIONS FROM INTERNAL COMBUSTION ENGINES: A REVIEW. *International Journal of Automotive Technology*, 13(1):9–22.

NCAP (2020). NCAP Tracker, National Clean Air Program, 2020. Technical report, NCAP.

Nilsson, E. D. and Rannik, O. (2001). Turbulent aerosol fluxes over the Arctic Ocean: 1. Dry deposition over sea and pack ice. *Journal of Geophysical Research Atmospheres*, 106(D23):32125–32137.

Novakov, T., Ramanathan, V., Hansen, J. E., Kirchstetter, T. W., Sato, M., Sinton, J. E., and Sathaye, J. A. (2003). Large historical changes of fossil-fuel black carbon aerosols. *Geophysical Research Letters*, 30(6):1–4.

Paliwal, U., Sharma, M., and Burkhart, J. F. (2016). Monthly and spatially resolved black carbon emission inventory of India: Uncertainty analysis. *Atmospheric Chemistry and Physics*, 16(19):12457–12476.

Pandey, G. and Sharan, M. (2021). Application of AERMOD for the identification of a point-source release in the FFT-07 experiment. *Air Quality, Atmosphere and Health*, 14(5):679–690.

Pani, S. K., Wang, S. H., Lin, N. H., Chantara, S., Lee, C. T., and Thepnuan, D. (2020). Black carbon over an urban atmosphere in northern peninsular Southeast Asia: Characteristics, source apportionment, and associated health risks. *Environmental Pollution*, 259:113871.

Panicker, A. S., Ali, K., Beig, G., and Yadav, S. (2015). Characterization of particulate matter and carbonaceous aerosol over two urban environments in Northern India. *Aerosol and Air Quality Research*, 15(7):2584–2595.

Pathak, B., Bhuyan, P. K., Biswas, J., and Takemura, T. (2013). Long term climatology of particulate matter and associated microphysical and optical properties over Dibrugarh, North-East India and inter-comparison with SPRINTARS simulations. *Atmospheric Environment*, 69:334–344.

Pathak, B., Bhuyan, P. K., Saikia, A., Bhuyan, K., Ajay, P., Nath, S. J., and Bora, S. L. (2021). Impact of lockdown due to COVID-19 outbreak on O3 and its precursor gases, PM and BC over northeast India. *Current Science*, 120(2):322–331.

Penner, J., Eddleman, H., and Novakov, T. (1993). Towards the development of a global inventory for black carbon emissions. *Atmospheric Environment. Part A. General Topics*, 27(8):1277–1295.

Petzold, A., Ogren, J. A., Fiebig, M., Laj, P., Li, S. M., Baltensperger, U., Holzer-Popp, T., Kinne, S., Pappalardo, G., Sugimoto, N., Wehrli, C., Wiedensohler, A., and Zhang, X. Y. (2013). Recommendations for reporting black carbon measurements. *Atmospheric Chemistry and Physics*, 13(16):8365–8379.

Petzold, A., Schloesser, H., Sheridan, P. J., Patrick, W., Ogren, J. A., Virkkula, A., Petzold, A., Schloesser, H., Sheridan, P. J., Patrick, W., Ogren, J. A., Virkkula, A., Absorption, M., Petzold, A., Schloesser, H., Sheridan, P. J., Arnott, W. P., Ogren, J. A., and Virkkula, A. (2005). Evaluation of Multiangle Absorption Photometry for Measuring Aerosol Light Absorption Evaluation of Multiangle Absorption Photometry for Measuring Aerosol Light Absorption. *Aerosol Science and Technology*, 39(1):40–51.

Pillai, P. S., Suresh Babu, S., and Krishna Moorthy, K. (2002). A study of PM, PM10 and PM2.5 concentration at a tropical coastal station. *Atmospheric Research*, 61(2):149–167.

Pipal, A. S., Kulshrestha, A., and Taneja, A. (2011). Characterization and morphological analysis of airborne PM2.5 and PM10 in Agra located in north central India. *Atmospheric Environment*, 45(21):3621–3630.

Prabhu, V., Soni, A., Madhwal, S., Gupta, A., and Sundriyal, S. (2020). Black carbon and biomass burning associated high pollution episodes observed at Doon valley in the foothills of the Himalayas. *Atmospheric Research*, 243(April):105001.

Prasad, P., Roja Raman, M., Venkat Ratnam, M., Chen, W. N., Vijaya Bhaskara Rao, S., Gogoi, M. M., Kompalli, S. K., Sarat Kumar, K., and Suresh Babu, S. (2018). Characterization of atmospheric Black Carbon over a semi-urban site of Southeast India: Local sources and long-range transport. *Atmospheric Research*, 213(December 2017):411–421.

Qin, Y. M., Bo Tan, H., Li, Y. J., Jie Li, Z., Schurman, M. I., Liu, L., Wu, C., and Chan, C. K. (2018). Chemical characteristics of brown carbon in atmospheric particles at a suburban site near Guangzhou, China. *Atmospheric Chemistry and Physics*, 18(22):16409–16418.

Rajesh, T. A. and Ramachandran, S. (2018). Black carbon aerosol mass concentration, absorption and single scattering albedo from single and dual spot aethalometers: Radiative implications. *Journal of Aerosol Science*, 119(February):77–90.

Ramanathan, V. and Carmichael, G. (2008). Global and regional climate changes due to black carbon. *Nature geoscience*, 1:221–227.

Rana, A., Jia, S., and Sarkar, S. (2019). Black carbon aerosol in India: A comprehensive review of current status and future prospects. *Atmospheric Research*, 218(111):207–230.

Ranjan, A. K., Patra, A. K., and Gorai, A. K. (2020). Effect of lockdown due to SARS COVID-19 on aerosol optical depth (AOD) over urban and mining regions in India. *Science of the Total Environment*, 745:141024.

Reddy, M. S. and Venkataraman, C. (2002). Inventory of aerosol and sulphur dioxide emissions from India. Part II - Biomass combustion. *Atmospheric Environment*, 36(4):699–712.

Rehman, I. H., Ahmed, T., Praveen, P. S., Kar, A., and Ramanathan, V. (2011). Black carbon emissions from biomass and fossil fuels in rural India. *Atmospheric Chemistry and Physics*, 11(14):7289–7299.

Reid, J. S., Eck, T. F., Christopher, S. A., Koppman, R., Dubovik, O., Eleuterio, D. P., Holben, B. N., Reid, E. A., and Zhang, J. (2005). A review of biomass burning emissions part III: Intensive optical properties of biomass burning particles. *Atmospheric Chemistry and Physics*, 5(3):827–849.

Rupakheti, D., Adhikary, B., Praveen, P. S., Rupakheti, M., Kang, S., Mahata, K. S., Naja, M., Zhang, Q., Panday, A. K., and Lawrence, M. G. (2017). Pre-monsoon air quality over Lumbini, a world heritage site along the Himalayan foothills. *Atmospheric Chemistry and Physics*, 17(18):11041–11063.

Safai, P. D., Devara, P. C., Raju, M. P., Vijayakumar, K., and Rao, P. S. (2014). Relationship between black carbon and associated optical, physical and radiative properties of aerosols over two contrasting environments. *Atmospheric Research*, 149:292–299.

Saleh, R., Hennigan, C. J., McMeeking, G. R., Chuang, W. K., Robinson, E. S., Coe, H., Donahue, N. M., and Robinson, A. L. (2013). Absorptivity of brown carbon in fresh and photo-chemically aged biomass-burning emissions. *Atmospheric Chemistry and Physics*, 13(15):7683–7693.

Sandradewi, J., Prévôt, A. S., Weingartner, E., Schmidhauser, R., Gysel, M., and Baltensperger, U. (2008). A study of wood burning and traffic aerosols in an Alpine valley using a multi-wavelength Aethalometer. *Atmospheric Environment*, 42(1):101–112.

Sarkar, C., Chatterjee, A., Singh, A. K., Ghosh, S. K., and Raha, S. (2015). Characterization of black carbon aerosols over Darjeeling - A high altitude Himalayan station in Eastern India. *Aerosol and Air Quality Research*, 15(2):465–478.

Satish, R. and Rastogi, N. (2019). On the Use of Brown Carbon Spectra as a Tool to Understand Their Broader Composition and Characteristics: A Case Study from Crop-residue Burning Samples. *ACS Omega*, 4(1):1814–1853.

Satish, R., Shamjad, P., Thamban, N., Tripathi, S., and Rastogi, N. (2017). Temporal Characteristics of Brown Carbon over the Central Indo-Gangetic Plain. *Environmental Science and Technology*, 51(12):6765–6772.

Schneider, J., Kirchner, U., Borrmann, S., Vogt, R., and Scheer, V. (2008). In situ measurements of particle number concentration, chemically resolved size distributions and black carbon content

of traffic-related emissions on German motorways, rural roads and in city traffic. *Atmospheric Environment*, 42(18):4257–4268.

Shamjad, P. M., Tripathi, S. N., Thamban, N. M., and Vreeland, H. (2016). Refractive index and absorption attribution of highly absorbing brown carbon aerosols from an urban Indian city-Kanpur. *Scientific Reports*, 6(1):1–7.

Sharma, M. and Maloo, S. (2005). Assessment of ambient air PM10 and PM2.5 and characterization of PM10 in the city of Kanpur, India. *Atmospheric Environment*, 39(33):6015–6026.

Song, S., Wu, Y., Xu, J., Ohara, T., Hasegawa, S., and Li, J. (2013). Black carbon at a roadside site in Beijing : Temporal variations and relationships with carbon monoxide and particle number size distribution. *Atmospheric Environment*, 77:213–221.

Stockwell, C. E., Christian, T. J., Goetz, J. D., Jayarathne, T., Bhave, P. V., Praveen, P. S., Adhikari, S., Maharjan, R., DeCarlo, P. F., Stone, E. A., Saikawa, E., Blake, D. R., Simpson, I. J., Yokelson, R. J., and Panday, A. K. (2016). Nepal Ambient Monitoring and Source Testing Experiment (NAMaSTE): Emissions of trace gases and light-absorbing carbon from wood and dung cooking fires, garbage and crop residue burning, brick kilns, and other sources. *Atmospheric Chemistry and Physics*, 16(17):11043–11081.

Takahama, S., Russell, L. M., Shores, C. A., Marr, L. C., Zheng, J., Levy, M., Zhang, R., Castillo, E., Rodriguez-Ventura, J. G., Quintana, P. J., Subramanian, R., Zavala, M., and Molina, L. T. (2014). Diesel vehicle and urban burning contributions to black carbon concentrations and size distributions in Tijuana, Mexico, during the Cal-Mex 2010 campaign. *Atmospheric Environment*, 88:341–352.

Tartakovsky, D., Broday, D. M., and Stern, E. (2013). Evaluation of AERMOD and CALPUFF for predicting ambient concentrations of total suspended particulate matter (TSP) emissions from a quarry in complex terrain. *Environmental Pollution*, 179:138–145.

Tartakovsky, D., Stern, E., and Broday, D. M. (2016). Dispersion of TSP and PM10 emissions from quarries in complex terrain. *Science of the Total Environment*, 542:946–954.

Teich, M., Van Pinxteren, D., Wang, M., Kecorius, S., Wang, Z., Müller, T., Močnik, G., and Herrmann, H. (2017). Contributions of nitrated aromatic compounds to the light absorption of water-soluble and particulate brown carbon in different atmospheric environments in Germany and China. *Atmospheric Chemistry and Physics*, 17(3):1653–1672.

Titos, G., del ï£¡guila, A., Cazorla, A., Lyamani, H., Casquero-Vera, J. A., Colombi, C., Cuccia, E., Gianelle, V., Močnik, G., Alastuey, A., Olmo, F. J., and Alados-Arboledas, L. (2017). Spatial and temporal variability of carbonaceous aerosols: Assessing the impact of biomass burning in the urban environment. *Science of the Total Environment*, 578:613–625.

Tiwari, S., Dumka, U. C., Gautam, A. S., Kaskaoutis, D. G., Srivastava, A. K., Bisht, D. S., Chakrabarty, R. K., Sumlin, B. J., and Solmon, F. (2017). Assessment of PM2.5 and PM10 over Guwahati in Brahmaputra River Valley: Temporal evolution, source apportionment and meteorological dependence. *Atmospheric Pollution Research*, 8(1):13–28.

Tiwari, S., Dumka, U. C., Hopke, P. K., Tunved, P., Srivastava, A. K., Bisht, D. S., and Chakrabarty,

R. K. (2016). Atmospheric heating due to black carbon aerosol during the summer monsoon period over Ballia: A rural environment over Indo-Gangetic Plain. *Atmospheric Research*, 178-179(April):393–400.

Tiwari, S., Pipal, A. S., Srivastava, A. K., Bisht, D. S., and Pandithurai, G. (2015). Determination of wood burning and fossil fuel contribution of black carbon at Delhi, India using aerosol light absorption technique. *Environmental Science and Pollution Research*, 22(4):2846–2855.

Tiwari, S., Srivastava, A. K., Bisht, D. S., Parmita, P., Srivastava, M. K., and Attri, S. D. (2013). Diurnal and seasonal variations of black carbon and PM2.5 over New Delhi, India: Influence of meteorology. *Atmospheric Research*, 125-126:50–62.

Trompetter, W. J., Grange, S. K., Davy, P. K., and Ancelet, T. (2013). Vertical and temporal variations of black carbon in New Zealand urban areas during winter. *Atmospheric Environment*, 75:179–187.

USEPA (2002). Health assessment document for diesel engine exhaust. Technical report, U.S. Environmental Protection Agency.

USEPA (2012). Report to Congress on Black Carbon Department of the Interior, Environment, and Related Agencies Appropriations Act, 2010. Technical Report March, U.S. Environmental Protection Agency.

USEPA (2021). User's Guide for the AMS/EPA Regulatory Model (AERMOD): EPA-454/B-21-001. Technical report, U.S. Environmental Protection Agency.

Vaishya, A., Singh, P., Rastogi, S., and Babu, S. S. (2017). Aerosol black carbon quantification in the central Indo-Gangetic Plain: Seasonal heterogeneity and source apportionment. *Atmospheric Research*, 185:13–21.

Vaitieknas, P. and Banaityte, R. (2007). Modeling of motor transport exhaust pollutant dispersion. *Journal of Environmental Engineering and Landscape Management*, 15(1):39–46.

Väkevä, M., Kulmala, M., Stratmann, F., and Hämeri, K. (2002). Field measurements of hygroscopic properties and state of mixing of nucleation mode particles. *Atmospheric Chemistry and Physics*, 2(1):55–66.

Van der Zee, S. C., Fischer, P. H., and Hoek, G. (2016). Air pollution in perspective: Health risks of air pollution expressed in equivalent numbers of passively smoked cigarettes. *Environmental Research*, 148:475–483.

Venkatram, A., Isakov, V., Seila, R., and Baldauf, R. (2009). Modeling the impacts of traffic emissions on air toxics concentrations near roadways. *Atmospheric Environment*, 43(20):3191–3199.

Wang, J., Liu, D., Ge, X., Wu, Y., Shen, F., Chen, M., Zhao, J., Xie, C., Wang, Q., Xu, W., Zhang, J., Hu, J., Allan, J., Joshi, R., Fu, P., Coe, H., and Sun, Y. (2019). Characterization of black carbon-containing fine particles in Beijing during wintertime. *Atmospheric Chemistry and Physics*, 19(1):447–458.

Wang, R., Tao, S., Balkanski, Y., Ciais, P., Boucher, O., Liu, J., Piao, S., Shen, H., Vuolo, M. R., Valari, M., Chen, H., Chen, Y., Cozic, A., Huang, Y., Li, B., Li, W., Shen, G., Wang, B., and Zhang, Y. (2014).

Exposure to ambient black carbon derived from a unique inventory and high-resolution model. *Proceedings of the National Academy of Sciences of the United States of America*, 111(7):2459–2463.

Wang, R., Tao, S., Shen, H., Wang, X., Li, B., Shen, G., Wang, B., Li, W., Liu, X., Huang, Y., Zhang, Y., Lu, Y., and Ouyang, H. (2012). Global emission of black carbon from motor vehicles from 1960 to 2006. *Environmental Science and Technology*, 46(2):1278–1284.

Wang, X., Westerdahl, D., Chen, L. C., Wu, Y., Hao, J., Pan, X., Guo, X., and Zhang, K. M. (2009). Evaluating the air quality impacts of the 2008 Beijing Olympic Games: On-road emission factors and black carbon profiles. *Atmospheric Environment*, 43(30):4535–4543.

Wang, Y., Shupler, M., Birch, A., Chu, Y. L., Jeronimo, M., Rangarajan, S., Mustaha, M., Heenan, L., Seron, P., Lanas, F., Salazar, L., Saavedra, N., Oliveros, M. J., Lopez-Jaramillo, P., Camacho, P. A., Otero, J., Perez-Mayorga, M., Yeates, K., West, N., Ncube, T., Ncube, B., Chifamba, J., Yusuf, R., Khan, A., Liu, Z., Bo, H., Wei, L., Tse, L. A., Mohan, D., Kumar, P., Gupta, R., Mohan, I., Jayachitra, K. G., Mony, P. K., Rammohan, K., Nair, S., Lakshmi, P. V., Sagar, V., Khawaja, R., Iqbal, R., Kazmi, K., Yusuf, S., Brauer, M., and Hystad, P. (2022). Measuring and predicting personal and household Black Carbon levels from 88 communities in eight countries. *Science of the Total Environment*, 818.

Warren, S. G. and Clarke, A. D. (1990). Soot in the atmosphere and snow surface of Antarctica. *Journal of Geophysical Research*, 95(D2):1811–1816.

Weil, J. C., Corio, L. A., and Brower, R. P. (1997). A PDF dispersion model for buoyant plumes in the convective boundary layer. *Journal of Applied Meteorology*, 36(8):982–1003.

Weingartner, E., Saathoff, H., Schnaiter, M., Streit, N., Bitnar, B., and Baltensperger, U. (2003). Absorption of light by soot particles: Determination of the absorption coefficient by means of aethalometers. *Journal of Aerosol Science*, 34(10):1445–1463.

WHO (2012). World Health Organization: Health effects of black carbon. Technical report, WHO.

Willmott, C. J. (1982). Some comments on the evaluation of model performance. *Bulletin - American Meteorological Society*, 63(11):1309–1313.

Wu, J., Lu, J., Min, X., and Zhang, Z. (2018). Distribution and health risks of aerosol black carbon in a representative city of the Qinghai-Tibet Plateau. *Environmental Science and Pollution Research*, 25(20):19403–19412.

Yan, F., Winijkul, E., Jung, S., Bond, T. C., and Streets, D. G. (2011). Global emission projections of particulate matter (PM): I. Exhaust emissions from on-road vehicles. *Atmospheric Environment*, 45(28):4830–4844.

Yuan, L., Yin, Y., Xiao, H., Yu, X., Hao, J., Chen, K., and Liu, C. (2016). A closure study of aerosol optical properties at a regional background mountainous site in Eastern China. *Science of the Total Environment*, 550:950–960.

Zha, S., Cheng, T., Tao, J., Zhang, R., Chen, J., Zhang, Y., Leng, C., Zhang, D., and Du, J. (2014). Characteristics and relevant remote sources of black carbon aerosol in Shanghai. *Atmospheric Research*, 135:159–171.

Zhang, X., Lin, Y. H., Surratt, J. D., and Weber, R. J. (2013). Sources, composition and absorption Ångström exponent of light-absorbing organic components in aerosol extracts from the los angeles basin. *Environmental Science and Technology*, 47(8):3685–3693.

Zhao, G., Tao, J., Kuang, Y., Shen, C., Yu, Y., and Zhao, C. (2019). Role of black carbon mass size distribution in the direct aerosol radiative forcing. *Atmospheric Chemistry and Physics*, 19(20):13175–13188.

Zheng, J., Hu, M., Du, Z., Shang, D., Gong, Z., Qin, Y., Fang, J., Gu, F., Li, M., Peng, J., Li, J., Zhang, Y., Huang, X., He, L., Wu, Y., and Guo, S. (2017). Influence of biomass burning from South Asia at a high-altitude mountain receptor site in China. *Atmospheric Chemistry and Physics*, 17(11):6853–6864.

Zotter, P., Herich, H., Gysel, M., El-Haddad, I., Zhang, Y., Mocnik, G., Hüglin, C., Baltensperger, U., Szidat, S., and Prévôt, A. S. (2017). Evaluation of the absorption Ångström exponents for traffic and wood burning in the Aethalometer-based source apportionment using radiocarbon measurements of ambient aerosol. *Atmospheric Chemistry and Physics*, 17(6):4229–4249.

List of Publications

Refereed International Journals

I. **Singh, S.** and Gokhale, S. (2021). Source apportionment and light absorption properties of black and brown carbon aerosols in the Brahmaputra River Valley region. *Urban Climate*, 39, p.100963 [**IF: 6.663**].

II. **Singh, S.** and Gokhale, S. (2022). Effect of COVID-19 epidemic led-lockdowns on aerosol black carbon concentration, sources and its radiation effect in Northeast India. *Journal of Earth System Science*, 131(2), p.139 [**IF: 1.912**].

III. **Singh, S.** and Gokhale, S. (2023). Modelling the dispersion of traffic-derived black carbon emissions into hilly terrain of northeast India. *Environmental Monitoring and Assessment* [**Under review**].

Conferences

I. **Singh, S.** and Gokhale, S. (2019). Fossil fuel and biomass originated black carbon and its seasonal contribution in the rural tract of Brahmaputra River basin. *International Conference on Atmospheric Chemistry and Physics in Highly Polluted Environments*, Indian Institute of Technology Delhi, March 22-24.

II. Chaudhury, A. S., **Singh, S.** and Gokhale, S. (2018). Traffic black carbon: A neural network based source optimization study. *Research Conclave*, Indian Institute of Technology Guwahati, March 18.

Awards

⁕ **Student Travel Award** (2019) by China-India Association of Atmospheric Scientists (CIAAS), International conference held at Indian Institute of Technology Delhi on March 22-24.